Synthesis and Characterization of Ceria-based Electrolyte for Intermediate Temperature Solid Oxide Fuel Cell

A
Ph.D. Thesis
Submitted for the award of the degree of

Doctor of Philosophy

by

Taranveer Kaur

(Registration No. 901812003)

Under the supervision of

Dr. Jayant Kolte
Assistant Professor

Dr. Kulvir Singh
Professor

THAPAR INSTITUTE
OF ENGINEERING & TECHNOLOGY
(Deemed to be University)

Department of Physics & Material Science
Thapar Institute of Engineering & Technology, Patiala
Punjab-147004

February 2024

Dedicated to

my

beloved parents

Certificate

This is to certify that the thesis entitled "Synthesis and Characterization of Ceria-based Electrolyte for Intermediate Temperature Solid Oxide Fuel Cell" which is being submitted by Taranveer Kaur in the fulfilment of the requirement for the award of the degree Doctor of Philosophy in the Department of Physics & Material Science, Thapar Institute of Engineering & Technology (TIET), is an authentic record of candidate's own work carried out by her under our supervision and guidance. The matter presented in this thesis has not been submitted in part or full for the award of any degree in any other University or Institute.

Date: 27.08.2024

Place: Patiala

Dr. Jayant Kolte

Assistant Professor

Department of Physics & Material Science

Thapar Institute of Engineering & Technology

Patiala -147004, India

Dr. Kulvir Singh

Professor & Head

Department of Physics & Material Science

Thapar Institute of Engineering & Technology

Patiala -147004, India

Acknowledgment

I would like to express my deepest gratitude to my supervisors, **Dr. Kulvir Singh and Dr. Jayant Kolte,** for their unwavering support, invaluable guidance, and insightful feedback throughout the entire process of conducting this research and writing this thesis. Their expertise, encouragement, and patience have been instrumental in shaping the course of this work. I am also grateful to my doctoral committee members, **Dr. Poonam Uniyal, Dr. S. D. Tiwari, and Dr. R. K. Gupta,** for their constructive criticism, thoughtful suggestions, and encouragement of my observations and results. I am highly indebted to **Dr. O. P. Pandey, Dr. B. C. Mohanty, and Dr. B. N. Chudasama** for their valuable suggestions and discussions during various stages of my research work.

Furthermore, I would like to acknowledge **SAI labs and MCF labs, Thapar Institute of Engineering and Technology, Patiala, Punjab**, and **IIC, IIT Roorkee** for characterization facilities such as XRD, FESEM, Raman spectroscopy, XPS, and TGA which are essential for the completion of this research. I thank **Mr. Ghanshyam, Mr. Pardeep Kumar, Mr. Ajit, Mr. Samarjit Mandal, Miss Lovepreet Kaur, and Miss Neha Saini** for providing the necessary help to carry out such experiments.

I am thankful to Thapar Institute of Engineering and Technology, Patiala, Punjab, for providing funding for me as a teaching associate. Sincere thanks to **Ms. Neelam Sadana, Mr. Lalji Verma, Ms. Amandeep Kaur, Mr Purushottam Kumar Singh, Mr. Vijay K Verma,** and other office staff of the Department of Physics and Materials Science for their help in office and technical matters.

I am grateful to my friend **Jyoti** for being my constant support from the beginning of my Ph.D. journey and for making this journey enjoyable. I am also thankful to my seniors **Dr. Neetu Bansal, Dr. Gaurav Sharma, Dr. Savidh Khan, Dr. Parmvir Kaur, Dr. Shivani Punj, Dr. Manmeet Kaur, and Ms. Trisha Walia** for their help. I am also thankful to my lab mates **Ms. Neha Thakur, Mr. Parminder Singh, Mr. Raj Ankit, Ms. Ayushi, Ms. Vimi Dua, Ms. Navneet Kaur, Mr. Santosh Kumar, and Ms. Aditi Sharma** for their encouragement, stimulating discussions, and moral support. Their perspectives and insights have been invaluable in shaping my ideas and refining my arguments. I would like to acknowledge the help and support received from **Ms. Jahnvi Goyal** in experimental activities during my research. Without their cooperation, this research would not have been possible.

Special thanks to my mummy, **Mrs. Parminder Kaur,** and my daddy ji, **S. Baljinder Singh,** for their constant love, encouragement, and understanding, especially during moments of stress and uncertainty. Their unwavering support has been my anchor throughout this journey. They have valued my education and my wellbeing above all. I want to thank my brother, **Pushpinder Singh**, for motivating me and supporting me throughout my journey. I would like to acknowledge significantly the blessings of my dada-dadi, **Late S. Gurdev Singh, Mrs. Chand Kaur,** and my nani, **Mrs. Saminder Kaur**.

I am also very grateful for the unconditional love and support of my husband and my best friend, **Mr. Sutanterpal Singh Manes**. No words can express how grateful I am to have you by my side. Thank you for always being by my side and helping me realize my dreams. I am also thankful for the blessings and support of my in-laws, **Mr. Baldev Singh Manes and Mrs. Parmjit Kaur.**

Finally, I extend my most profound appreciation to all the participants who generously contributed their time and insights to this study. Your support and encouragement have been indispensable; I am profoundly grateful for that.

This thesis is dedicated to my lovely parents for their constant support and love.

And above all, I pay my profound gratitude to The Almighty GOD for giving me strength, love and blessings.

Taranveer Kaur

Taranveer Kaur

Table of content

List of Figures

List of Tables

List of symbols

ρ	density
a	Lattice constant
N_A	Avogadro's number
k	Boltzmann's constant
R	Resistance
E_a	Activation energy
Å	Angstrom
λ	Wavelength
χ	Chi
S	Siemens
W	Watt
d	Interplanar spacing
ν	frequency
h	Planck's constant

Abbreviations and Nomenclature

AFC	Alkaline fuel cells
BIMEVOX	Bismuth metal vanadium oxide
CHP	Constant heat and power
CPE	Constant phase element
CTE	Coefficient of thermal expansion
DI	Deionised
EDS	Energy dispersive spectroscopy
FCC	Face centred cubic
FESEM	Field emission scanning electron microscopy
FWHM	Full width at half maximum
CGO	Cerium gadolinium oxide
ICDD	International centre for diffraction data
LSGM	Lanthanum strontium gallium manganate
MCFC	Molten carbonate fuel cell
MIEC	Mixed ionic electronic conductor
PAFC	Phosphoric acid fuel cell
PEG	Polyethylene glycol
PEMFC	Polymer exchange membrane fuel cell
PVA	Polyvinyl Alcohol
SOEC	Solid oxide electrolysis cells
SOFC	Solid oxide fuel cell
TGA	Thermogravimetric analysis
TPB	Triple phase boundary
XPS	X-ray photoelectron spectroscopy
XRD	X-ray diffraction
YSZ	Yttria stabilized zirconia

Abstract

Solid oxide fuel cells (SOFC) are environment-friendly energy conversion devices in which chemical energy transforms directly into electrical energy. These devices are highly efficient and can work with various fuels. In this process, apart from electricity, SOFC produces water steam as a by-product that can be used to co-generate electricity. Further, they can also be used in electrolysis mode to generate hydrogen and oxygen gases. Even though SOFCs have many advantages, the high operating temperature (i.e., 800-1000 °C) is a crucial bottleneck in realizing its full potential. High operating temperature poses several problems regarding the choice of materials, particularly for interconnects and glass seals. It also leads to faster interfacial reactions, material degradation, and increased operational and fabrication costs. These complexities can be overcome by reducing the operating temperature to less than 800 °C. Electrolytes are vital components in deciding the operating temperature of SOFC. The conventional SOFC uses yttria-stabilized zirconia (YSZ) as an electrolyte, which operates between 800-1000 °C. High ionic conductivity, chemical and thermal stability, as well as a dense structure, are some of the essential requirements for an electrolyte. Doped ceria is a better choice for electrolytes at intermediate temperature (500-800 °C) due to its high conductivity and better compatibility with other cell components in this temperature range.

The present thesis investigates Gd and Sr doped and co-doped ceria samples with a focus on solid oxide fuel cell development. The samples are synthesized using an ultrasound-assisted sol-gel auto-combustion method. The samples were characterized for their structural, thermal, and electrical properties. The selected electrolytes are sandwiched between the anode and cathode and tested in real SOFC conditions. The thesis is divided into six chapters, with a list of references provided at the end of the thesis.

Chapter 1 introduces fuel cells and SOFCs with a brief account of the different categories of fuel cells. The fuel cells are categorized depending on the electrolytes used in them. The properties of various SOFC components, such as anode, cathode, electrolyte, interconnects, and sealants, are also discussed in this chapter. The different designs and configurations of the SOFC are also mentioned in this chapter, emphasizing the planar design of SOFC.

Chapter 2 focuses on the literature related to ceria-based electrolytes. The ceria-based electrolytes show good conductivity at temperatures less than 800 °C. These electrolytes can help lower the operating temperature of the SOFCs. This chapter reviews the role of dopants in producing oxygen vacancies in the ceria lattice and their effect on the conductivity of these electrolytes. The different dopants and their concentration, co-dopants, and synthesis techniques are some of the factors that influence the performance of ceria-based electrolytes are also discussed. Based on the above literature, the motivation of the present study is provided, followed by the objectives of the present research work.

The detailed synthesis methods of Gd-doped, Sr-doped, and Gd-Sr co-doped ceria samples are given in **Chapter 3**. The samples are characterized using different techniques namely thermogravimetric analysis (TGA) for thermal characterization, X-ray diffraction (XRD) analysis for crystal structure, Raman studies for local structural analysis and vacancy ordering, scanning electron microscopy (SEM) for microstructural and surface analysis. The conductivity and activation energy of the sintered samples have been determined using impedance spectroscopy. Further, the prepared cells are characterized in real SOFC conditions. The technical details of these methods are discussed in this chapter.

Chapter 4 discusses the individual doping of Gd and Sr and the co-doping effect of both cations on the different structural, microstructural, and electrical properties. Doping of Gd and Sr in the ceria introduces oxygen vacancies in the lattice. XRD patterns confirm the cubic fluorite structure of the doped and co-doped samples. Although 30 % Gd-doped ceria sample

and 10 % Sr-doped ceria sample showed the existence of secondary phase. The existence of secondary phase is confirmed by the trends in the lattice parameter and Raman spectra. Raman spectra also confirm the existence of intrinsic and extrinsic oxygen vacancies produced by the dopants (Gd^{3+} and Sr^{2+}) and the conversion of Ce^{4+} to Ce^{3+}. The XPS data has been used to verify the existence of the Ce^{4+} and Ce^{3+} ions in the lattice. The microstructural studies showed a highly dense structure, showing partial liquid phase sintering in Sr-doped and Gd-Sr co-doped samples. The conductivity analysis showed increased conductivity in doped and co-doped samples compared to the undoped samples. The 10 % Gd-doped ceria sample showed the highest conductivity of 1.67×10^{-2} Scm^{-1}, followed by 10 % Gd and 2.5 % Sr co-doped ceria sample, which showed 1.20×10^{-2} Scm^{-1} at 600 °C.

In **chapter 5**, the optimization of the anode for the tape-casting process and the electrolyte for the spray-coating process is discussed. The anode-supported cells are made by tape casting the anode and spray coating the electrolyte. The anode and electrolyte are co-sintered together at 1450 °C for 4 h. The cathode is then painted on top of electrolyte and sintered at 1000 °C for 2 h, forming the complete cell. The fractured surface images of the cells show highly dense electrolytes sandwiched between two porous electrodes. The complete cell is studied in real SOFC conditions using hydrogen (3 % H_2O) as fuel on the anode and ambient air on the cathode side. A highest power density of 112.7 $mWcm^{-2}$ has been achieved for 10 % Gd and 2.5 % Sr-doped ceria samples.

Chapter 6 concludes the results discussed in the previous chapters on Gd-doped ceria, Sr-doped ceria, and Gd-Sr co-doped ceria. The doped ceria electrolyte with cubic fluorite structure is formed. The solid solubility limit of Gd, Sr, and Gd-Sr co-doped in ceria is ~20 %, ~7.5 %, and 5.0 %, respectively. The highest conductivity is observed for 10 % Gd doped CeO_2 (1.67×10^{-2} Scm^{-1} at 600 °C), followed by 10 % Gd-2.5 % Sr doped ceria and then 10 % Gd and 5.0 % Sr doped ceria. Based on optimization and conductivity, the four samples, CG1, CS3,

CG1S1, and CG1S2, are fabricated and tested in real SOFC conditions. In these series, $Ce_{0.875}Gd_{0.1}Sr_{0.025}O_{1.925}$ shows the best results regarding phase stability, microstructure, conductivity, and power density. This implies that $Ce_{0.875}Gd_{0.1}Sr_{0.025}O_{1.925}$ can be a potential candidate as an electrolyte for intermediate-temperature SOFCs. The chapter concludes with a discussion of future perspectives and suggestions for the study.

Chapter 1

Introduction

1.1 Fuel Cells

The world energy crisis refers to the increasing concerns over the limited availability and sustainability of global energy sources and reducing carbon emissions. Energy demand has skyrocketed as the world's population grows and economies expand. For a very long time, the primary energy sources have been fossil fuels like coal, oil, and natural gas. However, these sources are non-renewable and aggravate environmental problems such as air pollution and climate change. Moreover, the growing concern about the availability of conventional energy resources and the environmental impact of power generation using these resources has led to the development of alternative energy sources. To address the world energy crisis, there is a growing need for investment in cleaner, renewable, sustainable, and efficient energy sources. Renewable energy sources consist of solar cells, wind mills, geothermal plants, biogas plants, and hydroelectric dams [1]. The issue with solar cells and windmills is their low efficiency and require large installation areas. However, geothermal, and hydroelectric plants are known to disrupt the ecosystem. In comparison, fuel cells are much more efficient, cleaner, and environmentally friendly devices [2]. Fuel cells regularly achieve 40-60% efficiencies depending upon the current drawn from the device [3]. Also, fuel cells generate low carbon dioxide emissions and negligible SO_x and NO_x gases [4]. Fuel cells are well-known for their high efficiency, minimal emissions, and versatility, as they can be used in various applications, from powering small electronics to providing electricity for vehicles and houses. Much of the hydrogen and oxygen used in fuel cells combine to form a harmless by-product, namely water steam.

Fuel cells consist of two electrodes, viz. anode and cathode, with an electrolyte placed between them. Electrodes are generally made of metals or semi-conducting materials, and the electrolyte might be either liquid or solid depending on the type of fuel cell. The electrodes are connected externally through an electric circuit. The electrochemical reaction in a fuel cell involves the fuel (such as hydrogen) oxidizing at the anode to produce electrons and protons. The electrons travel through an external circuit to generate electrical power. Oxygen undergo reduction at cathode by combining with these electrons. Protons or oxide ions move through the electrolyte depending on the type. For an oxide ion carrier electrolyte, oxide ion will move to the anode, where they combine with hydrogen to generate heat, water, and electrons. The electrochemical reactions occurring at the anode and the cathode for such type of electrolyte are given in equation (1.1) and (1.2), respectively and the overall chemical reaction is given in equation (1.3)

At cathode: $$\frac{1}{2}O_2 + 2e^- \rightarrow O^{2-} \quad (1.1)$$

At anode: $$H_2 + O^{2-} \rightarrow H_2O + 2e^- \quad (1.2)$$

Equivalent chemical reaction: $$H_2 + \frac{1}{2}O_2 \rightarrow H_2O \quad (1.3)$$

The electrons traveling through the external circuit produce an electrical current that does the electrical work.

1.2 Types of Fuel Cells

Fuel cells generally have two types of electrolytes, either a liquid electrolyte or a solid electrolyte. A summary of the different fuel cells with their merits and demerits is given in **Table 1.1**. Based on the type of electrolyte, these are categorized as follows:

Table 1.1 Types of fuel cells, electrolyte used, charge carrier, operating temperature, efficiency, and their merits and demerits [3, 5]

Types of fuel cells	**Electrolyte**	**Charge carrier**	**Operating Temp. (°C)**	**Efficiency**	**Merit**	**Demerit**
PEFC	Thin polymer electrolyte	H^+	~90	40-50 %	Low operating temperature, highest power density	Requires expensive Pt catalyst, CO and S poisoning, and expensive components
AFC	Potassium hydroxide (KOH)	OH^-	60-250	50 %	Better cathode performance, low-cost electrolyte, non-precious metal catalyst	Requires pure H_2 and O_2, electrolyte replenishment and water removal required
PAFC	Phosphoric Acid	H^+	180-210	40 %	Advanced technology, Reliable and low-cost electrolyte	Liquid electrolyte, CO and S poisoning, and expensive Pt catalyst
MCFC	Alkali Carbonates	CO_3^{2-}	600-700	45-55 %	Low-cost catalyst, high-quality heat generation, fuel flexibility	Corrosive and molten electrolytes, expensive materials, CO_2 release, and degradation
SOFC	Ceramic solid oxides	O^{2-}	800-1000	50-60 %	Solid electrolyte, high-quality waste heat, high power density, no expensive	High operating temperature and sealing issues.

		catalyst required, fuel flexibility

1.2.1 Alkaline Fuel Cells (AFC)

The electrolyte in an AFC is an alkaline solution (sodium hydroxide or potassium hydroxide). This electrolyte is kept in the asbestos matrix. It operates at 60-220 °C, depending on the electrolyte concentration [5]. The electrolyte transports the hydroxyl ion (OH^-) from the cathode to the anode. Only pure H_2 and O_2 are used as fuel in these cells, as CO or CO_2 are poisonous for these cells. AFCs can achieve an operating voltage of about 0.875 V [3]. The electrical efficiency of AFCs lies between 40-50 % [6]. AFCs were first developed in the 1930s and used by NASA in their Apollo spacecraft mission. This fuel cell is very advanced, but its demerit is a liquid electrolyte and limited fuel flexibility.

1.2.2 Polymer (Proton) Exchange Membrane Fuel Cells (PEMFC)

The electrolyte in PEMFC is an ion exchange membrane (fluorinated sulphonic acid polymer). The electrolyte is solid in nature and conducts protons. These are also known as proton exchange membrane fuel cells. For both the anode and cathode, carbon electrodes with platinum electrocatalysts are used. Extensive and fine processing for fuels other than pure hydrogen and oxygen is necessary since even minimal amounts of CO, sulphur species, and halogens can readily poison the electrodes [5]. The efficiency of the cell is about 45 to 55%, and the operating temperature is between 60-80 °C [6]. Currently, PEMFC exhibits the highest power output (500-2500 $mWcm^{-2}$) and is considered for use in vehicles and portable applications [3, 7].

1.2.3 Phosphoric Acid Fuel Cell (PAFC)

Phosphoric acid (H_3PO_4), in its liquid form, is used as the electrolyte in PAFC. The cell typically operates between 150-220 °C. The acid is retained in a silicon carbide matrix sandwiched between two porous graphite electrodes containing the platinum catalyst. Using platinum catalyst makes these cells susceptible to CO or sulphur poisoning. The electrical efficiency of PAFCs is up to 30-42 % [6]. These fuel cells were the first to be made commercial and widely studied during the 1980s-2000s [7]. PAFCs are mainly intended for use in stationary applications.

1.2.4 Molten Carbonate Fuel Cell (MCFC)

The electrolyte in MCFC is usually a combination of molten alkali carbonates (lithium or potassium carbonate), which is retained in the $LiAlO_2$ matrix. The cell operates at high temperatures of 600 to 700 °C. The carbonate ions that move through the highly conductive molten salt provide ionic conduction. Ni and NiO can be used at higher temperatures as catalysts [5]. When these incoming carbonate ions combine with hydrogen, they produce carbon dioxide and water and release electrons into the external circuit. The efficiency of the cell is generally 43-55 % [6]. These cells can also operate with other fuels like biogas, natural gas, and coal gas. The development of MCFCs has been focussed on larger maritime and stationary applications.

1.2.5 Solid Oxide Fuel Cell (SOFC)

The electrolyte in an SOFC is a solid, non-porous metal oxide, typically Y_2O_3-stabilized ZrO_2 (YSZ). The cell operates at 800-1000 °C. Oxide ions are carried through the electrolyte in this cell. The anode and cathode materials are different in SOFC. The anode is usually a cermet (Ni-YSZ), and the cathode is a mixed ionic electronic conductor (MIEC, Sr doped $LaMnO_3$) [5]. The electrical efficiency of the cell is about 50-60% [3, 6, 8]. SOFCs are now considered

for various applications, such as stationary power generation, mobile power, and vehicle power.

SOFC has the highest efficiency among the different energy-generating systems, as shown in **Fig 1.1**. These devices do not require any expensive catalyst because of their high operating temperature. Without needing an external reformer, they can work with different fuels, such as methane, butane, biogas, and natural gas [2, 9]. The efficiency of an SOFC can reach more than 80 % when used in a combined heat and power (CHP) mode.

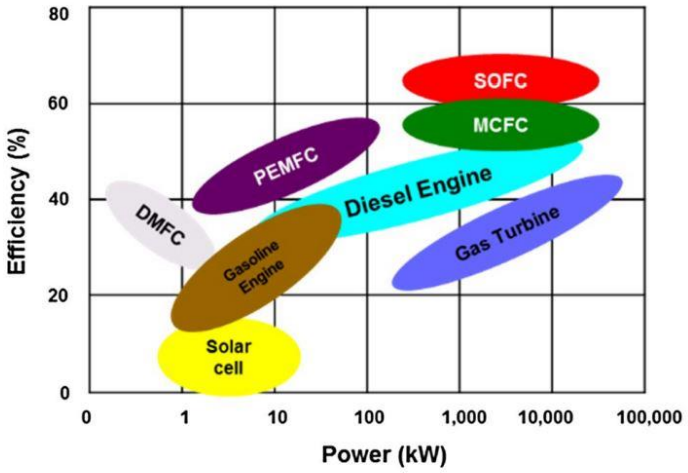

Fig 1.1 A comparison of efficiency vs power of some power-generating devices [2]

1.3 Working principle of SOFC

SOFCs use a solid oxide electrolyte to change chemical energy into electrical energy. SOFCs do not require any external reformer for the fuel cell as their high temperature facilitates internal reforming. Additionally, their high temperature allows the use of inexpensive catalysts such as nickel [10]. The fuel cells are suitable for medium and large-scale power generation because of their high efficiency, internal reforming, and use in CHP systems [11]. They have a longer lifespan, have low maintenance, and do not produce any harmful emissions. These devices can also work in the reverse mode as solid oxide electrolysis cells (SOEC) for H_2O, CO_2, and NO conversion [12]. The SOEC can have an efficiency of more than 90 % [12]. These

devices can convert hazardous CO_2 into a more useful substance, thus reducing its emission into the atmosphere. Although SOFC technology is not widespread, with ongoing research and development, it can become a significant player in the energy sector.

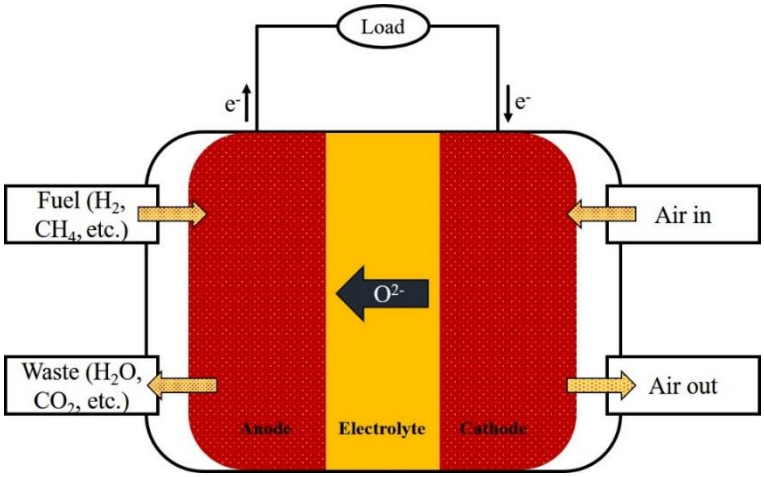

Fig 1.2 Schematic of SOFC, which conducts oxygen ions through the electrolyte

The cell is constructed with a dense electrolyte placed between two porous electrodes. The schematic of the cell is shown in **Fig 1.2**. Oxygen is reduced at the cathode into oxide ions by acquiring electrons from the electrode. These oxide ions travel from cathode to anode via electrolyte, driven by the difference of chemical potential established between the electrodes. At the anode, these ions will oxidize the hydrogen from the fuel with the help of an internal catalyst, giving water, heat, and electrons as a reaction product. These electrons move through the external circuit to produce a current. Thus, the purpose of the anode is to allow the electrochemical oxidation of fuel, transport electrons to the external circuit, and allow internal fuel reforming. The purpose of the electrolyte is to isolate the two half-reactions given in the equation (1.1) and (1.2), prevent the mixing of fuel and air, and transport oxide ions from the cathode to the anode. An oxygen reduction reaction occurs at the cathode, in which the oxygen from the air or fuel combines with the electrons from the external circuit to produce oxide ions in the presence of a catalyst.

However, SOFCs face some challenges related to cost, durability, and reliability, which are being actively researched and addressed by the scientific community. Most of these issues can be resolved by reducing the operating temperature of the SOFC [13]. The SOFCs that operate at temperatures above 800 °C are called high-temperature solid oxide fuel cells (HTSOFC), those operating between 500 and 800 °C are called intermediate-temperature solid oxide fuel cells (ITSOFC), while the SOFCs operating at temperatures less than 500 °C are called low-temperature solid oxide fuel cell (LTSOFC).

1.4 SOFC configuration and components

SOFC can be fabricated in two main configurations, i.e., planar SOFC and tubular SOFC, as shown in **Fig 1.3**. Tubular SOFC (**Fig 1.3** (a)) are easier to seal and have good thermal-cycling stability. The prime purpose of a tubular configuration is to eliminate the use of gas-tight seals at higher temperatures [7]. The cell is shaped as a tube closed at one end and open at the other. In tubular fuel cells, fuel flows along the anode, and air passes through the cell using a thin alumina tube located inside the cell. However, this design results in longer current paths around the tubular circumference and depicts higher cell internal resistance. This tubular configuration is the more advanced configuration of SOFC.

Planar SOFC (**Fig 1.3 (b)**), on the other hand, are easier to fabricate using tape casting and screen-printing methods. They also have higher power densities than tubular configurations [14, 15]. In planar SOFC, the different cell parts are in the form of thin plates stacked on each other. Planar SOFCs are easier to stack than tubular cells but are prone to crack and require high-temperature gas-tight sealing [7]. Planar configuration is usually preferred because of its simple design, easy fabrication, and cost-effectiveness [16]. The different components of an SOFC are discussed below:

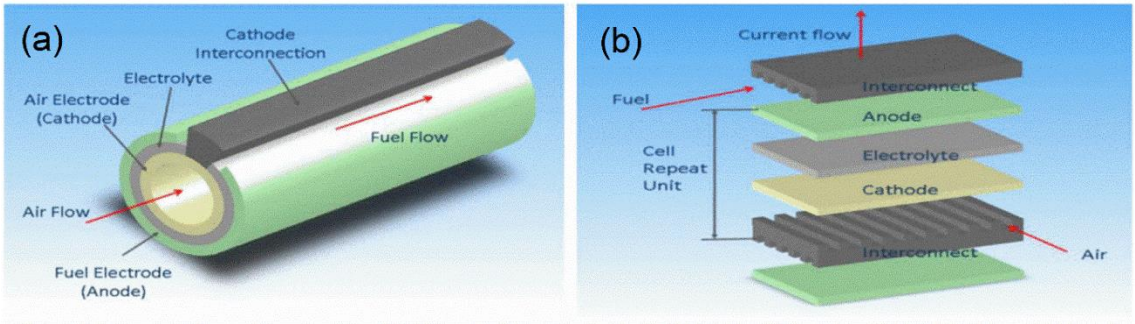

Fig 1.3 (a) Planar and (b) tubular configurations of SOFC [15]

1.4.1 Anode

The anode is the electrode where the oxidation of hydrogen gas takes place. The electrons liberated during this process are sent to the outer electrical circuit. The oxidation reaction occurs at the triple phase boundaries (TPB) in the presence of hydrogen (fuel), electrons (from the electrode), and oxide ions (the electrolyte phase) [17]. The anode should possess the following properties [18]:

- Mixed conductor with high electrical conductivity (~100 Scm^{-1}).
- Sufficient porosity to allow gas flow to the inner chambers of the electrode.
- Good thermal and chemical stability.
- Minimum mismatch of coefficient of thermal expansion (CTE) with other components.
- High catalytic activity to allow complete oxidation of hydrogen.
- Avoid coke deposition while working with fuels like methane, butane, natural gas, etc.

The most common material considered for SOFC anode is Ni-YSZ cermet. The addition of YSZ to Ni extends the TPBs [19]. Here, Ni acts as the electronic conductor as well as the catalyst. YSZ provides the structural backbone, ionic conductivity, and improves thermal coefficient matching between the anode and electrolyte [3]. At low temperatures, YSZ is usually replaced by cerium gadolinium oxide (CGO), as CGO performs better than YSZ below 800 °C [20]. Ceria-based materials also prevent coke deposition in the anode and show better

catalytic activity at low temperatures [21, 22]. Other than these two materials, Cu-Ni-YSZ, $Sr_2Mg_{1-x}Mn_xMoO_{6-x}$, $Fe_xCo_{0.5-x}Ni_{0.5}$-SDC, $Ni_{0.8}Co_{0.15}Al_{0.05}LiO_2$, $La_{1-x}Sr_xTiO_{3-\delta}$, Cu-$CeO_2$-YSZ, are also developed as alternate anode materials [23-25].

1.4.2 Electrolyte

In SOFC, the electrolyte is exposed to the reducing and oxidizing conditions on the anode and cathode sides, respectively. The oxygen ions (O^{2-}) move through the electrolyte by an ion-hopping process through the oxygen vacancies. This mechanism is a thermally activated process. For a long-term and stable operation, the electrolyte should have the following properties [18, 26]:

- High ionic conductivity (~0.1Scm^{-1}) for faster transport of ions from the anode to the cathode at working temperature of SOFC.
- High density to avoid mixing of the fuels from the anode and cathode side.
- Good chemical and thermal stability in oxidizing and reducing oxygen partial pressures (1-10^{-22} atm.).
- Minimum mismatch of CTE with other cell components.

In SOFC, the most common electrolyte used is YSZ. As an oxide ion conductor, it has several other advantages, such as high mechanical strength, non-toxicity, and chemical stablility [1, 27]. Other than this, many other oxides such as doped CeO_2, doped Bi_2O_3, and perovskite such as doped $LaGaO_3$ have also been studied as electrolytes for SOFC. These oxides are not good ionic conductors on their own. However, their conductivity can be improved using dopants, which are widely studied as electrolytes in lower operating temperatures (<800 °C).

1.4.3 Cathode

The electrode where the oxygen reduction reaction occurs is called the cathode or air electrode. Similar to the anode, this reaction occurs at the TPBs, which include the oxygen gas, the

cathode, and the electrolyte [28]. The cathode should possess the following properties for optimum performance [10, 18]:

- Mixed conductor with high electrical conductivity (~100 Scm^{-1}).
- Sufficient Porosity to enable gas transport to the inner chambers of the electrode.
- Good chemical and thermal stability.
- Minimum mismatch of CTE with other cell components.
- High catalytic activity to allow complete oxygen reduction reaction.
- Good tolerance towards atmospheric impurities.

Since metals are unstable in a high-temperature oxidizing atmosphere, ceramics are the only materials used for SOFC cathode. For high-temperatures SOFC, strontium-doped $LaMnO_3$ (LSM) is usually employed as a cathode [29]. LSM has good electronic conductivity but poor ionic conductivity. YSZ is added to the cathode to enhance the ionic conductivity and increase the TPBs [18]. For ITSOFC, Sr and Fe-doped $LaCoO_3$ (LSCF) and Sm-doped $SrCoO_3$ are usually employed [6]. Gd or Sm doped ceria is added to these cathodes to improve their ionic conductivity with an increased number of TPBs.

1.4.4 Interconnects

Interconnects collect current from the cells and transfer it to an external electric circuit. These materials must have high electronic conductivity, chemical stability, low ionic conductivity, and their CTE match with the anode and the cathode [18]. Also, these materials should be stable in oxidizing and reducing conditions. Lanthanum chromate ($LaCrO_3$) doped with Sr has been utilized with YSZ as an interconnect as it can withstand temperatures as high as 1000 °C [29]. Meanwhile, for low-temperature SOFCs, metallic alloys such as ferritic steel with high Cr content (Crofer 22 APU) are used as interconnects [30, 31]. These metallic interconnects are low-cost and have high electrical conductivity.

1.4.5 Sealants

Sealants play an essential role in avoiding leakage of gas materials from the anode and cathode and thus avoiding mixing the two gases, especially in the planar configuration of SOFC. A sealant material should be low-cost with CTE matching with other cell parts, be resilient, and have good resistance against thermal shock [18, 32]. There are two types of sealing: compressive and rigid sealing [29]. Compressive sealing uses mica sealing or metals such as gold, platinum, and silver. Silver, the least expensive metal, is mainly preferred for low-temperature SOFCs [33]. Rigid sealing is either a glass-ceramic sealant or a brazen alloy. Brazen alloys are not used at high temperatures as metals oxidize quickly [32]. Glasses such as alkaline earth borosilicate and aluminosilicate glass-ceramics with transition temperatures close to operating temperature are usually employed for SOFC as sealants [34, 35].

SOFCs are also classified into four types- electrolyte-supported, anode-supported, cathode-supported, and metal-supported, as shown in **Fig 1.4**. The supporting layer is usually thicker than other parts as it gives mechanical support to the entire cell. An electrolyte-supported cell is the most robust one, providing better tolerance against redox cycles, good sealing, and better fuel efficiency [36]. This type of cell configuration is usually employed for higher operating temperatures. However, thick electrolytes increase ohmic losses at low temperatures [29]. A very thin electrolyte is deposited on top of the electrode support in the electrode-supported cell. The advantage of electrode-supported cells is that the electrolytes can be made as thin as possible to reduce electrical losses and the supporting electrode is thick (>300 μm). The use of thin electrolyte reduces the operating temperature and cell ohmic polarization, improving the overall cell performance [37]. The supporting electrode can be either an anode or cathode, and these types of cells are employed for ITSOFC. There are practical issues related to the step-wise fabrication of cathode-supported cells. Their tendency to intercalate with the electrolyte contents during the sintering process and cell operation is one of the key issues connected with

building cathode-supported SOFCs, which might result in poor electrochemical performance [38, 39]. Usually, anode-supported SOFC with thin electrolyte is employed as this type of cell performs better than other configurations due to lower ohmic electrolyte resistance [40, 41]. Metal-supported SOFC offers more structural and redox stability than ceramic support layers [42]. On the other hand, problems with the metal-supported SOFC include CTE mismatch, Cr poisoning, and oxidation of the metal support at high temperatures [29].

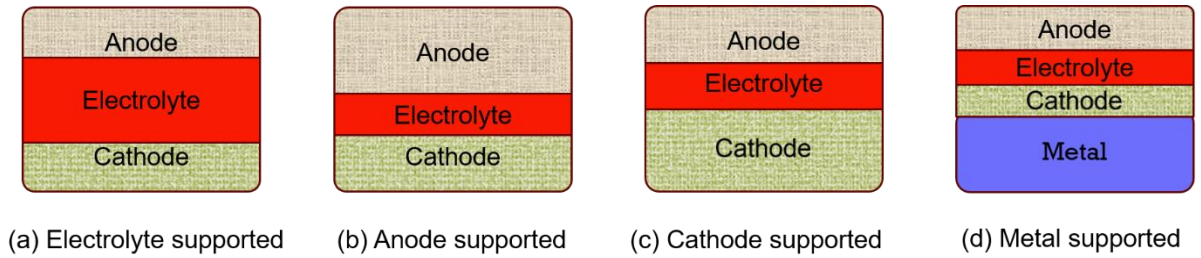

Fig 1.4 Illustration of different cell configurations

Thus, to develop different supported SOFC. The supported base is thicker than other components of SOFC. Secondly, the selection of support must have good mechanical properties and good tolerance to accommodate other components during the processing of the cells.

1.5 Common electrolyte materials for SOFC

Electrolyte is an integral part of SOFC as it bridges the two electrodes and provides ionic transport between anode and cathode. The common oxide ion electrolytes used in SOFC include lanthanum gallate compounds, stabilised zirconia, doped bismuth, and doped ceria. [26]. The majority of these electrolytes have a cubic fluorite structure. The undoped ZrO_2, CeO_2, and Bi_2O_3 exhibit low ionic conductivity. Their conductivity is improved by using suitable trivalent or divalent dopants. The charge compensation occurs in the form of oxygen vacancy defects, which usually provide the hopping site for O^{2-} ions.

Stabilized zirconia is the most commonly used electrolyte in SOFC. However, its cubic fluorite structure is stable only at temperatures higher than 2300 °C. To stabilize this structure at lower temperatures, dopants such as Y_2O_3, CaO, MgO, and Sc_2O_3 are added to the zirconia [18, 26]. Zirconia stabilized with 8 mol % Y_2O_3, commonly known as YSZ, is known to have ionic conductivity of 0.1 Scm^{-1} at 1000 °C [19]. At this mol % of yttria, the cubic fluorite structure is completely stabilized, and it shows very high chemical and mechanical stability across a broad range of oxygen partial pressures, making it most suitable material for SOFC electrolytes. Other than YSZ, scandia stabilized zirconia (ScSZ) is also known to show high ionic conductivities (0.15 Scm^{-1} at 1000 °C) [19]. Unfortunately, the expensive cost of scandia limits the use of ScSZ. Further, the problem with zirconia-based electrolytes is their high operating temperature and their reaction with strontium or lanthanum present in the cathode [43].

Doped ceria electrolytes are promising electrolytes for ITSOFC. Ceria exhibits a stable cubic fluorite structure. Although undoped ceria has very low ionic conductivity and, this conductivity is a mix of n-type and oxide ion conductivity [44]. At high temperatures (1000 °C), the conductivity of reduced ceria ($CeO_{1.9}$) is dominated by electronic contribution (70 % electronic and 30 % ionic). However, if the dopants (divalent or trivalent) are introduced in the ceria lattice, the opposite is true, i.e., the ionic conductivity dominates over the electronic conductivity [45]. The dopants introduce the oxygen vacancies in the lattice, making them primarily ionic conductors. Ceria doped with rare earth cations and alkaline earth cations such as Gd^{3+}, Sm^{3+}, Ca^{2+}, and Sr^{2+}, respectively, has shown high conductivities in the ITSOFC temperature range (500-700 °C) [46]. Also, these electrolytes show good chemical stability with other cell components. The only issue with these materials is their reduction to Ce^{3+} under reducing atmosphere of oxygen.

Bi_2O_3 is known to have four phases α, β, γ, and δ out of these, only two are stable phases (α and δ). The δ-phase has a fluorite structure and exhibits higher conductivity, although it is only stable at temperatures exceeding 730 °C. [47]. However, this phase can be stabilized at room temperature using dopants such as rare earth cations (Dy, Y, Tb) in combination with high valence cations (Gd, V, W, or Nb) [47, 48]. It has been reported that γ-$Bi_4V_2O_{11}$ doped with transition metal (BIMEVOX) demonstrates high ionic conductivity and higher stability at low temperatures (600 °C) [49]. The dopants, such as Gd, La, Cu, Ti, Al, Ga, etc., are known to stabilize this compound and improve its conductivity [50-52]. The problem with using these oxides in SOFC is their instability in the operating temperature range (500-600 °C). A slow phase transformation (δ→α) occurs at these temperatures, decreasing conductivity [29]. Further, these have poor mechanical strength and significant chemical reactivity with other components of the cell, posing a problem for their use as electrolytes [19].

Other than these cubic fluorite electrolytes, there are also perovskite structure-based electrolytes. One of the most common perovskites is $LaGaO_3$-based electrolytes. The partial substitution of La with Sr and Ga with Mg in $LaGaO_3$ (LSGM) improves its ionic conductivity [53-57]. These electrolytes exhibit minimum electronic conduction and high stability in the ITSOFC range. Adding other dopants such as Co, Ni, or Bi in small quantities at gallium sites can further improve the oxide ion conductivity of this electrolyte [58, 59]. As potential oxygen ion conductors, other lanthanum-based perovskite structures, including $LaAlO_3$, $LaSrO_3$, $LaInO_3$, $LaScO_3$, and $LaYO_3$, have also been investigated [60]. However, phase instability, gallium volatilization at high temperatures, and chemical incompatibility with nickel limit the use of these materials [18, 61].

Although YSZ is the most common electrolyte, its high operating temperature poses a big problem for the commercialization of SOFC. To reduce the operating temperature, a thin film is needed. However, the growth of thin films with similar conductivity is a herculean task, and

the film's resistance increases drastically below 800 °C [62]. The conductivity of YSZ at 500 °C is ~0.0005 Scm^{-1} [26]. Thus, developing electrolytes with high ionic conductivity at temperatures less than 700 °C is crucial. LSGM and BIMEVOX have high conductivity at low temperatures but face stability issues and CTE mismatch with other cell components [18, 19]. Overall, the ceria-based electrolytes are the most promising material for ITSOFC. Their use as electrolytes is widely studied. However, there is still a need to improve the performance of these materials with higher density, conductivity and low reduction of Ce^{4+} to Ce^{3+} during processing and operation of SOFC. The latest developments related to these materials are discussed in the next chapter.

Chapter 2

Literature Review

2.1 Background

The state-of-the-art SOFC uses YSZ as an electrolyte with operating temperature of >800 °C. This high temperature poses many problems, such as material degradation, reduced lifetime, interfacial diffusion between electrode and electrolyte, CTE mismatching problems, and increased operating cost of the cell [18]. Although a lot of research is being carried out on HTSOFCs, it is crucial to reduce the operating temperature of SOFC to improve performance, stability and overcome the problems mentioned above. Lowering the operating temperature is also important to reduce the start-up time, better compatibility between different components of SOFC, and decrease energy consumption [63]. It can be achieved by two approaches: either decrease the thickness of the YSZ electrolyte or use alternative electrolyte materials that depict higher ionic conductivity at low temperatures [64]. Using thin film techniques, fuel cells with electrolyte thickness as small as 100 nm can be made with YSZ, but these techniques are costly [65]. Some of the alternate electrolyte materials include LSGM, BIMEVOX, and doped ceria oxides [19]. These electrolytes show good ionic conductivity at intermediate operating temperatures, i.e., between 600 – 800 °C. The conductivity with respect to the temperature of these electrolytes is shown in **Fig 2.1**. Although BIMEVOX-based electrolytes have the highest conductivity, they have stability issues and are highly reactive with other components of SOFC [19]. Similarly, LSGM also have compatibility issues with other cell components as discussed in the previous chapter. So, in this chapter the latest developments in the undoped and doped ceria are given and discussed.

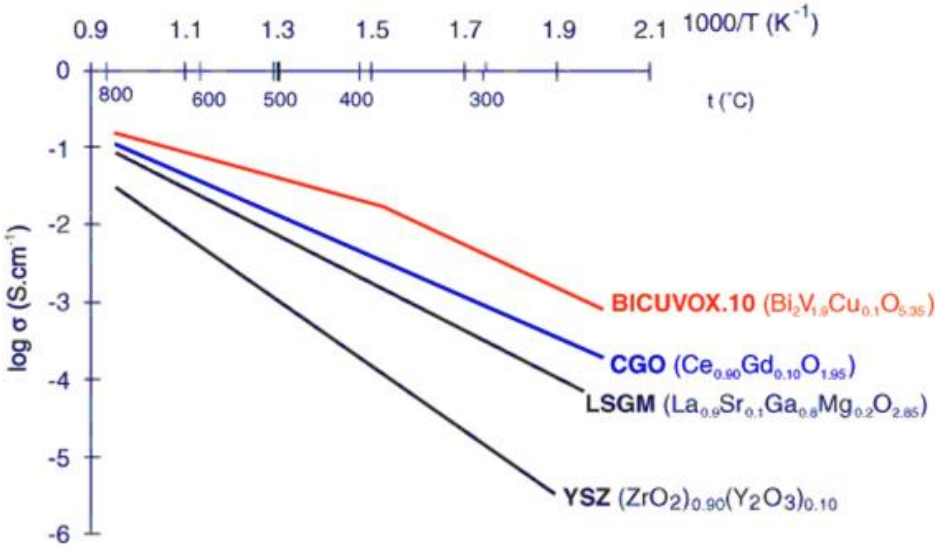

Fig 2.1 Conductivity variation with temperature of some common electrolytes [66]

The undoped ceria has poor ionic conductivity ($\sigma \sim 10^{-5}$ Scm^{-1} at 600 °C) due to lack of oxygen vacancies [67]. Therefore, doping of ceria, with either trivalent or divalent cations or a combination of the two, can increase its conductivity in the intermediate temperature range [68-83]. These dopants have lower valence than Ce^{4+}, which introduces oxygen vacancies to maintain the overall charge neutrality. After appropriate doping, oxygen vacancies are created in the crystal lattice, as shown in **Fig 2.2**. These dopants increase the ionic conductivity of ceria by producing oxygen vacancies, as shown in the following equations using the Kröger – Vink notation:

$$\mathrm{Re}_2 O_3 \xrightarrow{2CeO_2} 2\,\mathrm{Re}'_{Ce} + 3O_O^X + V_O^{\cdot\cdot} \tag{2.1}$$

$$MO \xrightarrow{CeO_2} M''_{Ce} + O_O^X + V_O^{\cdot\cdot} \tag{2.2}$$

Re'_{Ce} represents Re^{3+} occupying Ce^{4+} sites and $\mathrm{M}''_{\mathrm{Ce}}$ represents M^{2+} occupying Ce^{4+} sites, thus generating oxygen vacancies ($V_O^{\cdot\cdot}$).

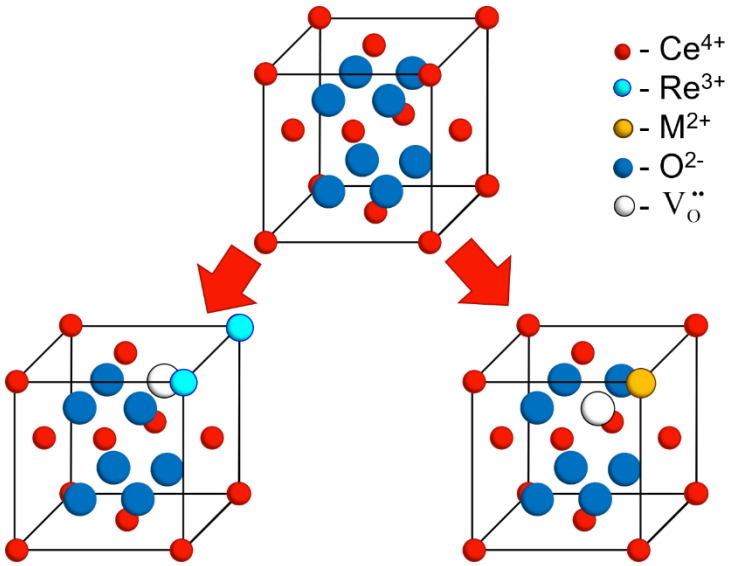

Fig 2.2 Representation of oxygen vacancy formation by trivalent (Re^{3+}) and divalent (M^{2+}) cation doping in ceria lattice

The CeO_2 exists in fluorite cubic structure (F-type) with the $Fm\bar{3}m$ space group, and this structure is stable up to the melting point of CeO_2, i.e., 2400 °C. This structure has four CeO_2 formula units per unit cell with Ce at 4a sites with coordinates (0, 0, 0) and O at 8c sites with coordinates $(\frac{1}{4},\frac{1}{4},\frac{1}{4})$. Each Ce^{4+} is surrounded by 8 oxygen as its nearest neighbour and 12 Ce^{4+} ions as its next nearest neighbour, as represented in **Fig 2.2.** Doping introduces vacant sites in the lattice, which are crucial for the movement of oxygen ions for enhancing ionic conductivity. The transportation of oxygen ions in the lattice is a thermally activated process. Oxygen ion conductivity in CeO_2 is driven by a hopping mechanism via an oxygen vacancy defect [18]. The electrical conductivity of doped ceria depends on many factors such as synthesis procedure [68], sintering [71, 84], dopant concentration [46], co-doping [77, 78, 85, 86], grains and grain boundaries [87], etc. Doped ceria electrolytes have been synthesized using different techniques such as sol-gel [88], co-precipitation method [84, 89-91], polyol method [64, 86], hydrothermal method [67, 92-94], glycine nitrate process [95, 96], citrate-nitrate combustion method [97, 98], etc. Further, sintering conditions play important role in deciding

the density and conductivity of the electrolyte [71, 84].

2.2 Chemical nature of dopants and conductivity

The most common dopants in ceria are samarium (Sm) and gadolinium (Gd) [69, 99]. Other than these dopants, La, Nd, Y, Dy, Ca, Sr, Mg, etc., are also effective dopants in ceria [46, 69, 90, 100-104]. Doping of lower valence cations in ceria generates oxygen vacancies to balance the charge imbalance in crystal lattice. This increases the ionic conductivity of ceria. However, this conductivity increases only to a certain extent of dopant concentration (about 10-20 mol % of dopant) depending on the solubility of dopants in the host structure. Usually, the solubility of dopants depends on many factors, such as differences in ionic radii, charges, and crystal structure of hosts and dopants, etc. Moreover, after a certain limit of vacancies, defect interactions increase, and defect clusters are formed. This reduces the number of mobile oxide ions, which alters the ionic conductivity [46]. The ideal dopant concentration depends on the dopant ionic radii and synthesis procedure [46]. **Fig 2.3** illustrates how the dopant ionic radii influence the ionic conductivity of ceria for the divalent and trivalent atoms [105]. With increasing ionic radii, the conductivity increases, reaches a maximum, and then decreases. The ionic radii of Gd^{3+} and Sm^{3+} are closer to Ce^{4+}; therefore, these dopants show maximum ionic conductivity with minimum lattice distortion. The conductivity of divalent ions is lesser than that of trivalent ions because of the larger ionic radii mismatch between divalent ions and cerium ions (Ce^{4+}) [18].

Chaubey *et al.* [69] investigated the properties of doped ceria electrolytes ($Ce_{0.9}Ln_{0.1}O_{1.95}$, Ln=Nd, Sm, and Gd) prepared using the solid-state reaction method. Gd-doped ceria showed the highest conductivity of the three dopants compared to Nd and Sm-doped ceria. Anjaneya *et al.* [106] prepared various doped ceria $Ce_{0.8}Ln_{0.2}O_{2-\delta}$ (Ln= Y^{3+}, Nd^{3+}, Gd^{3+}, Sm^{3+}, and La^{3+}) electrolytes using citrate complexation method. The Sm-doped ceria samples showed the highest conductivity of 9.73×10^{-4} Scm^{-1}, followed by Gd-doped ceria (4.41×10^{-4} Scm^{-1}) at 350

°C, having activation energy of 0.86 and 0.87 eV, respectively.

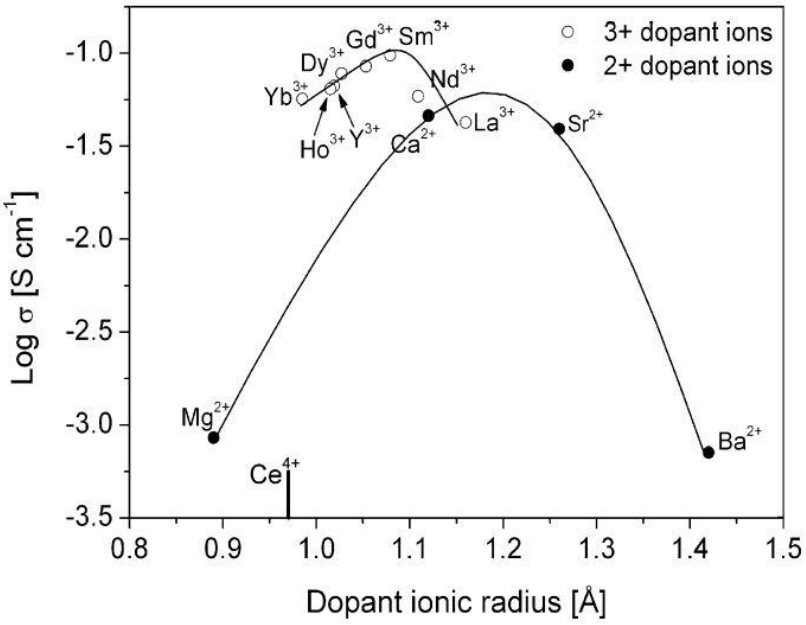

Fig 2.3 Ionic conductivity of cerium oxide vs dopant ionic radii for divalent and trivalent dopants at 800 °C [105]

Kuharuangrong [107] studied the ionic conductivity of ceria doped with Gd, Dy, Sm, and Er. The maximum conductivity for Sm-doped ceria is reported. Also, it has been found that the conductivity decreases with increasing Er concentration, and an additional phase appears in the electrolyte. Steele [108] reported that Gd-doped ceria has a higher ionic conductivity than Sm and Y-doped ceria. It has also been reported that the presence of impurities (such as SiO_2) has a negative effect on the grain boundary conductivity. So, it is good to use high-purity powders to synthesize the electrolyte. **Table 2.1** shows the ionic conductivity of different dopants in ceria, along with references. It is also crucial to develop affordable modified ceria as an electrolyte with sufficient ionic conductivity [109]. Alkaline earth ions, namely Mg^{2+}, Ca^{2+}, and Sr^{2+} doped ceria, are also widely studied for their suitability as electrolytes [74, 110-112]. The alkaline earth metals are economical, readily available, and more environmentally friendly than rare earth metals [100, 113, 114]. Among alkaline earth metals, Sr^{2+} is preferred in ceria-based electrolytes because Sr doping reduces the average binding

energy among cations and anions [115, 116]. Oxygen ions migrate more easily in electrolytes with lower average binding energy.

Table 2.1 Compositions, synthesis method, conductivity, measuring temperature, activation energy along with references of different dopants in ceria

Compositions	**Synthesis method**	**σ (Scm^{-1})/Temp. (°C)**	**E_a (eV)**	**Ref.**
$Ce_{0.9}Pr_{0.1}O_{2-\delta}$	EDTA-citrate method	1.21×10^{-3} /700	1.28	[73]
$Ce_{0.8}Dy_{0.2}O_{2-\delta}$	Solution combustion method	2.06×10^{-1} /800	0.54	[72]
$Ce_{0.95}Sr_{0.05}O_{2-\delta}$	Citrate-nitrate auto-combustion method	3.26×10^{-3}/500	0.87	[100]
$Ce_{0.8}Yb_{0.2}O_{1.9}$	Solid state reaction method	1.30×10^{-2}/800	0.59	[71]
$Ce_{0.8}Nd_{0.2}O_{1.9}$	Molten salt method	0.15×10^{-2}/600	0.87	[117]
$Ce_{0.9}Ca_{0.1}O_{1.9}$	Combustion method	1.70×10^{-2}/800	0.84	[118]
$Ce_{0.8}Er_{0.2}O_{2-\delta}$	Citric acid–nitrate combustion method	1.8×10^{-2}/700	0.55	[119]
$Ce_{0.8}Sm_{0.2}O_{2-\delta}$	Sucrose-pectin modified sol-gel method	1.01×10^{-2}/700	0.89	[120]
$Ce_{0.9}Gd_{0.1}O_{2-\delta}$	Hydrothermal method	1.80×10^{-2}/800	0.61	[92]

2.3 Effects of co-doping in ceria

Co-doping of ceria with divalent (Sr^{2+}, Ca^{2+}, Mg^{2+}) and trivalent (Gd^{3+}, Sm^{3+}, La^{3+}) cations is known to enhance its performance as an electrolyte by improving the number of oxygen vacancies [77, 86, 103, 121-124]. This method can improve the conductivity of the ceria by increasing the number of available oxygen vacancies, avoiding local ordering of these vacancies, avoiding reduction of ceria in the reducing atmosphere, and decreasing the activation energy [46, 119, 125]. However, there are contradicting studies that show the negative effects of co-doping [46]. Many researchers have investigated different co-doped and tri-doped ceria, such as $Ce_{0.85}Gd_{0.10}Sr_{0.05}O_{2-\delta}$ [80], $Ce_{0.76}Pr_{0.08}Sm_{0.08}Gd_{0.08}O_{2-\delta}$ [126], $Ce_{0.8}Sm_{0.08}Gd_{0.12}O_{2-\delta}$, $Ce_{0.8}Sm_{0.045}Gd_{0.05}Yb_{0.105}O_{2-\delta}$ [127], $Ce_{1-2x}Gd_xLa_xO_\delta$ and $Ce_{1-2x}Gd_xNd_xO_\delta$ (x = 0.1, 0.25) [128], $Ce_{0.8}Gd_{0.2-x}Pr_xO_{1.90}$ (x = 0-0.10) [77], $Ce_{0.9}Gd_{0.09}M_{0.01}O_{2-\delta}$ (M = Fe, Cu) [129], (La, Cu) co-doped Ceria [130], $Ce_{0.95-x}Dy_xCa_{0.02}Bi_{0.03}O_{2-\delta}$ [131],

$Gd_{0.1}Pr_xCe_{0.9-x}O_{1.90}$ [132], $Ce_{0.8}Yb_{0.1}Sm_{0.1}O_{2-\delta}$ [133], $Ce_{0.83}Sm_{0.085}Pr_{0.085}O_{2-\delta}$ [134], $Ce_{0.8}Gd_{0.2-x}Sm_xO_{1.9}$, (x= 0.01, 0.03 and 0.05) [135], $Ce_{0.8}Sm_{0.2-x}Zn_xO_{2-\delta}$ (x = 0, 0.02, 0.04, 0.08, and 0.16) [136]. **Table 2.2** shows some co-doped ceria-based compositions with conductivity and activation energies.

Table 2.2 Compositions, conductivity, measuring temperature and activation energies with references

Compositions	**Temp. (°C)**	**Conductivity (Scm^{-1})**	**Activation energy (eV)**	**Ref.**
$Ce_{0.85}La_{0.10}Sr_{0.05}O_{2-\delta}$	600	2.72×10^{-3}	0.96	[80]
$Ce_{0.85}Gd_{0.10}Sr_{0.05}O_{2-\delta}$	600	6.78×10^{-3}	0.96	[80]
$Ce_{0.5}Gd_{0.25}Nd_{0.25}O_{\delta}$	600	0.178×10^{-1}	-	[128]
$Ce_{0.8}Yb_{0.1}Sm_{0.1}O_{2-\delta}$	750	2.7×10^{-2}	-	[133]
$Ce_{0.83}Sm_{0.085}Pr_{0.085}O_{2-\delta}$	600	2.63×10^{-2}	0.68	[134]
$Ce_{0.8}Gd_{0.15}Sm_{0.05}O_{1.9}$	600	1.078×10^{-2}	-	[135]
$Ce_{0.8}Sm_{0.16}Zn_{0.04}O_{2-\delta}$	800	5.7×10^{-2}	-	[136]
$Ce_{0.85}Dy_{0.1}Ca_{0.02}Bi_{0.03}O_{1.915}$	700	3.53×10^{-2}	0.79	[137]
$Ce_{0.825}Sm_{0.0875}Gd_{0.0875}O_{2-x}$	600	2.23×10^{-2}	-	[138]
$Ce_{0.82}La_{0.06}Sm_{0.06}Dy_{0.06}O_{2-\delta}$	550	2.7×10^{-2}	0.82	[139]
$Ce_{0.80}Pr_{0.10}Dy_{0.10}O_{2-\delta}$	500	6.8×10^{-3}	0.80	[140]
$Ce_{0.8}Y_{0.18}La_{0.02}O_{2-\delta}$	800	5.7×10^{-2}	0.87	[141]
$Ce_{0.80}Nd_{0.18}Y_{0.02}O_{1.90}$	600	1.28×10^{-2}	1.03	[142]
$Ce_{0.8}Pr_{0.1}La_{0.1}O_{2-\delta}$	600	1.92×10^{-2}	0.46	[143]
$Ce_{0.8}Y_{0.12}Cu_{0.08}O_{1.86}$	800	2.90×10^{-2}	0.75	[144]
$Ce_{0.9}Gd_{0.075}Y_{0.025}O_{1.95}$	600	2.59×10^{-2}	0.59	[145]

Abdullah *et al.* [128] prepared the $Ce_{1-2x}Gd_xLa_xO_{\delta}$ and $Ce_{1-2x}Gd_xNd_xO_{\delta}$ (x = 0.1, 0.25) ceramics using composite mediated hydrothermal method. The maximum conductivity achieved was 1.78 Scm^{-1} at 600 °C for $Ce_{0.5}Gd_{0.25}Nd_{0.25}O_{\delta}$. The conductivity of doped ceria depends on the ionic radii and dopant concentration. Ceria doped with gadolinium and yttrium was found to have a conductivity of 2.59×10^{-2} Scm^{-1} at 600 °C [145]. $Ce_{0.8}Sm_{0.2-x}Zn_xO_{2-\delta}$ (x = 0, 0.02, 0.04, 0.08, and 0.16) powders were synthesized using the sol-gel method [136]. Adding Zn not only improved the sintering behaviour of the doped ceria but also improved the conductivity (5.7×10^{-2} Scm^{-1} at 800 °C) for $Ce_{0.8}Sm_{0.16}Zn_{0.04}O_{2-\delta}$. Ramesh *et al.* [134] reported that

$Ce_{0.83}Sm_{0.085}Pr_{0.085}O_{2-\delta}$ samples, synthesized using a sol-gel process, possess higher conductivity, i.e., 2.63×10^{-2} Scm^{-1} at 600 °C with an activation energy of 0.68 eV. This conductivity was higher than the singly doped ceria samples $Ce_{0.8}Sm_{0.2}O_{2-\delta}$ (9.95×10^{-3} Scm^{-1}) and $Ce_{0.8}Pr_{0.2}O_{2-\delta}$ (7.99×10^{-3} Scm^{-1}) in similar processing conditions. The co-doping effect results in an increase in the number of oxygen vacancies. Further, the oxygen diffusion is faster in these systems due to minimum distortion in the lattice. The combined effect of these two factors increases the conductivity of co-doped ceria systems.

Bi *et al.* [146] studied the effect of MgO addition on the electrical properties of $Ce_{0.9}Gd_{0.1}O_{2-\delta}$ electrolyte. The electrolyte was prepared using the Glycine Nitrate Process. The samples sintered at 1200°C showed the highest conductivity of 8.11×10^{-2} Scm^{-1} at 800 °C. The electrolyte $Ce_{0.9}Gd_{0.1-x}Fe_xO_{2-\delta}$ prepared using co-precipitation method showed a relative density of 95 % for pellets sintered at 1000 °C for 5 h [147]. Although the electric conductivity of $Ce_{0.9}Gd_{0.07}Fe_{0.03}O_{2-\delta}$ is more than $Ce_{0.9}Gd_{0.1}O_{2-\delta}$ but, its performance deteriorates as compared to $Ce_{0.9}Gd_{0.1}O_{2-\delta}$ due to the reduction of Fe^{3+} in reducing atmosphere.

Coles-Aldridge *et al*. [138] prepared two different series of samarium and gadolinium co-doped ceria using a citrate complexation process: $Ce_{1-2x}Sm_xGd_xO_{2-x}$ (x = 0.125, 0.1, 0.0875, 0.075 or 0.05) and $Ce_{0.825}Sm_xGd_{0.175-x}O_{1.9125}$ (x = 0.175, 0.14, 0.105, 0.0875, 0.07, 0.035 or 0). The highest conductivity was shown by a total dopant concentration of 17.5 mol% in the former series and a Sm: Gd ratio of 50:50 in the later series at temperatures of 550 °C and above. $Ce_{0.825}Sm_{0.0875}Gd_{0.0875}O_{2-x}$ showed higher and stable conductivity of 2.23×10^{-2} Scm^{-1} at 600 °C. Tian *et al.* [148] reported an increase in conductivity from 0.026×10^{-3} Scm^{-1} at 800 °C for $Ce_{0.8}Sm_{0.2}O_{1.9}$ to 0.043×10^{-3} Scm^{-1} for Bi_2O_3 doped $Ce_{0.8}Sm_{0.2}O_{1.9}$. The synthesis method also affects the co-doping effect, the solid solubility limit, and other parameters. The $Ce_{0.8}Gd_{0.2-x}Sm_xO_{1.9}$ (x= 0.01, 0.03, and 0.05) prepared using two different methods (controlled co-precipitation and Pechini method) showed completely different results [135].

$Ce_{0.8}Gd_{0.15}Sm_{0.05}O_{1.9}$ prepared using the Pechini method showed a total conductivity of 1.078×10^{-2} Scm^{-1} at 600 °C while the same sample prepared using the controlled precipitation method showed a total conductivity of 0.504×10^{-2} Scm^{-1} at 600 °C. The Pechini method produces powders with large surface area and lower particle distribution, resulting in dense electrolytes (>95 % relative density).

Venkataraman *et al.* [139] successfully incorporated three dopants (La^{3+}, Sm^{3+} and Dy^{3+}) in ceria using the sol-gel auto-combustion method. The highest conductivity of 2.7×10^{-2} Scm^{-1} is observed at 550 °C for the composition $Ce_{0.82}La_{0.06}Sm_{0.06}Dy_{0.06}O_{2-\delta}$. The tri-doped ceria compound $Ce_{1-x}(Pr_{1/3}Sm_{1/3}Gd_{1/3})_xO_{2-\delta}$ prepared by sol-gel auto combustion method showed ionic conductivity of 1.86×10^{-2} Scm^{-1} at 600 °C [126]. The presence of three different dopants increases the number of available oxygen vacancies, enhancing the conductivity of tri-doped samples.

However, Kasse *et al.* [149] reported no significant change in conductivity by Sm^{3+} and Nd^{3+} co-doped ceria compared to singly doped ceria. Similar results were reported for Sr^{2+} and Er^{3+} co-doped ceria [119]. Therefore, not all dopant pairs enhance the conductivity of ceria. Also, the conductivity only increases up to a specific dopant concentration. Increasing the dopant concentration above this level results in the formation of defect clusters with oxygen vacancies or the secondary phase, which reduces the number of available oxygen vacancies and the conductivity [122].

2.4 Effect of process parameters on the conductivity of ceria-based electrolytes

Synthesis of any electrolyte is crucial to get good quality and homogeneous powder for highly dense (> 90 %) and highly conducting electrolytes. The densification behaviour of an electrolyte is influenced by the particle size of initial ingredients, mesoporosity, and homogeneity of the powder [99]. Even the grain size affects the conductivity of the doped ceria

electrolytes. Lenka *et al*. [150] reported that bulk conductivity decreases with decreasing grain size, and grain boundary conductivity increases. The ionic conductivity increases by one order of magnitude for nanosized grains than micron-size grains [151]. Different process routes influence the above factors. Thus, different routes have been used by researchers to synthesize ceria-based electrolytes such as sol-gel method [88, 152], co-precipitation method [84, 89, 90], hydrothermal method [92, 93], Pechini method [135, 153], solid-state reaction method [154], glycine nitrate process [95, 155], polyol method [64, 86], cellulose templating method [156], and spray pyrolysis method [157, 158]. The solid-state reaction method is the easiest method to prepare desired phased materials. However, this method has the disadvantage of inhomogeneity, prolonged reaction time, and requirement of high processing temperature (~1600 °C). This method also results in poor sintering of the final product. The wet chemical synthesis method promotes high homogeneity and fine particle size. This leads to high reactivity of powder and decreases the sintering temperature of ceramic. **Table 2.3** shows the variation in conductivity of gadolinium-doped ceria prepared using different methods. It can be clearly seen that different conductivity and density values are reported for different synthesis methods for the same composition.

Table 2.3 Synthesis method, sintering temperature, relative density, conductivity, measuring temperature along with references for gadolinium doped ceria

Synthesis method	**Sintering temp. (°C)**	**Relative density (%)**	**σ (Scm^{-1})/Temp (°C)**	**Ref.**
Pechini method	1450	96	3.2×10^{-3}/600	[99]
EDTA citrate complexation method	1200	99	1.6×10^{-2}/700	[159]
Glycine Nitrate Process	1350	-	9.7×10^{-3}/700	[95]
Hydrothermal synthesis	1500	-	1.80×10^{-2}/800	[92]
Composite Mediated Hydrothermal method	800	-	9.3×10^{-4}/600	[94]
Urea-based homogeneous co-precipitation method	1500	95	1.1×10^{-2}/650	[89]
Co-precipitation method	1300	-	2.0×10^{-2}/600	[160]

Sol-gel method	1500	-	1.9×10^{-2}/600	[88]
Polyol method	1300	> 95	3.25×10^{-2}/800	[64]

Gondolini *et al.* [161] prepared nanocrystalline powder of ceria with varying amounts of gadolinium doping using the microwave-assisted polyol method. The polyol-mediated method produces fine particles without any agglomeration. Microwave heating influences the morphological properties of Gd-doped ceria, such as lower sintering onset temperature and higher density than the conventionally sintered samples. The lower sintering temperature was due to the increase in the specific surface area, which resulted in increased powder reactivity. The higher ionic conductivity was attributed to the slightly higher density of these powders. The $Ce_{0.9}Gd_{0.1}O_{2-\delta}$ and $Ce_{0.8}Gd_{0.2}O_{2-\delta}$ prepared using a modified sol-gel technique showed electrical conductivity between 1.9×10^{-2}-5.5×10^{-2} Scm^{-1} in the temperature range 600 – 800 °C. This increased conductivity may be due to the improved gadolinium ion mobility in very dense structures [88]. While $Ce_{0.9}Gd_{0.1}O_{2-\delta}$ prepared using urea-based homogeneous co-precipitation method showed conductivity of 1.1×10^{-2}-4.1×10^{-2} Scm^{-1} in the temperature range 650-800 °C [89].

Kim *et al.* [68] prepared $Re_{0.1}Ce_{0.9}O_{2-\delta}$ and $Re_{0.2}Ce_{0.8}O_{2-\delta}$ (where Re = Gd, Sm, and Nd), using four different synthesis methods such as solid-state method, hydrothermal method, co-precipitation method, and combustion method. The ionic conductivity of ceria not only depends on the dopant type and their content but also on the synthesis method. The samples prepared using the co-precipitation method showed the least density, while those prepared using the combustion method showed the highest density. The highest conductivity was observed for $Nd_{0.2}Ce_{0.8}O_{2-\delta}$ samples prepared using a combination of two different powders (co-precipitation and combustion method). The conductivity was about 2.5-4 times higher than single-processed powders. Anirban *et al*. [162] prepared $Gd_{0.2}Ce_{0.8}O_{2-\delta}$ using three different methods- citrate-nitrate auto-ignition, co-precipitation, and mechanical alloying method. They

observed that the samples prepared using the co-precipitation method had the smallest particle size, while the samples prepared using the auto-ignition method had the highest conductivity.

The use of precursors also affects the properties of the prepared electrolyte [163]. Ong *et al.* [118], in their study on $Ce_{0.9}Ca_{0.1}O_{1.9}$, where they prepared this electrolyte using three different fuels (citric acid, glycine, and urea), found that the use of different fuels produced different results. The best results were found for electrolytes prepared using citric acid with the highest density (>96 %) and highest conductivity (1.72×10^{-2} Scm^{-1} at 800 °C).

The sol-gel method is used to synthesize ceramics using a chemical solution that acts as the precursor to produce an integrated network (or gel). Typical precursors include metal alkoxides and metal salts, which undergo hydrolysis and polycondensation reactions. Different factors influence the resultant products in sol-gel synthesis, such as type of solvents, temperature, precursors, catalysts, pH, additives, fuel-to-oxidant ratio, and mechanical agitation [95, 159]. The sol-gel method has a short reaction time, better control at stoichiometry, and low synthesis cost [88]. The sol-gel method followed by self-combustion yields better results and higher conductivity [164].

Recently, the sonochemical method has been found to be an effective tool for the low-temperature synthesis of nanoparticles. This technique has been used for the synthesis of SOFC components such as YSZ electrolyte [165], CGO electrolyte [157, 166, 167], NiO-CGO anode [168], cathodes such as SSC ($Sm_xSr_{1-x}CoO_3$)-CGO [169], and LSC($La_{0.6}Sr_{0.4}CoO_3$)/SDC(Sm_2O_3-doped CeO_2) [170]. Generally, sonication takes place at a high frequency (20 kHz) and high power (200-1000 Watts (W)). In ultrasonication, cavitation occurs due to the pressure generated by the ultrasonic waves. Ultrasonic waves generate, enlarge, and collapse these bubbles. The formation and collapse of these bubbles increases the temperature (5000 °C) and pressure (1000 atm) with fast heating and cooling rates (10^{10} $°Cs^{-1}$)

within the vicinity of these bubbles, which induces immense stress on the liquid. This stress is enough to break the agglomerates into smaller fragments and prevent nucleation [167]. Thus, with the assistance of ultrasonication, particle agglomeration can be prevented, and uniform particle distribution can be achieved [171-173]. The use of sonication resulted in better dispersion of particles within the solution. This will be associated with better particle size control, lower sintering temperature, and higher density. The sol-gel method combined with ultrasonication is expected to produce highly homogeneous powders, resulting in denser electrolytes with high conductivity.

It is evident from the above literature survey that gadolinium-doped ceria is widely explored as an electrolyte for ITSOFC applications. Since it is chemically stable at the operating temperature range (500-800 °C). It has high electrical conductivity of 0.5×10^{-2} Scm^{-1}- 2.0×10^{-2} Scm^{-1} with low activation energy [64, 92, 94, 160]. The conductivity of doped ceria electrolytes is dominated by grain boundaries, especially at temperatures less than 600 °C [174]. Grain boundary conductivity is known to be influenced by several variables, including dopant type, grain boundary surface area, and impurities along the grain boundaries [174, 175]. These factors can reduce the ionic conductivity of ceria. The impurities in the ceria, such as siliceous impurities, get segregated along the grain boundaries and form an amorphous phase [87, 176]. The alkali earth metal cations such as calcium and strontium are known to reduce grain boundary resistivity by removing these impurities and thus increasing the conductivity of doped ceria electrolytes [121, 177-180]. Among the alkali earth metal cations, strontium is the one that is widely studied because it has low lattice binding energy and shows grain boundary scavenging effects [115, 121]. Jaiswal *et al.* reported that adding Sr increases the conductivity of lanthanum and strontium co-doped ceria by at least 20 times more than lanthanum-doped ceria [121]. Yeh *et al.* reported twice the increase in conductivity of samarium doped ceria by strontium doping [115]. Strontium is also reported as a better dopant

in increasing vacancy formation and significantly affects the grain boundaries compared to other dopants, such as barium or calcium in lanthanum-doped ceria [102]. Thus, it is crucial to develop affordable modified ceria as an electrolyte with sufficient ionic conductivity [109].

2.5 Motivation of the present study

It is important for electrolytes to have high density (>90 % of the theoretical density). Many researchers have focused on reducing the sintering temperature and increasing the density of doped ceria by different preparation methods, sintering aids, or sintering methods, but there has not been much success. There is no consistency in the observed conductivity for different synthesis methods. Further, one of the challenges with the existing doped ceria electrolyte is the reduction of Ce^{4+} to Ce^{3+} in the reducing atmosphere during the operation of the cell. This increases the electronic conductivity of the electrolyte. It may short-circuit the cell, which reduces the power density and, ultimately, the lifetime of the device. The process parameters are influenced by the particle size, homogeneity, calcined temperature, sintering temperature, and solid solubility limits of the dopants in ceria. These factors ultimately affect the density and conductivity of the final product. Therefore, the motivation of the present study is to achieve highly dense and suitable ionic conductivity electrolytes for ITSOFC applications using an ultrasound-assisted sol-gel auto-combustion synthesis method.

2.6 Objectives

Based on the above motivation, the following are the objectives of the present study:

1. To synthesize Sr and Gd doped and co-doped CeO_2 using chemical methods.
2. Samples will be characterized for their structural, thermal and electrical properties using various techniques.
3. Optimized electrolyte will be tested for its performance in real SOFC conditions.

Chapter 3

Experimental Techniques

3.1 Raw Materials

The chemicals used for the synthesis of electrolyte powders include cerium (III) nitrate hexahydrate ($Ce(NO_3)_3.6H_2O$, 99.5 %), strontium (II) nitrate ($Sr(NO_3)_2$, 99 %), and gadolinium (III) nitrate hexahydrate ($Gd(NO_3)_3.6H_2O$, 99.9 %), which were procured from Alfa Aesar. Ethylene glycol ($C_2H_6O_2$, 99 %) and citric acid ($C_6H_8O_7$, 99 %) were obtained from Loba Chemie to prepare the solution. The list of chemicals used for synthesizing fuel cells is given in **Table 3.1**.

Table 3.1 Chemicals used in fuel cell synthesis and their purpose/use along with the company name

Chemical Name	**Purpose/use**	**Company Name**
NiO	Anode	Fuel cell materials, USA
$(La_{0.6}Sr_{0.4})_{0.95}Co_{0.8}Fe_{0.2}O_{3-\delta}$ (LSCF)	Cathode	Fuel cell materials, USA
Poly(vinyl) alcohol (PVA)	Binder	Mitsubishi Chemical Performance Polymers, USA
Ethyl cellulose	Binder	Loba chemie, India
Polyethylene glycol (PEG)	Plasticizer I	Loba chemie, India
Glycerol	Plasticizer II and anti-adhesive	Loba chemie, India
Octanol-1	Defoamer	Loba chemie, India
Darvan C-N (Ammonium polymethyl acrylate)	Dispersant	Vanderbilt chemicals, USA
Terpineol	Solvent	Loba chemie, India
Silver paste/silver metal	Sealant	Ants Ceramics, India

3.2 Synthesis of doped and undoped ceria

The nitrates of the different materials used as metal precursor to prepare powders were taken in their required stoichiometric ratio. The metal precursors were dissolved in distilled water. The solution was then mixed with citric acid and ethylene glycol. The molar ratio of metal oxide: citric acid and ethylene glycol: citric acid was kept at 2:1 and 4:1, respectively, according to the earlier reports [181]. The solution was further sonicated for 60 minutes with a 10-second (s) on-off cycle. The sonicator power (Mangaldeep Tech Solutions, Mumbai, 20 kHz) was kept at 500 W. Thereafter, the solution was kept on the hot plate with continuous stirring at a temperature of 60-70 °C to remove excess water and to get the transparent dark brown coloured gel. This gel was then kept in the oven at 250 °C for self-combustion. The resulting material was calcined at 500 °C for 2 hours to eliminate any organic residue. Further, the calcined powders were uniaxially pressed into 10 mm diameter and 2 mm thick pellets in a cylindrical die by pressing at 100 MPa using a manually operated hydraulic press. These green pellets were sintered at 1450 °C for 4 h in an OKAY furnace by Bysakh and Co. Kolkata, India. The heating rate was kept at 5 °Cmin^{-1}. The compositions and their nomenclature are given in **Table 3.2**.

Table 3.2 The sample name used for different undoped, doped, and co-doped ceria

Sample Name	Composition
CeO_2	CeO_2
CG1	$Ce_{0.9}Gd_{0.1}O_{1.95}$
CG2	$Ce_{0.8}Gd_{0.2}O_{1.90}$
CG3	$Ce_{0.7}Gd_{0.3}O_{1.85}$
CS1	$Ce_{0.975}Sr_{0.025}O_{1.975}$
CS2	$Ce_{0.95}Sr_{0.05}O_{1.95}$
CS3	$Ce_{0.925}Sr_{0.075}O_{1.925}$

CS4	$Ce_{0.9}Sr_{0.1}O_{1.90}$
CG1S1	$Ce_{0.875}Gd_{0.1}Sr_{0.025}O_{1.925}$
CG1S2	$Ce_{0.85}Gd_{0.1}Sr_{0.5}O_{1.90}$
CG1S3	$Ce_{0.825}Gd_{0.1}Sr_{0.075}O_{1.875}$
CG2S1	$Ce_{0.775}Gd_{0.2}Sr_{0.025}O_{1.875}$
CG2S2	$Ce_{0.75}Gd_{0.2}Sr_{0.05}O_{1.85}$
CG2S3	$Ce_{0.725}Gd_{0.2}Sr_{0.075}O_{1.825}$

3.3 Cell fabrication

The planar anode-supported fuel cells of final diameter 20 mm were prepared by tape casting the anode (with 65 wt.% NiO and 35 wt.% $Ce_{0.9}Gd_{0.1}O_{2-\delta}$), followed by spray coating the electrolyte and then painting the cathode (with 65 wt.% $(La_{0.6}Sr_{0.4})_{0.95}Co_{0.8}Fe_{0.2}O_{3-\delta}$ and 35 wt. % $Ce_{0.9}Gd_{0.1}O_{2-\delta}$) on top of the electrolyte. The selection of electrolyte composition is based on the conductivity and other parameters as discussed in Chapter 4. The cell fabrication discussed in this section is the final optimized fabrication process. The optimization of the different components is discussed in detail in Chapter 5.

3.3.1 Tape casting of anode

NiO and CG1 were taken in the ratio of 65 wt.% and 35 wt.% to use as an anode. These powders were first ball-milled with zirconia balls in an ethanol medium for 6 h. The ball diameter is 6mm, and the powder-to-ball ratio is 1:2. The anode powder was then taken out and dried to remove ethanol. The aqueous-based anode tape was prepared by mixing the anode powder with 2 wt.% of dispersant (Darvan C-N) and DI water for about 16 h. This was followed by adding 3.9 wt.% each of type I and type II plasticizers (polyethylene glycol and glycerol, respectively) and mixing for another 2 h. Then 5.1 wt.% of binder (polyvinyl alcohol) and a few drops of defoamer (octanol) were added to the slurry, and the mixtures were milled for 1 h. The 15 wt.% PVA solution was prepared using distilled water and PVA mixed at 80 °C on a magnetic stirrer.

Then, using a doctor's blade, this slurry was cast on a Mylar film to get a green anode tape of about ~0.6 mm thickness. The height of the micrometer screw on the Doctor's blade was adjusted to 1.75 mm. This green tape was allowed to dry at room temperature for 24 h.

3.3.2 Spray coating of electrolyte

The electrolyte was spray-coated on green anode tape. First, the electrolyte powder (45 wt.%) was mixed with DI water and dispersant (6 wt.%) for 16 h in a beaker using zirconia balls on a rolling mill. After that, PEG (3.8 wt.%) was added along with PVA (15.2 wt.%) in the slurry and mixed for about 3 h. The prepared slurry was sprayed on the green tapes of the anode, of a diameter of 22 cm. This slurry was sprayed on dried anode tape using an air spray gun and a high-pressure vacuum pump. This half-cell was isostatically pressed using a hydraulic press to ensure a dense electrolyte film.

3.3.3 Co-sintering

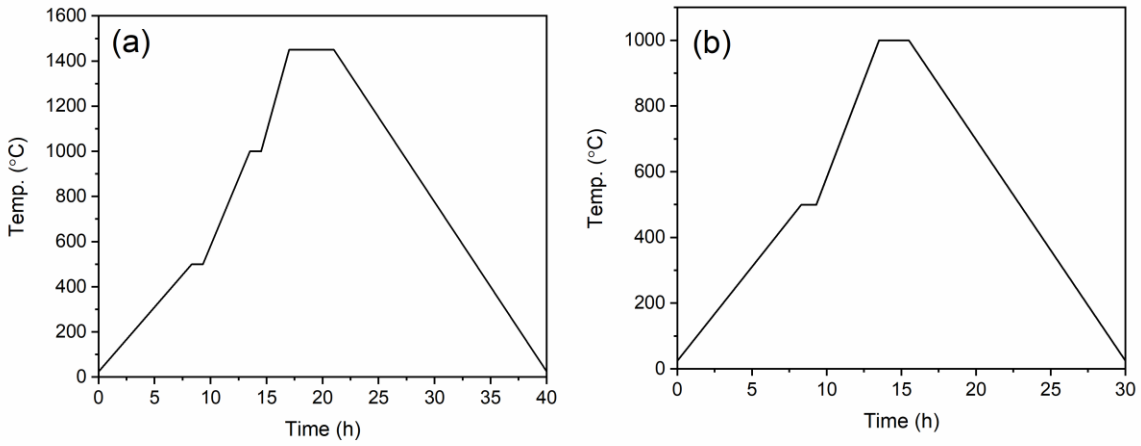

Fig 3.1 Temperature profile used for (a) half-cell co-sintering and (b) cathode sintering

The anode and electrolyte were co-sintered according to the temperature profile in **Fig 3.1 (a)**. For the organic burnout stage, the half cells were heated at 1 °Cmin^{-1} up to 500 °C. The dwell time at this stage was about 1 h. Further, the cells heated up to 1000 °C with a heating rate of 2 °Cmin^{-1} with a dwell time of 1 h. Finally, the cells were heated to 1450 °C with a heating rate

of 3 °Cmin^{-1}. The dwell time was 4 h, and the furnace was allowed to cool on its own after this stage. To ensure the flatness of the cells, CG1 plates of about 10 g weight were kept on top of the cells.

3.3.4 Cathode layer deposition and sintering

The cathode was prepared using LSCF and CG1 in the 65 wt.% and 35 wt.% ratio. These materials are chosen because they are compatible with ceria-based electrolytes and show good performance [182]. Moreover, CG1 increases the number of triple phase boundaries and, thus, enhances the cell performance [40].These powders were first ball-milled using zirconia balls and ethanol for 6 h. The cathode powder was then taken out and dried to remove ethanol. The cathode ink was prepared by mixing cathode powder with terpineol and ethyl cellulose (5 wt.%) mixture and then painted on the electrolyte. The cathode layer was sintered at 1000 °C for 2 h following the temperature profile in **Fig 3.1 (b)**. The flowchart for the complete cell fabrication has been summarized in **Fig 3.2**.

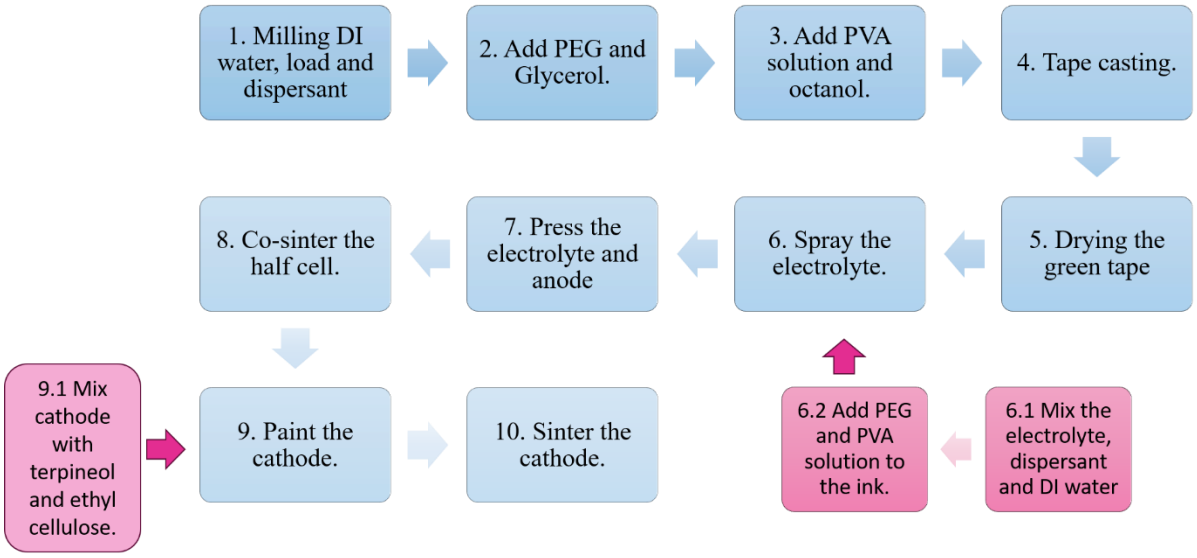

Fig 3.2 Steps followed for complete cell fabrication of planar SOFC

3.4 Characterization techniques

The sintered pellets were characterized for structural, thermal, and electrical properties to check their suitability as electrolytes for SOFC. The characterization techniques include thermogravimetric analysis (TGA), X-ray diffraction analysis (XRD), scanning electron microscopy (SEM) with energy dispersive spectroscopy (EDS), Raman spectroscopy, X-ray photoelectron spectroscopy (XPS), impedance spectroscopy, and cell testing. A brief description of the technical details of these techniques, along with their applications, is given in **Table 3.3**, followed by their extended details.

Table 3.3 The different characterization techniques, instruments used, technical details, and the information obtained

Characterization technique	**Instrument with model**	**Technical detail**	**Information obtained**
TGA	NETZSCH STA 449F3	As-prepared powder sample, RT-800 °C, Air atmosphere	Thermal stability, decomposition, moisture content, and calcination temperature
XRD	SmartLab SE (Rigaku)	Sintered and calcined powder samples, 20-90°, 2° min^{-1}, Cu Kα (λ=1.54 Å)	Crystal structure and lattice parameter
FESEM	Carl Zeiss Sigma 500 FEG-SEM	Sintered pellets, Secondary emission mode	Microstructure images and grain size
Raman spectroscopy	LabRam HR Evolution Raman Spectrometer (Horiba Scientific)	Sintered pellets, λ=532 nm	Defect analysis and oxygen vacancies
XPS	PHI 5000 VersaProbe III	Sintered samples, Al-Kα radiation with carbon peak as the reference	Ratio of Ce^{3+}/Ce^{4+}

Impedance spectroscopy	Solartron 1260A Impedance/Gain-Phase analyzer	Sintered samples, 0.1 V_{rms}, 10 Hz - 1 MHz, 100 °C - 600 °C	Conductivity measurements and activation energy
Cell testing	ZVL-100-10-80L (AMREL)	SOFC cells, H_2 + 3 % H_2O) and air, 500 °C and 600 °C.	OCV and power density

3.4.1 Thermogravimetric analysis (TGA)

Thermogravimetric analysis monitors the changes in the weight of the sample as a function of temperature. It compares the mass of the unknown sample with a reference sample (Al_2O_3). TGA was used to measure the thermal stability, decomposition, and moisture content in the material. The purpose of the TGA was to check the decomposition of organic products in the prepared powders and determine the calcination temperature of the as-prepared powders. The TGA is important to check the thermal stability of the prepared powders in the operating temperature range of fuel cells and to know the calcination temperature of the prepared powders. The analysis was conducted using a NETZSCH STA 449F3 analyzer by placing the prepared powders in alumina crucibles. The temperature range was RT-800 °C at a heating rate of 10 °Cmin^{-1} in the air atmosphere. Al_2O_3 powder was used as the reference during measurement.

3.4.2 Density measurement

It is important to have a dense electrolyte to avoid any fuel crossover and short circuit in an SOFC. The density of the sintered pellets was calculated using the Archimedes method. The theoretical density (ρ_{th}) for Gd-doped ceria, Sr-doped ceria, and Gd-Sr co-doped ceria were calculated using the following equations (3.1), (3.2), and (3.3), respectively [183]:

$$\rho_{th} = \frac{4}{N_A a^3}[(1-x)M_{Ce} + xM_{Gd} + (2-\frac{x}{2})M_O] \quad (3.1)$$

$$\rho_{th} = \frac{4}{N_A a^3}[(1-x)M_{Ce} + xM_{Sr} + (2-x)M_O] \quad (3.2)$$

$$\rho_{th} = \frac{4}{N_A a^3}[(1-x-y)M_{Ce} + xM_{Gd} + yM_{Sr} + (2-\frac{1}{2}x-y)M_O] \quad (3.3)$$

Where N_A is Avogadro's number, x is the dopant concentration, 'a' is the lattice parameter, and M_{Ce}, M_{Gd}, M_{Sr}, and M_O are the molar masses of cerium, gadolinium, strontium, and oxygen, respectively. The Archimedes' principle was employed to measure the experimental density (ρ_{ex}) of the sintered pellets as follows:

$$\rho_{ex} = \frac{W_a \rho}{W_a - W_w} \quad (3.4)$$

Here, ρ is the density of water, and W_a and W_w are the weight of the pellet in air and water, respectively. The relative density is found using the following equation (3.5):

$$\rho_{rel} = \frac{\rho_{ex}}{\rho_{th}} \times 100 \quad (3.5)$$

3.4.3 Phase analysis and Rietveld refinement

The sintered pellets were analysed for phase purity using an X-ray diffractometer (XRD). XRD is a powerful, non-destructive technique commonly employed to study the crystal structure of a material. When X-rays of wavelength 1 Å to 10 Å are directed at a crystalline material, they interact with the crystal lattice, causing constructive and destructive interference of the X-ray waves. This interference results in a diffraction pattern corresponding to specific angles and intensities. The diffraction pattern is analysed using Bragg's Law, which relates the angles of diffraction (θ), the wavelength of the incident X-rays (λ), and the interplanar spacing of crystal lattice planes (d) as shown in **Fig 3.3 (a)**. The equation of the Bragg's law is given below:

$$n\lambda = 2d\sin\theta \quad (3.6)$$

Here, n is the order of diffraction. The X-rays from a source are made to fall on the sample surface, where these rays undergo diffraction, and a diffraction pattern is recorded using a detector, as shown in **Fig 3.3 (b)**.

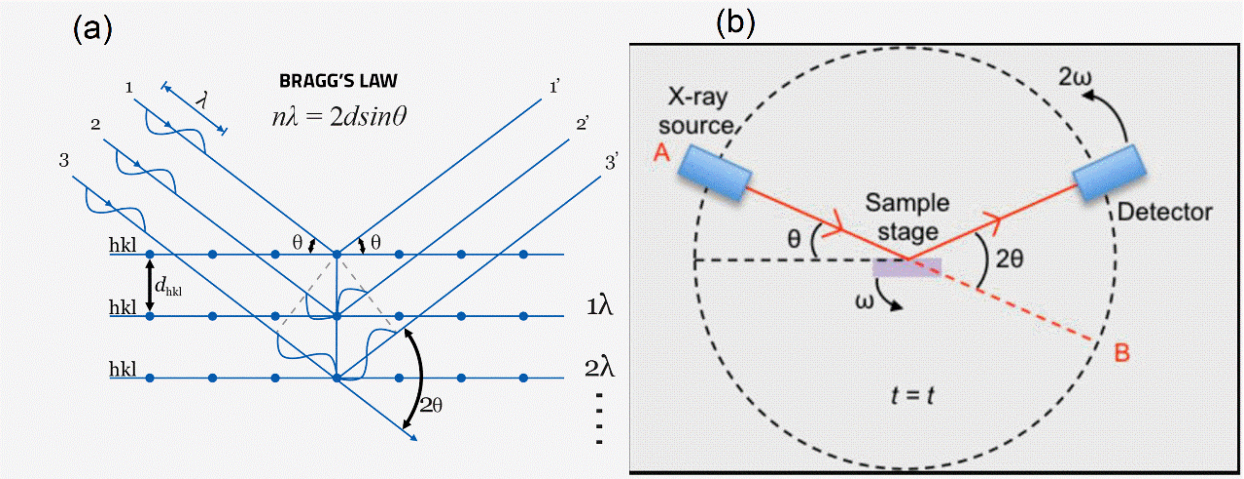

Fig 3.3 (a) Representation of Bragg's law and (b) Working principle of X-ray diffractometer [184]

The XRD data of the sintered samples was taken using SmartLab SE (Rigaku) with a scanning range of 20–90° with a step size of 0.01°. The scan speed was kept at 2° min^{-1}. The samples were analysed using monochromatic Cu K_α (λ=1.54 Å) radiations. K_β was removed using nickel filter. The quality of the beam was confirmed by performing the test run on silicon samples. The data obtained was compared with standard reference patterns from the International Centre for Diffraction Data (ICDD) database.

Rietveld refinement was performed on the XRD data to validate the phase determination further. Hugo Rietveld developed this method in the 1960s. FullProf software was utilized to perform the Rietveld refinement. The Rietveld refinement uses a least square approach to refine different parameters such as atomic positions, lattice parameters, thermal vibration, and other structural parameters. This technique uses an iterative process to match the calculated data with the experimental diffraction data.

3.4.4 Determination of microstructure

To determine the microstructure, field emission scanning electron microscopy (FE-SEM) was employed, which provides information about the size and shape of the grains. FE-SEM utilizes a field emission electron source to achieve higher-resolution imaging compared to conventional SEM. A high electrical field gradient accelerates and releases electrons from a field emission source. These primary electrons are focused and deflected by magnetic lenses within the high vacuum column to create a narrow scan beam that bombards the target, as seen in **Fig 3.4 (a)**, and the typical emissions occurring because of this bombardment are given in **Fig 3.4 (b)**. These emissions include secondary electron emission, backscattered electron emission, characteristics of X-rays (energy dispersive X-rays), Auger electrons, and other emissions depending on the depth that the electron beam can penetrate inside the sample. The sintered samples were coated with a thin layer of gold using JEC-1600 Auto fine coater (JEOL). This gold coating is required to avoid charging of the sample, which occurs due to the non-conductive nature of the ceramic samples. Field emission scanning electron microscopy (FE-SEM, Carl Zeiss Sigma 500 FEG-SEM) was employed to study the surface and fractured surface of the prepared samples. The grain size was calculated using ImageJ software. The elemental composition was determined using energy-dispersive X-ray spectroscopy (EDS, Quantax 200, Bruker). The distribution of different elements throughout the pellets was determined using area mapping of the sintered pellet to know the distribution of elements.

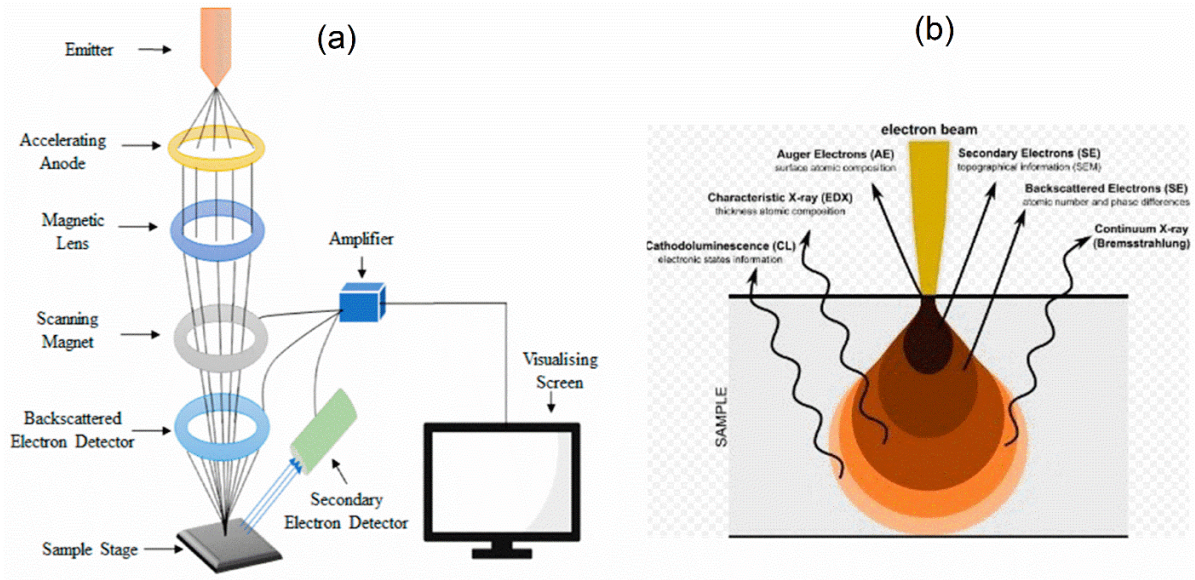

Fig 3.4 An illustration represents the (a) working of FESEM and (b) typical emission of FESEM when incident electron beam interacts with specimen [185]

3.4.5 Raman spectroscopy

Raman spectroscopy is a non-destructive technique used for studying vibrational, rotational, and other low-frequency modes in a system. The monochromatic light from the laser interacts with the sample and a part of the scattered light undergoes a change in wavelength. This shift in wavelength is called the Raman effect. The Raman effect is the outcome of inelastic scattering, in which interactions with the vibrational or rotational modes of the molecules in the sample change the energy of the scattered photons. A schematic of the Raman spectrometer is given in **Fig 3.5**. The light from a laser source is passed through a lens and a filter to the sample. The light is then directed towards the sample using a microscope objective lens after being reflected by a mirror and a filter, which acts as a mirror along this path. The same objective gathers the sample's backscattered light, which is then sent through the same filter to remove the dominant Rayleigh component and transmit the Raman-shifted wavelengths. After being transmitted to the spectrometer, the Raman scattered light is redirected by a prism onto the diffraction grating, dividing it into its individual wavelengths. The prism deflects the scattered light through a lens and onto a detector, which measures light intensity as a function

of wavelength and turns the light into a digital signal. Peaks in the Raman spectrum correspond to specific vibrational modes of the molecules, and the positions of these peaks can be used to identify the chemical composition of the material. Raman analysis was conducted using LabRam HR Evolution Raman Spectrometer (Horiba Scientific) with a Diode-pumped laser of excitation energy 532 nm. This work uses Raman spectroscopy to study the defects and oxygen vacancies in the samples.

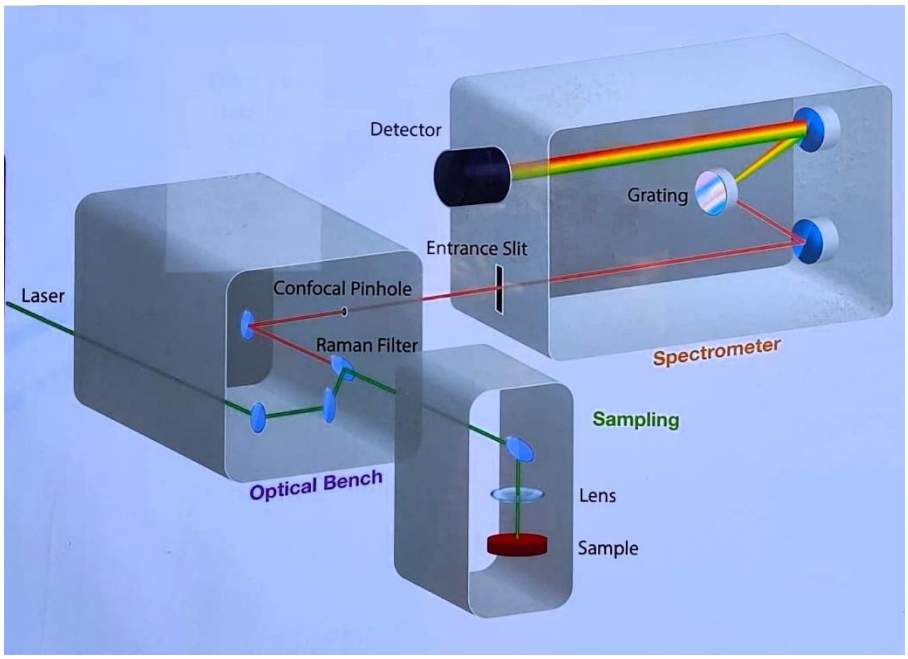

Fig 3.5 Schematic diagram of Raman spectrometer [186]

3.4.6 X-ray photoelectron spectroscopy (XPS)

XPS is a surface-sensitive technique that gives information about the elemental composition, chemical state, and electronic state of the elements within the material. XPS also gives information about the oxidation states of the elements. It works on the principle of photoelectric effect, where X-ray photons are used to eject electrons from the inner energy levels of atoms in a material. The kinetic energy and number of ejected electrons emitted from the top 1-10 nm of the surface are measured. By analysing the kinetic energy (KE) of the emitted

photoelectrons, the binding energy (BE) of the electrons can be determined using the following relation:

$$KE = h\nu - BE \tag{3.7}$$

Where hν refers to the energy of the incoming photons. The oxidation states of the elements were determined using XPS (PHI 5000 VersaProbe III) using Al-Kα radiation with carbon peak as the reference. The XPS was used to study the valence states of Ce in the present samples.

3.4.7 Impedance spectroscopy

Impedance spectroscopy involves measuring the complex impedance of a material over a range of frequencies. This spectroscopy provides valuable information about the electrical response and material characteristics. A small alternating current (ac) signal is applied to the sample across a range of frequencies. The response of the material is then analysed in terms of impedance, which is a complex quantity comprising both resistance and reactance components. The real part of impedance represents the resistance, while the imaginary part represents the reactance, indicating the capacitive or inductive behaviour. Impedance spectra of the samples usually exhibit three semicircles, as shown in **Fig 3.6**. The first semicircle corresponding to the grain resistivity (ρ_g) is observed in the higher frequency region. The second semicircle represents the grain boundary resistivity (ρ_{gb}) in the medium frequency region, whereas the third arc depicts electrolyte-electrode resistivity (ρ_e) and is observed in the lower frequency region. The diameter of the semi-circular arcs on the x-axis is used to compute the resistivities of the grains and grain boundaries. The impedance spectra were fitted to the conventional equivalent electronic circuit containing three Resistance-Constant Phase Element (R-CPE) subcircuits in series, as given in **Fig 3.7**.

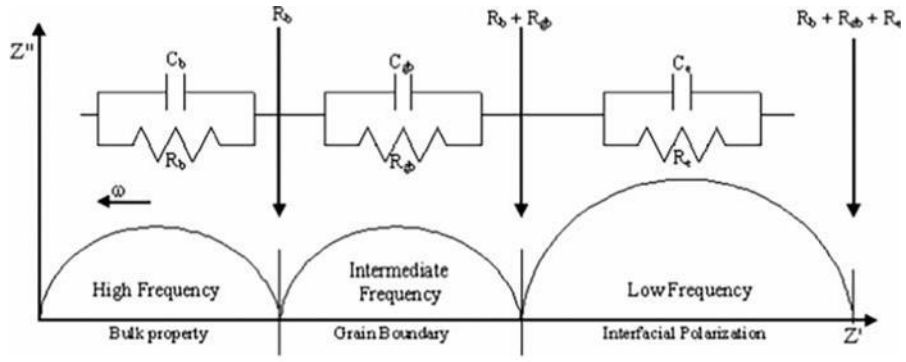

Fig 3.6 A typical impedance plot of complex (Z') vs imaginary impedance (Z") [187]

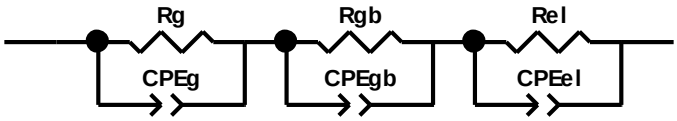

Fig 3.7 R-CPE combinations used to fit the Nyquist plots

Here, R_g, R_{gb}, and R_{el} are the grain, grain boundary, and electrode resistance, respectively. CPE_g, CPE_{gb}, and CPE_{el} are the constant phase elements of grain, grain boundary, and electrode, respectively. The conductivity is calculated using the following formula:

$$\sigma = \frac{1}{\rho} \tag{3.8}$$

Where σ is the conductivity of the sample, ρ is the resistivity of the sample. Here ρ (the total resistance) is calculated as $\rho = \rho_g + \rho_{gb}$. This resistivity was calculated using the formula:

$$\rho = R \times \frac{a}{t} \tag{3.9}$$

Where R is the total resistance, a is the cross-sectional area of the pellets, and 't' is the thickness. The slope of the following equation gives the value of activation energy (E_a)

$$\sigma T = \sigma_0 \exp\left(\frac{-E_a}{kT}\right) \tag{3.10}$$

Where T stands for temperature in Kelvin, k is Boltzmann's constant, and σ_0 is the temperature-

independent pre-exponential factor.

The electrical conductivity of the pellets was carried out at 0.1 V_{rms} within a frequency and temperature range of 10 Hz - 1 MHz (15 points per decade) and 100 °C - 600 °C, respectively, using the Solartron 1260A Impedance/Gain-Phase analyzer. Platinum paint was applied on both sides of the pellets before conductivity analysis. The sample holder used for this study was ProboStat, provided by NORECS.

3.4.8 Cell testing and Open Circuit Voltage (OCV) measurement

After cell fabrication, the complete button cells were prepared for electrochemical testing. The anode and cathode sides of the cell were painted with silver paint attached to the platinum wires for the current collection. For measurements, the sample holder used was ProboStat by NORECS, and the procedure is shown in **Fig 3.8**.

Fig 3.8 Steps for cell mounting on ProboStat sample holder for power studies [188]

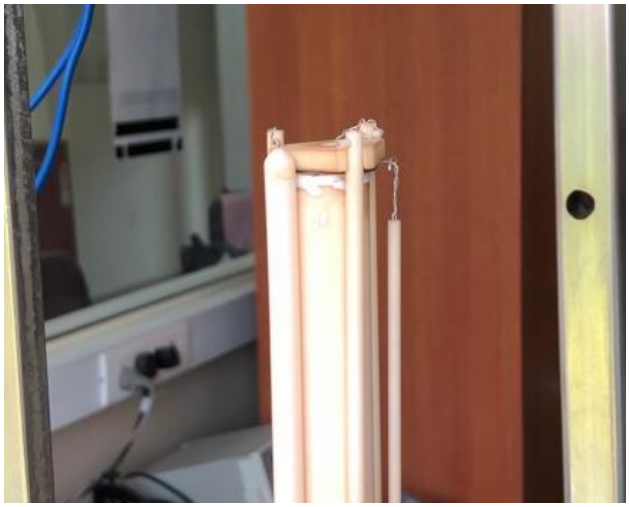

Fig 3.9 SOFC button cell mounted on the sample holder and sealed using silver rings and silver paint

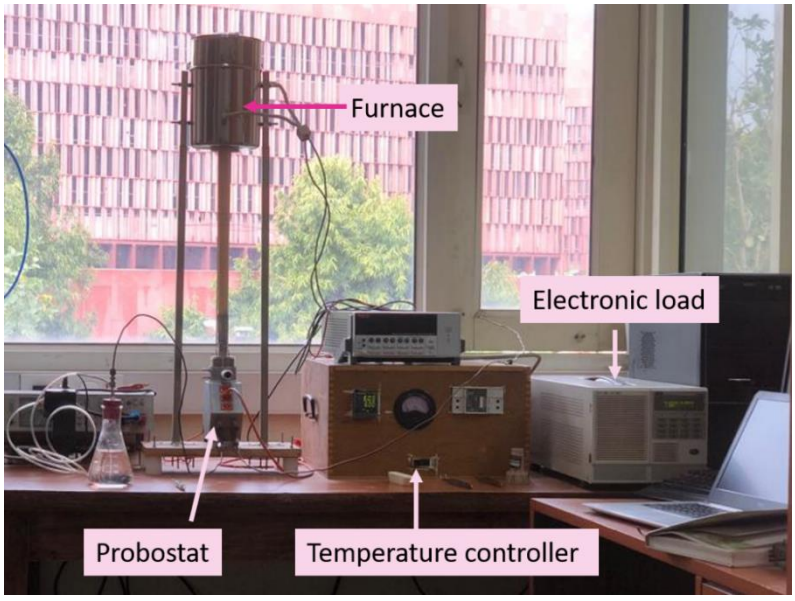

Fig 3.10 Laboratory scale SOFC test set-up used for the power studies of fabricated button cell

Fig 3.9 shows an SOFC cell mounted on the sample holder using silver rings and silver paint for sealing. The complete test setup for SOFC cell testing is shown in **Fig 3.10**. The fuel (H_2 + 3 % H_2O) with a flow rate of 30 sccm was supplied in the inner tube to the anode of the cell, and the ambient air was supplied to the cathode side. The cell was allowed to reach equilibrium before performing these measurements. The equilibrium was achieved when the OCV value stabilized, which took about ~100 min. The cell voltage, current, and power density

measurements were conducted using electronic load ZVL-100-10-80L (AMREL, USA) at temperatures between 500 °C and 600 °C.

Chapter 4

Characterization of Gd and Sr doped and co-doped Ceria Electrolyte

Undoped, doped, and co-doped CeO_2 were prepared using an ultrasound-assisted sol-gel auto-combustion synthesis method. These as prepared, calcined, and heat-treated samples were characterized for their phase purity, thermal stability, conductivity, etc. The obtained results are presented and discussed in this chapter. Furthermore, the well-characterized and optimised samples were selected to prepare the fuel cells. The characterizations of fuel cells are present in Chapter 5.

4.1 Thermal analysis

TGA was performed on the as-prepared ceramic powders to check their thermal stability up to 800 °C. The TGA curves for CG, CS, and CGS series are shown in **Fig 4.1 (a), (b),** and **(c)**, respectively. The maximum weight loss has been observed below 200 °C. The initial weight loss (<10 wt. %) is due to the evaporation of the water from the powders. The weight loss between 200 - 400 °C is due to the burning of organic residues and the decomposition of the nitrates that might be present in the powders [88]. After 400 °C, 1-3 % weight loss might occur due to the dehydration of partially hydrated oxides [92]. Beyond 500 °C, minor weight loss is associated with the conversion of partially hydrated ceria into completely dehydrated doped ceria [189]. Secondly, the weight loss (1-2 wt. %) might also be related to the loss of oxygen from the crystal lattice. Further, this loss can also be associated with one of two reasons: either Ce^{4+} reduces to Ce^{3+} or the replacement of Ce^{4+} cations by the dopant (Gd^{3+} and Sr^{2+}) cations as given in the following equation:

$$Gd_2O_3 \xrightarrow{CeO_2} 2Gd'_{Ce} + 3O_O^X + V_O^{\cdot\cdot} \quad (4.1)$$

$$SrO \xrightarrow{CeO_2} Sr''_{Ce} + O_O^X + V_O^{\bullet\bullet} \quad (4.2)$$

The loss of oxygen takes place to balance the charge in the crystal lattice. Based on TGA results, the calcination temperature is set to 500 °C for all the ceramic powders synthesized by the sol-gel auto-combustion method. The total weight loss for Gd doped ceria powder prepared by the chemical route is around 10 % (**Fig 4.1 (a)**), whereas, for CG2, it is around 17 %. The minimum weight loss is observed for Gd and Sr co-doped samples, and it is a maximum of 4 %. The maximum weight loss is observed in Gd-doped ceria, followed by Sr-doped ceria and Gd-Sr co-doped ceria, respectively. Based on TGA, the Gd-doped ceria exhibit the highest hydrophilic nature than Sr-doped and Gd-Sr co-doped samples.

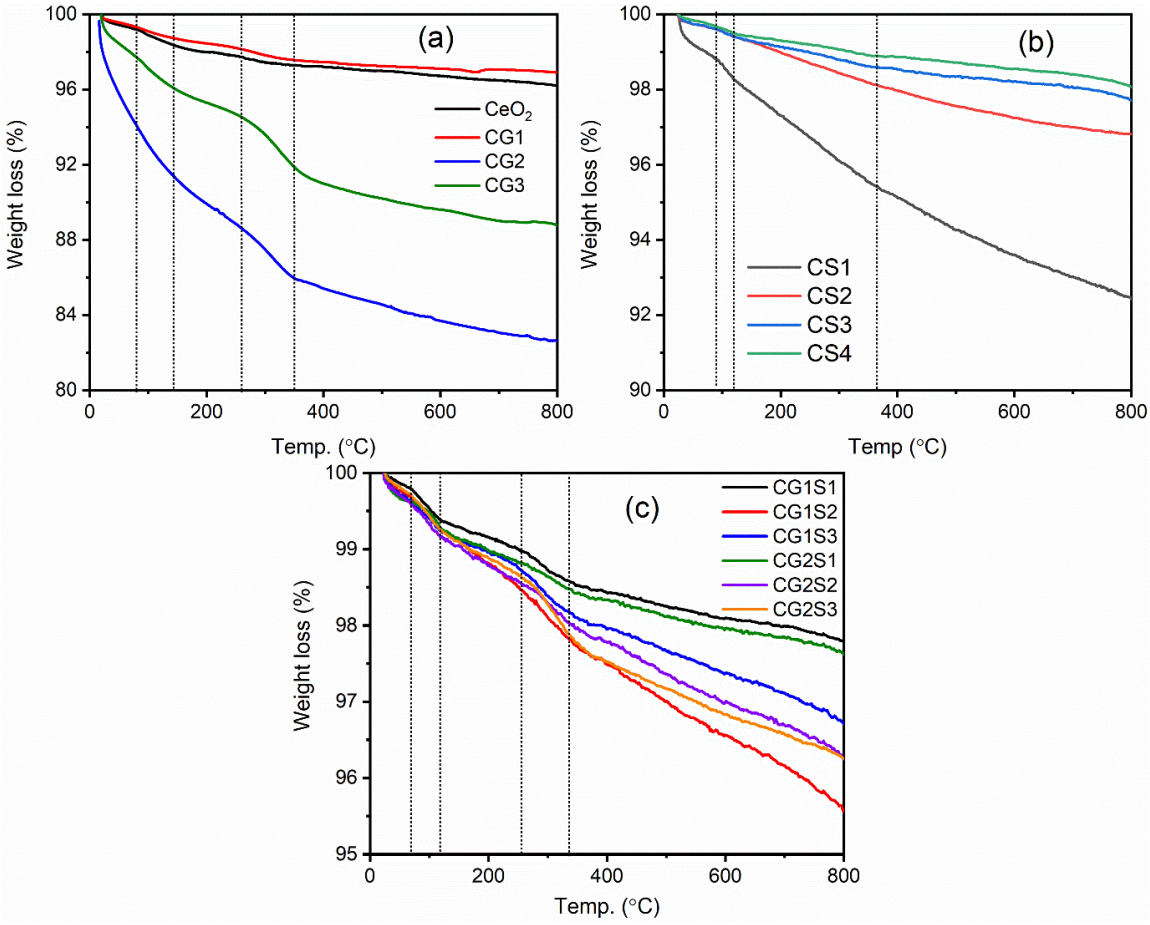

Fig 4.1 TGA of the as-prepared ceramics powders of (a) $Ce_{1-x}Gd_xO_{2-\delta}$, (x=0, 0.1, 0.2 and 0.3), (b) $Ce_{1-y}Sr_yO_{2-\delta}$ (y=0.025, 0.05, 0.075, and 0.1), and (c) $Ce_{1-x-y}Gd_xSr_yO_{2-\delta}$ (x=0.1, 0.2 and y= 0.025, 0.050 and 0.075) measured in the temperature range of RT-800 °C

4.2 Density

Density measurements have been carried out on all the sintered samples. The relative density of all the samples is more than 90 %. The use of the sol-gel auto-combustion method produces fine and homogeneous powders, leading to better sinterability of the samples with higher density. The relative densities of the different samples are given in **Table 4.1**. The maximum density (~97 %) is observed in CS1, CS2, and CS3 samples followed by CG2, CS4, CG1S1, CG1S2, and CG2S2 samples having density of ~96 %. However, the undoped sample showed density of only ~92 %. The high density of Sr-doped ceria is that the dopant Sr not only acts as a sintering aid but also creates oxygen vacancies. It causes the liquid phase sintering in the sample, as observed from the microstructural images (discussed in **section 4.4)**. The liquid phase sintering increases the density of these samples. The colour of the samples also changed from light yellowish-white to brownish after sintering. This implies that the oxidation states of cerium change during processing or the creation of oxygen vacancies by lower valence dopant cations like Gd^{3+} or Sr^{2+} in place of Ce^{4+}.

4.3 XRD analysis

4.3.1 Phase analysis and Rietveld refinement

The X-ray diffraction patterns of all the calcined samples are given in **Fig 4.2**. The full width at half maximum (FWHM) is higher for all the calcined samples than the sintered samples. The diffraction patterns are indexed with a CeO_2 structure (PDF# 34-0394) with a cubic fluorite structure with a space group $Fm\bar{3}m$. After calcination, the powders are ground and pelletized, followed by sintering at 1450 °C for 4 h. The technical details are given in the experimental section.

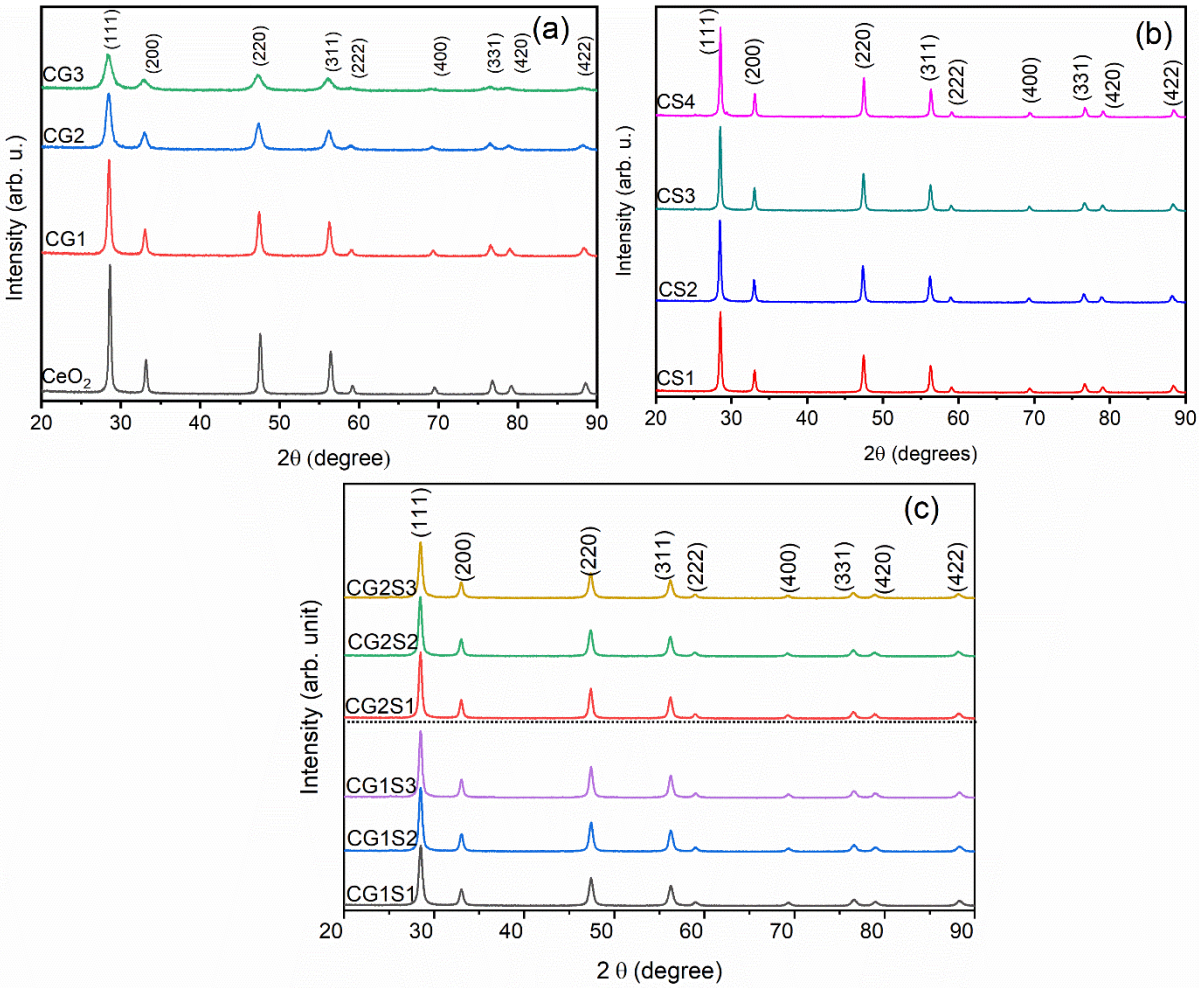

Fig 4.2 X-ray diffraction pattern of samples calcined at 500 °C of (a) $Ce_{1-x}Gd_xO_{2-\delta}$, (x=0, 0.1, 0.2 and 0.3), (b) $Ce_{1-y}Sr_yO_{2-\delta}$ (y=0.025, 0.05, 0.075, and 0.1), and (c) $Ce_{1-x-y}Gd_xSr_yO_{2-\delta}$ (x=0.1, 0.2 and y= 0.025, 0.050 and 0.075)

The phase analysis of sintered samples of the CG series are shown in **Fig 4.3 (a)**, whereas the CS and CGS series are shown in **Fig 4.3 (c)** and **Fig 4.3 (e),** respectively. **Fig 4.3 (b), (d),** and **(f)** shows an enlarged view of the (111) peak, and it represents the shifting of the diffraction pattern toward lower diffraction angles. All samples possess a cubic fluorite structure with a space group $Fm\bar{3}m$ and are indexed with a CeO_2 structure (PDF# 34-0394). This has been further confirmed by performing Rietveld refinement on the XRD data of samples, which is given in **Table 4.1** and represented in **Fig 4.4**. The experimental and calculated data show a good fit with each other, confirming the presence of a single phase even in doped samples. A

second phase is also observed in a 10 % strontium-doped ceria sample, i.e., CS4, as shown in **Fig 4.3 (a)**. The secondary phase is indexed to the $SrCeO_3$ phase (ICDD # 01-082-2370). The solubility limit of Sr into CeO_2 lies between 7.5 % and 10 %. Similar results have been reported for similar systems synthesized by the glycine nitrate process or solid-state reaction method by other researchers [96, 100, 112].

Table 4.1 Rietveld refinement parameters and grain size of samples sintered at 1450 °C for 4 h and their respective relative density

Sample name	**FWHM (°)**	**Lattice parameter, a (Å)**	**Volume, V (Å^3)**	**R_{wp}**	**R_{exp}**	**χ^2**	**Grain Size (µm)**	**Relative density (%)**
CeO_2	0.068	5.410	158.3	12.6	8.9	1.96	6.36	92
CG1	0.057	5.417	158.9	13.9	11.1	1.58	1.34	95
CG2	0.096	5.425	159.6	14.1	10.6	1.79	1.40	96
CG3	0.090	5.428	159.9	13.6	11.8	1.33	1.28	90
CS1	0.060	5.419	159.1	15.3	11.0	1.99	4.85	97
CS2	0.056	5.426	159.8	13.4	9.7	1.95	2.12	97
CS3	0.068	5.437	160.7	15.7	11.9	1.72	1.61	97
CS4	0.078	5.437	160.8	15.9	9.5	2.77	1.45	96
CG1S1	0.056	5.424	159.6	12.0	7.1	2.75	3.84	96
CG1S2	0.056	5.431	160.2	10.8	6.9	2.45	5.65	96
CG1S3	0.060	5.439	160.9	10.6	7.1	2.24	6.30	94
CG2S1	0.056	5.428	159.9	11.4	7.2	2.47	1.40	92
CG2S2	0.058	5.433	160.4	11.6	7.4	2.47	7.56	96
CG2S3	0.058	5.438	160.8	11.1	7.4	2.27	-	91

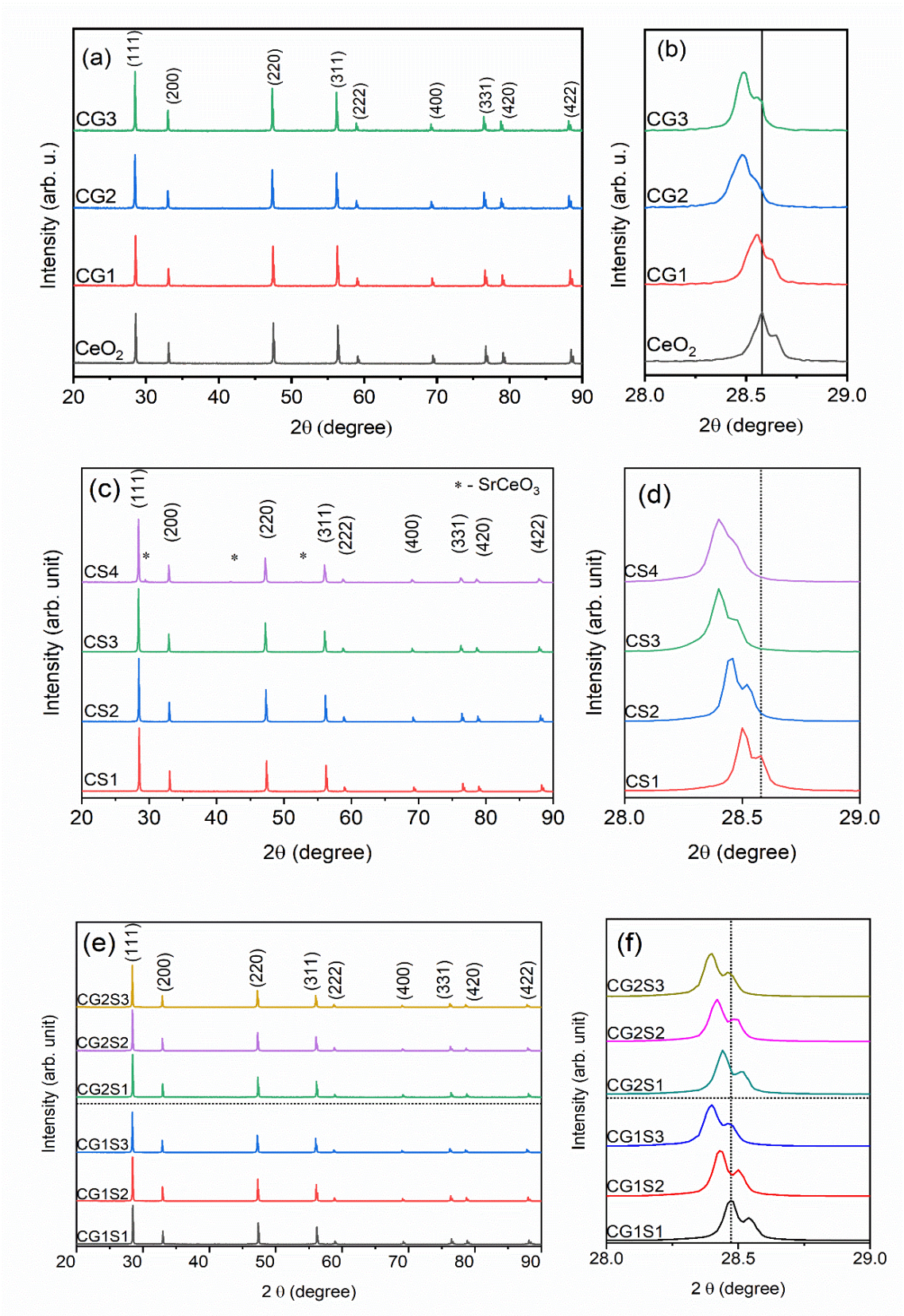

Fig 4.3 XRD of sintered samples of (a) $Ce_{1-x}Gd_xO_{2-\delta}$, (x=0, 0.1, 0.2 and 0.3), (c) $Ce_{1-y}Sr_yO_{2-\delta}$ (y=0.025, 0.05, 0.075, and 0.1), and (e) $Ce_{1-x-y}Gd_xSr_yO_{2-\delta}$ (x=0.1, 0.2 and y= 0.025,

0.050 and 0.075), and (b, d, and f) enlarged view of the peak at (111) for these samples

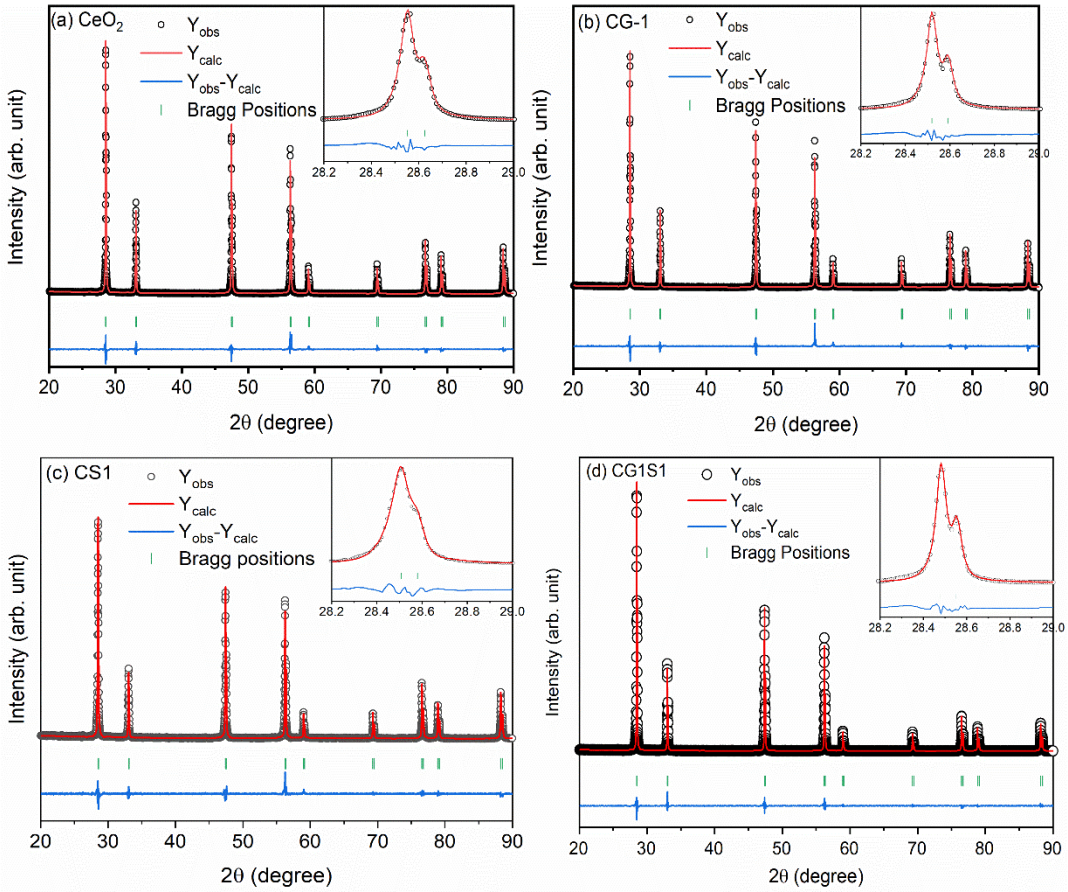

Fig 4.4 Rietveld refinement graphs of the (a) CeO_2, (b) $Ce_{0.9}Gd_{0.1}O_{1.95}$, (c) $Ce_{0.975}Sr_{0.025}O_{1.975}$, and (d) $Ce_{0.875}Gd_{0.1}Sr_{0.025}O_{1.925}$ showing the experimental and fitted data. The inset images show the zoomed in version of (111) peak

The FWHM of sintered samples is the highest (0.096 for CG2) for gadolinium doped samples (CG series, **Table 4.1**), while only a small change (0.056 for CS2) is observed in FWHM for Sr doped ceria (CS series). Almost no change is observed in co-doped ceria (CGS series). For all specimens, XRD peaks shift towards the lower diffraction angle with respect to the dopant concentration, as depicted in **Fig 4.3 (b), (d),** and **(f).** Both Gd^{3+} (1.05 Å) and Sr^{2+} (1.21 Å) have larger ionic radii than Ce^{4+} (0.97 Å) [190]. The difference in the ionic radius of the dopant and host cation causes strain in the host lattice, which leads to a shift in the XRD peaks in comparison to undoped CeO_2.

4.3.2 Solubility of the dopants in CeO_2

The variation in the lattice parameters with dopant concentration provides a good estimation of the solubility of the dopants in the host lattice. **Fig 4.5** represents the refined lattice parameter as a function of dopant concentration for sintered samples. The lattice parameter increases with the Gd substitution (see **Fig 4.5 (a))**. However, it is not linear for sintered samples at higher concentrations (x>0.20). The linearity deviated between the CG2 and CG3. This could be associated with the solid solubility limit of gadolinium in ceria that lies between x=0.20 and x=0.30. Above x=0.20, a secondary phase (C-type Gd_2O_3) may form, as discussed in **section 4.5**. However, XRD could not detect this phase due to the instrument's detection limit (~1 %). Secondly, this phase, Gd_2O_3, is closely related to the F-type CeO_2 phase [191].

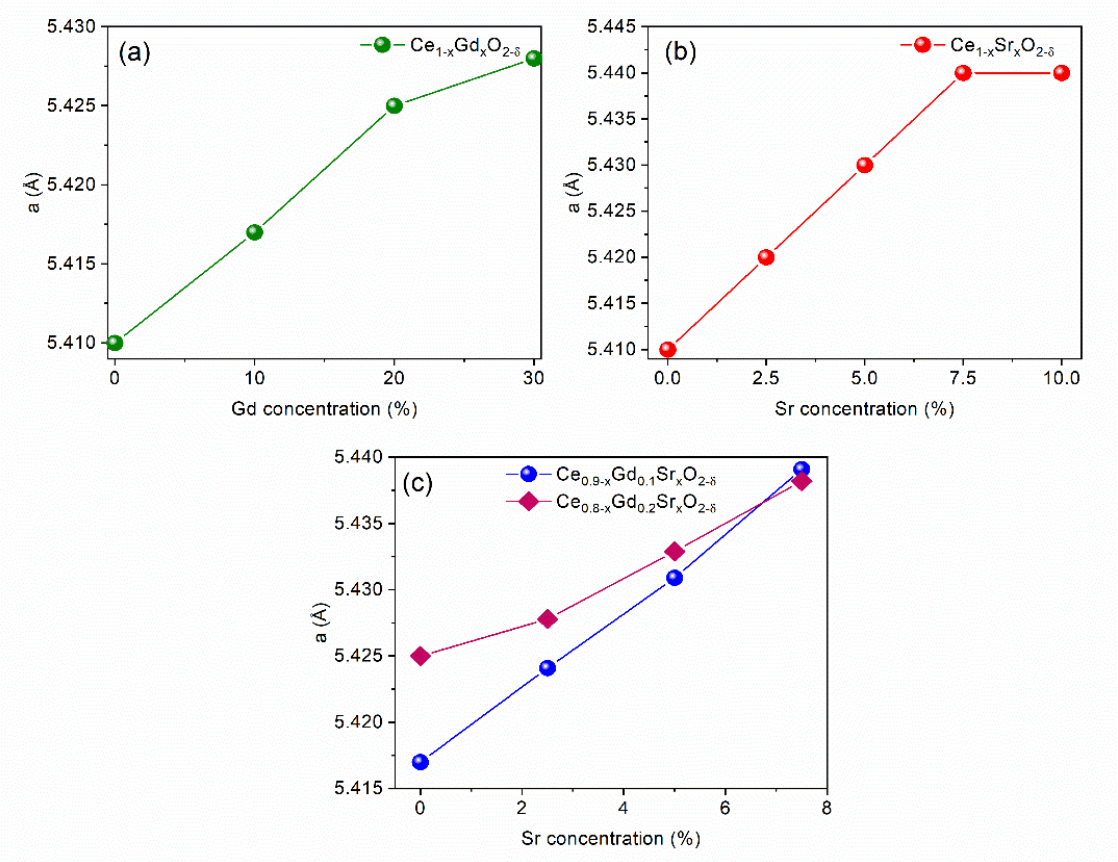

Fig 4.5 Lattice parameter variation of the sintered pellets with respect to dopant concentration for (a) Gd doped ceria, (b) Sr doped ceria, and (c) Gd and Sr co-doped ceria samples

For the CS series, the lattice parameter of the sintered samples increases linearly up to 7.5 %, as shown in **Fig 4.5 (b)**. After that, the lattice parameter remains almost constant between x=7.5 % and x=10 %. The Sr^{2+} doping induces oxygen vacancies in the crystal lattice to remove the charge imbalance caused by its addition in place of Ce^{4+}. The presence of these oxygen vacancies and the replacement of smaller Ce^{4+} (0.97 Å) by larger Sr^{2+} (1.21 Å) induces tensile strain in the lattice, increasing the lattice parameter. The change in the lattice parameter shows no variation for the CS4 sample. It indicates that the dopant is not replacing the host cation in the crystal lattice. Instead, it forms the secondary phase at a higher concentration of Sr dopants.

Based on the above results, CG3 and CS4 samples are omitted from further experiments and are not considered for co-doping studies. The larger ionic radii of Sr limit the solid solubility between 7.5 % and 10 %, whereas for Gd, the solid solubility limit is between 20 % and 30 %. The lattice parameter of the co-doped sintered samples increases linearly for CGS1 and CGS2 series, as shown in **Fig 4.5 (c)**. However, the slope is smaller for CGS2 than for CGS1. It is observed that the lattice parameter difference becomes smaller for increasing concentration of Sr and Gd. For 7.5 % Sr doped samples, the lattice parameter becomes almost similar for CGS1 and CGS2. The formation of a secondary Sr phase in CG2S3 samples is also observed in the micrographs of these samples, as discussed in the microstructural analysis.

4.4 Microstructural analysis

The SEM microstructural images to study the surface morphology of the samples are shown in **Fig 4.6, Fig 4.7**, and **Fig 4.8** for CG, CS, and CGS series respectively. The fractured surface images of the few selected samples are also taken and given in **Fig 4.9** to better understand the microstructure. For the CeO_2 sample, hexagonal-shaped grains are observed, as shown in **Fig 4.6 (a)**. As Gd concentration increases, the hexagonal grains become smaller, more uniform, and spherical in shape as seen in **Fig 4.6 (b)**. The fractured surface image of this sample shows

densely packed grains with few closed pores. CG2 sample (**Fig 4.6 (c)**) shows the bimodal distribution in the grain size. In the micrograph of CG3, several pores can also be spotted, as shown in **Fig 4.6 (d)** with yellow circles. The grain size of CeO_2 is 6.36 μm. For Gd-doped samples, the grain size lies between 1-2 μm as given in **Table 4.1**. The presence of gadolinium reduces the grain size of the sintered pellets by about three times, as seen in the SEM pictures of doped and undoped samples. Similar results are reported in the literature for doped CeO_2 [192].

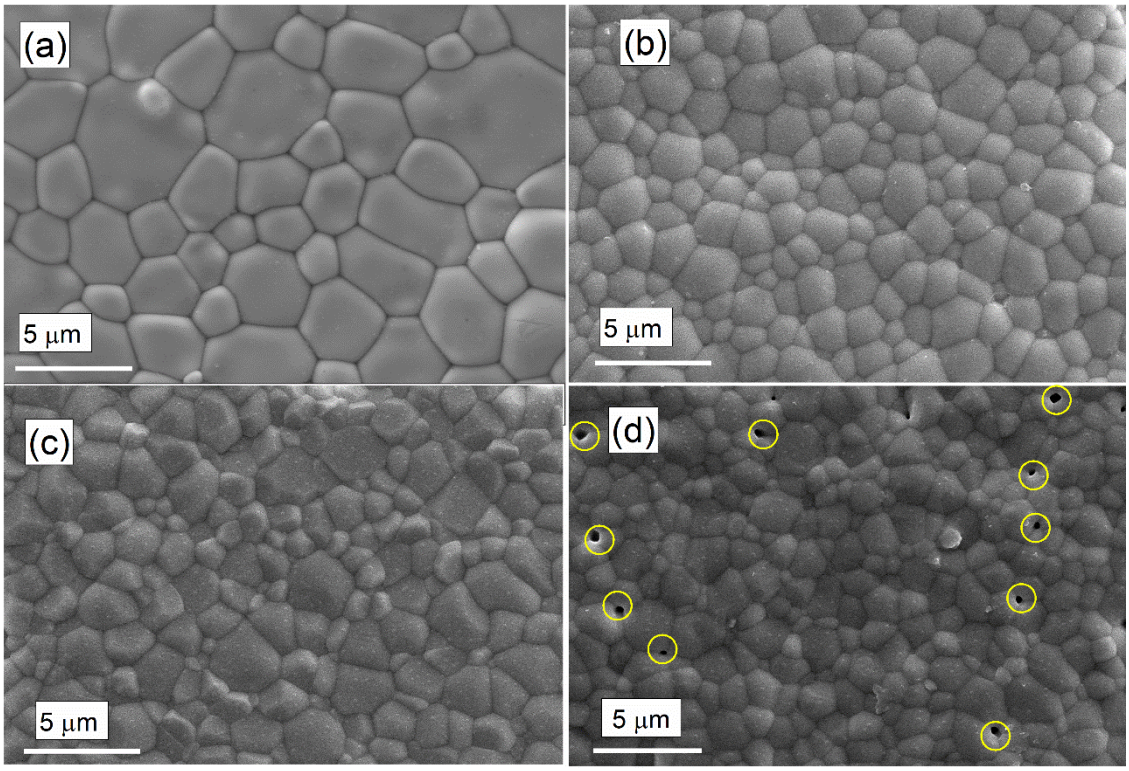

Fig 4.6 SEM images of samples taken in SE mode sintered at 1450 °C for 4 h for (a) CeO_2, (b) CG1, (c) CG2, and (d) CG3, respectively

For CS samples (**Fig 4.7**), the grains are well connected and show significantly less porosity. Sr doping not only generates oxygen vacancies but also acts as the sintering aid for ceria since the density of Sr-doped samples is better than Gd-doped samples. The grain size of sintered pellets has been calculated using Gaussian distribution and lies between 1-4 μm as given in

Table 4.1. The grain size of the sintered pellets decreases with strontium doping as it inhibits grain growth. As the dopant concentration increases, the grains become more uniform throughout the sample. Moreover, partial liquid phase sintering is also observed in all the samples. The most uniform and single phase is observed for the CS3 sample. Also, the dense microstructure is seen in the fractured surface images. Although this sample appears to be brittle, it can be seen from the chipping of the grain **(Fig 4.9 (b)).**

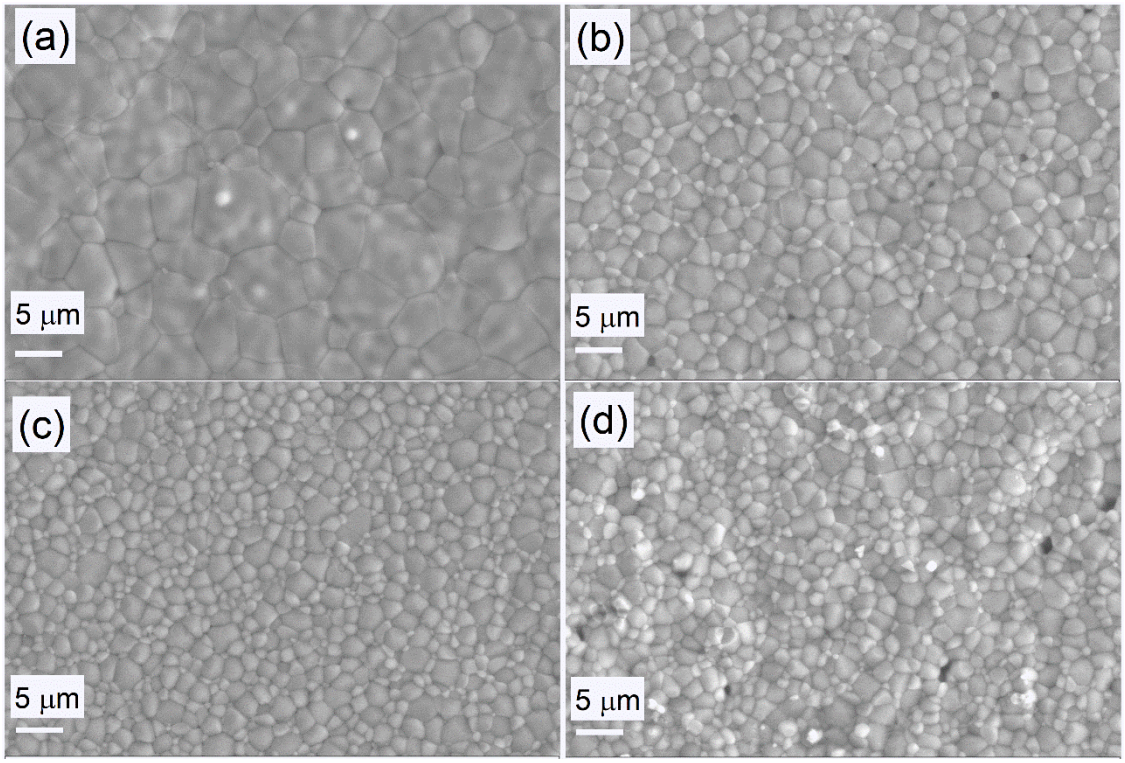

Fig 4.7 SEM microstructure of (a) CS1, (b) CS2, (c) CS3, and (d) CS4, respectively, sintered at 1450 °C for 4 h

The addition of gadolinium and strontium hinders grain growth [138, 191]. However, Sr^{2+} is more effective than Gd^{3+} doping to inhibit the grain growth of CeO_2. Sr^{2+} and Gd^{3+} doping will generate oxygen vacancies according to the "space-charge effect" [192, 193]. These oxygen vacancies would be concentrated on the surface or grain boundary region, generating a positive charge on the surface or grain boundaries. Due to this excess charge, the dopant segregates along the surface and grain boundaries. This dopant segregation reduces the grain boundary

mobility and, thus, reduces the grain size [194]. As a result, the grain boundary energy is reduced, and the driving forces for grain growth are also reduced. This could hamper the grain growth [195, 196].

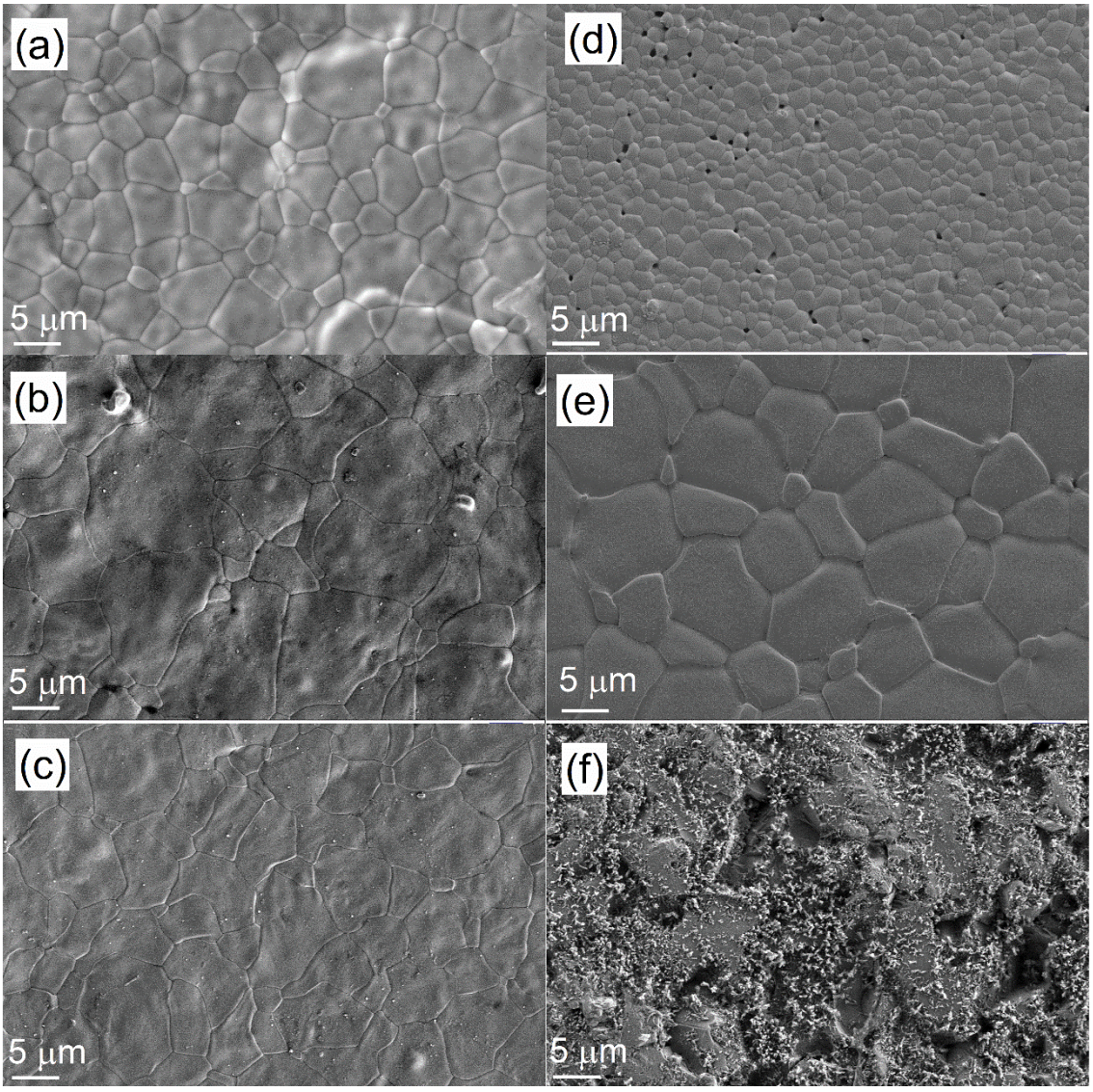

Fig 4.8 SEM microstructure of (a) CG1S1, (b) CG1S2, (c) CG1S3, (d) CG2S1, (e) CG2S2, and (f) CG2S3, respectively, sintered at 1450 °C for 4 h

For Gd and Sr co-doped ceria, all the micrographs show a dense structure **(Fig 4.8)** except for CG2S1 samples, which show a lot of porosity on the surface (**Fig 4.8** (d)). This agrees with density results (**Table 4.1**) as this sample has a lower density than other co-doped samples. All the sintered pellets show non-uniform grain distribution, increasing with the increasing Sr content. The grain size of sintered pellets lies between 1-8 μm, as given in **Table 4.1**. The

increase in the grain size agrees with the literature for the co-doped ceria systems [115, 119]. The grain size increases due to the partial liquid phase sintering. A clear liquid phase sintering is observed in the samples with high concentrations of dopants, as Sr is reported to act as a sintering aid in co-doped ceria systems [197, 198]. Even the fractured surface image shows a very dense microstructure. The CG2S3 sample appears completely melted on the surface, and grains are not discernible in this particular sample.

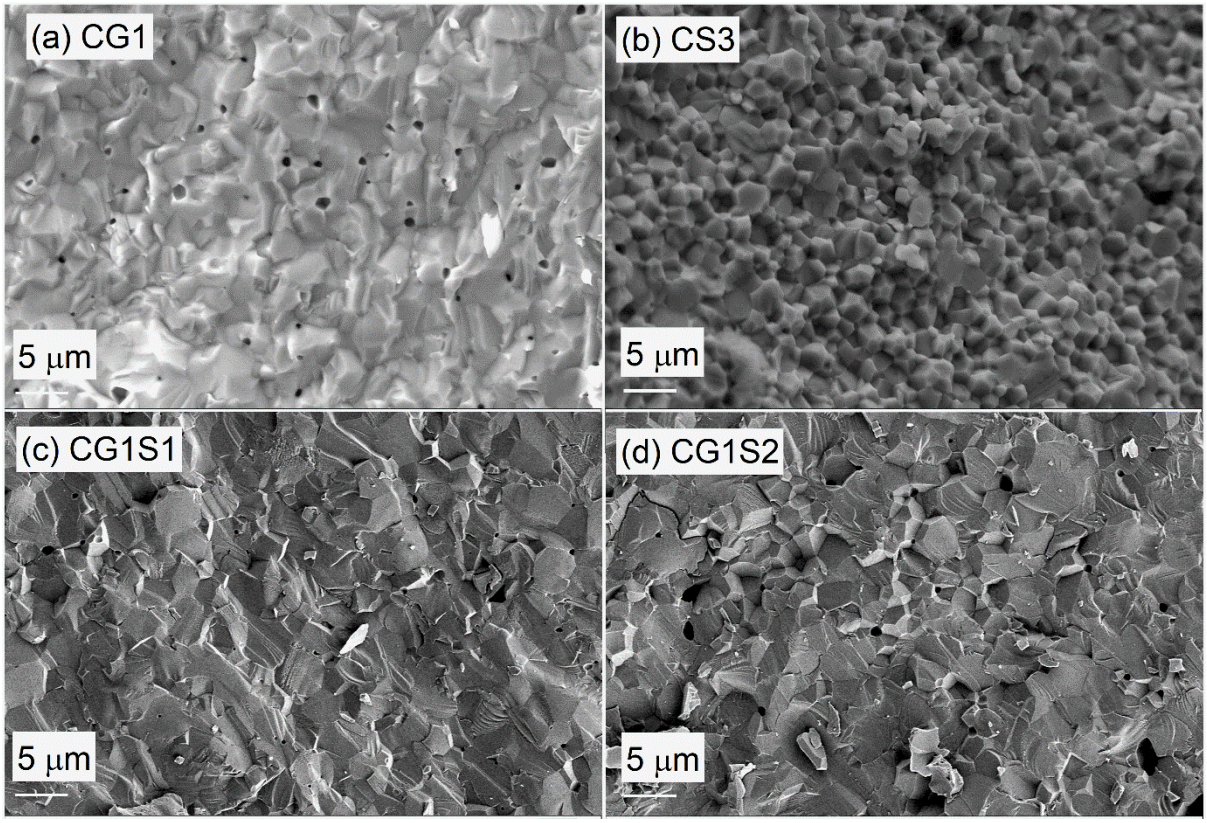

Fig 4.9 Fractured surface images of (a) CG1, (b) CS3, (c) CG1S1, and (d) CG1S2

However, a particular flower-like structure is observed on the surface of this sample. Since XRD could not detect any additional phase, this flower-like structure is probably amorphous in nature. Therefore, EDS mapping has been performed on this sample, as shown in **Fig 4.10,** and the weight % of the different elements in this flower-like structure is given in **Table 4.2**. It shows the separation of the Sr from the crystal structure in the CG2S3 sample **(Fig 4.10 (b))**. This is accounted for by the stress caused by the size difference in Sr^{2+} (1.21 Å), Gd^{3+} (1.05

Å), and Ce^{4+} (0.97 Å). The doping concentration becomes so high that strontium, having the largest ionic radii, is pushed out of the lattice. However, no separation is observed in CG1S3 (**Fig 4.10 (a)**). An even distribution of all the elements is seen on this sample surface.

Table 4.2 Weight % of the different elements of CG1S3 and CG2S3 samples

Sample ID	Ce	Sr	Gd	O	C
	Wt. %				
CG1S3	75.18	0.57	10.44	11.32	2.49
CG2S3	49.84	20.33	10.77	13.68	5.38

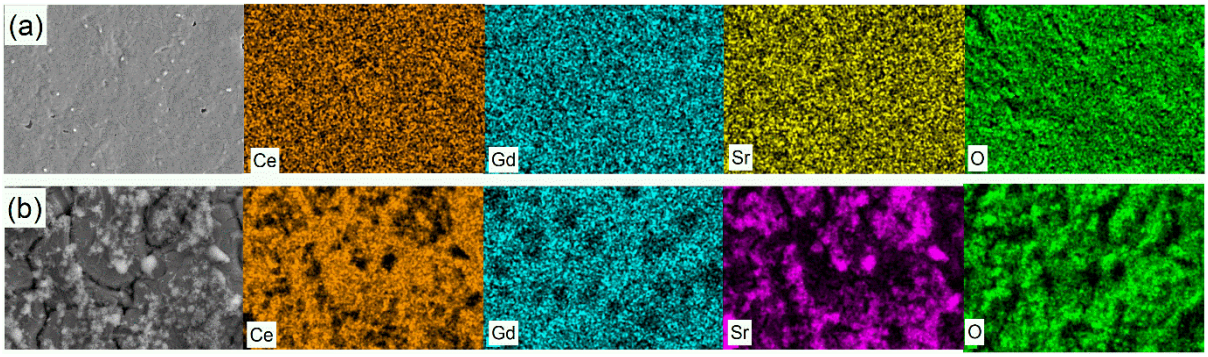

Fig 4.10 EDS spectra of (a) CG1S3 sample and (b) CG2S3 sample

The SEM micrographs of the samples show dense microstructure with reduced grain size for singly doped ceria. A small change in the grain size is observed for the Gd and Sr co-doped ceria due to the partial liquid phase sintering. The increase in the grain size reduces the number of grain boundaries in co-doped samples. This leads to the reduction in the grain boundary contribution to the impedance of the samples and thus increases the conductivity of the samples, as discussed in the conductivity section. In the case of Gd-doped ceria, the most optimized circular and uniform grains were observed for the CG1 sample (**Fig 4.6 (b)**). Similarly, in the case of Sr-doped ceria, the most uniform grain with higher density was observed for CS2 and CS3 samples, as shown in **Fig 4.7 (b)** and **(c)**. In the case of the co-doped

samples, the CG1S1 and CG1S2 samples show the most dense and uniform microstructure, as shown in **Fig 4.8 (a)** and **(b)**.

4.5 Raman analysis

Cerium oxide exhibits the cubic fluorite structure with $Fm\bar{3}m$ (O_h^5) space group. This structure has six optical phonon modes per group theory [199]. These modes correspond to the doubly degenerate transverse optical (TO) mode around ~250 cm^{-1}, the triply degenerate Raman-active mode around ~465 cm^{-1}, and the non-degenerate longitudinal optical (LO) mode around ~600 cm^{-1} [199, 200]. The TO and LO modes are infrared active. The Raman active F_{2g} mode at 465 cm^{-1} corresponds to the symmetrical stretching of the oxygen atoms around the Ce atoms. Any change in the bond length between the anion and cation due to vacancies or any other defects causes a shift or change in this Raman mode [200-202]. The Raman spectra of CeO_2 and CG series are shown in **Fig 4.11 (a)**. Multiple peaks are observed in the spectra, along with the main F_{2g} peak at 465 cm^{-1} (Peak 3 in **Fig 4.11 (a)**). With the increasing dopant concentration, the peaks become broader and merge with the neighbouring peaks. The intensity of other peaks increases compared to the F_{2g} peaks, which implies the incorporation of the dopants in the lattice. A shoulder around ~482 cm^{-1} appears alongside the F_{2g} peak. Its intensity increases with increasing dopant concentration.

Interestingly, in Sr doped ceria, only the CS2 (5 %) sample shows some small peaks alongside the central F_{2g} peak, as shown in **Fig 4.11 (b).** As the Sr concentration increases to 7.5 and 10 %, a broad shoulder appears on the high-frequency side of F_{2g}, along with a small band at 592 cm^{-1}. The intensity of this band is reduced in CS1 (2.5 %), and there is no shoulder present in this sample.

The Raman spectra of the co-doped sintered samples of the CGS series are shown in **Fig 4.11 (c)**. For this series, the spectra are quite similar to the CG series because of the high

concentration of Gd compared to Sr. Multiple peaks can be seen in the spectrum. However, these peaks become broader and merge with one another as the dopant concentration increases. The peak intensity at 465 cm^{-1} decreases with respect to other peaks. The reasons behind the appearance of the shoulder and the different peaks in the CG, CS, and CGS series are discussed in the following paragraphs.

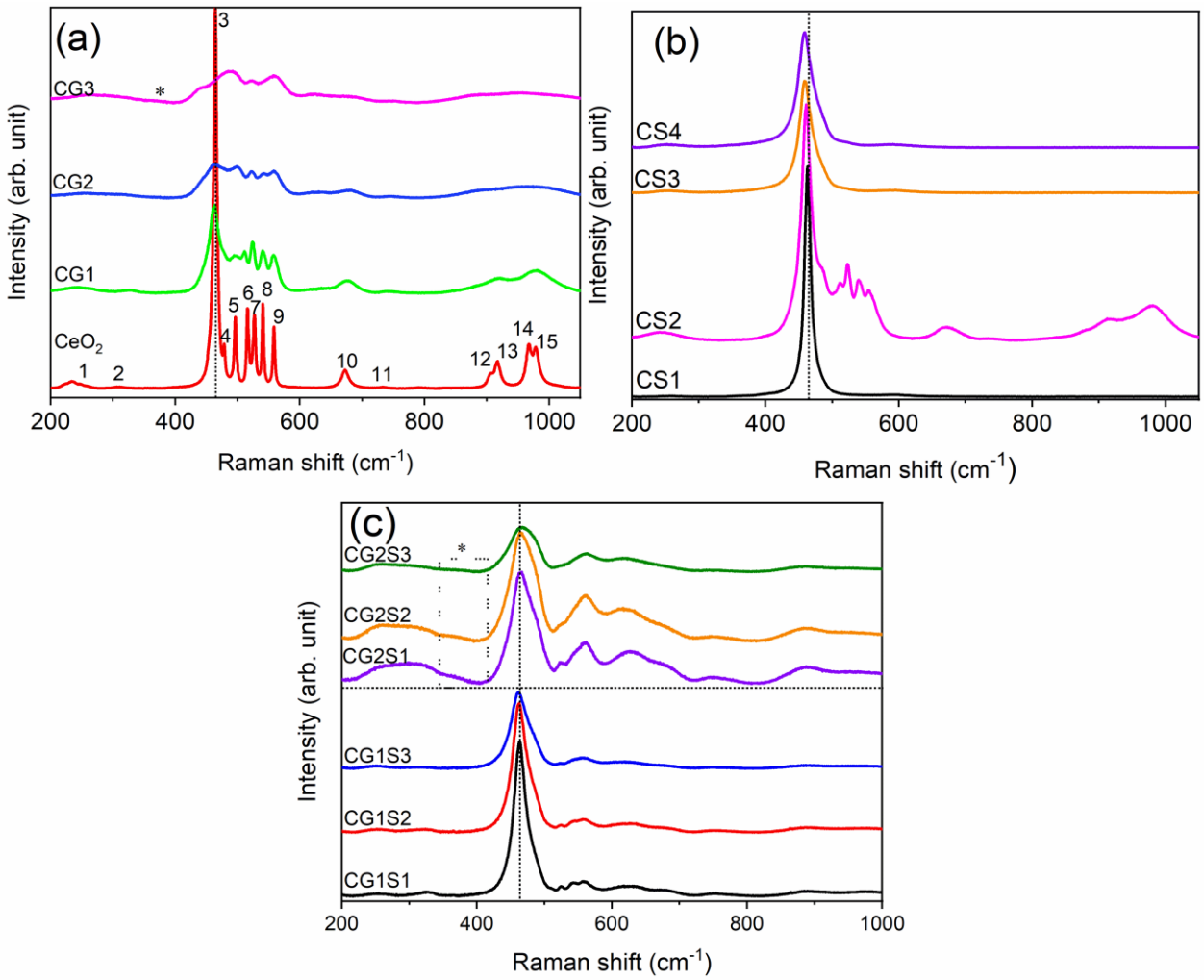

Fig 4.11 Raman spectra of sintered (a) $Ce_{1-x}Gd_xO_{2-\delta}$ (x=0, 0.1, 0.2, and 0.3), (b) $Ce_{1-y}Sr_yO_{2-\delta}$ (y=0.025, 0.05, 0.075, and 0.1), and (c) $Ce_{1-x-y}Gd_xSr_yO_{2-\delta}$ (x=0.1 and 0.2 and y=0.025, 0.05 and 0.075) ceramics measured at room temperature using λ=532 nm laser

Firstly, in the undoped CeO_2 (**Fig 4.11 (a)**), several sharp and intense peaks in the 500-600 cm^{-1} are observed, which signifies intrinsic oxygen vacancy formation in this sample and might be concentrated on the surface. These intrinsic vacancies are generated during the processing of

the undoped CeO_2 sample. At such elevated temperatures, the furnace atmosphere usually becomes reducing in nature (scarcity of oxygen), where Ce^{4+} may reduce to Ce^{3+} [203]. It is well reported in our earlier findings for different ceramics that contained transition metal oxides in their compositions [204]. The addition of Gd and Sr merged these peaks together, and they became broader (see **Fig 4.11 (a), (b),** and **(c)**). Further, Gd^{3+} and Sr^{2+} substitution at Ce^{4+} also generates extrinsic oxygen vacancies. One oxygen vacancy is created in the system for every two Gd^{3+}, replacing two Ce^{4+} ions, and one oxygen vacancy is created for every single Sr^{2+} ion, replacing the Ce^{4+} ion. The same is true for Ce^{3+} ions as well. Ce^{3+}, Gd^{3+}, and Sr^{2+} has larger ionic radii than Ce^{4+} (Gd^{3+}: 1.05 Å, Ce^{3+}: 1.143 Å, Sr^{2+}: 1.26 Å and Ce^{4+}: 0.97 Å) [205]. The reduction of Ce^{4+} to lower oxidation states, i.e., Ce^{3+} and dopants (Gd^{3+} and Sr^{2+}), can change the average coordination number of Ce along with lattice expansion [206]. This results in the appearance of multiple peaks in the Raman spectra. Further, the creation of intrinsic oxygen vacancies could be localized in the CeO_2 crystal lattice since Raman peaks are very sharp, as shown in **Fig 4.11 (a)**. On the other hand, the extrinsic vacancies created by dopants (Gd and Sr) might be delocalized (even the intrinsic vacancies) throughout the sample as Raman peaks corresponding to vacancies become broader with dopant concentration.

The doping of Sr in CS1, CS3, and CS4 reduces the concentration of Ce^{3+}, as suggested by the disappearance of peaks corresponding to the Ce^{3+}. However, in CS2 (5 %), the peaks corresponding to the Ce^{3+} reappear. This might imply that the Ce^{3+} concentration is higher in the CS2 than in other samples. This has also been confirmed by the XPS analysis, as discussed in **section 4.6.**

Out of the different peaks in the Raman spectra, the peaks positioned at ~497, 524, 542, and 560 cm^{-1} (peaks 5, 7, 8, and 9) appear due to oxygen vacancies [205, 207]. The intensity of these peaks increases with dopant concentration, which might represent the extrinsic vacancy defects caused by adding the Gd^{3+}/Sr^{2+} dopants. These different peaks appear depending on

whether the vacancy is in $Re^{3+}O_7V_O^{\cdot\cdot}$ (~497 and 542 cm^{-1}, Re^{3+} can be either Ce^{3+} or Gd^{3+}, see **Fig 4.12 (a)**) coordination sphere or $Ce^{4+}O_7V_O^{\cdot\cdot}$ (~ 524 and 560 cm^{-1}, **Fig 4.12 (b)**) coordination sphere [205].

The peak positioned at 477 cm^{-1} (peak 4) in CeO_2 shifts to 482 cm^{-1} in doped and co-doped samples because of the vibration of oxygen ions in $Re^{3+}O_8$ (**Fig 4.12 (c)**) the coordination sphere [205]. This shoulder becomes more pronounced in the CG2, CG3 samples, and CGS2 series, as seen in **Fig 4.11 (a** and **c)**. Schilling *et al.*, in their work, proposed that this peak appears if the Re^{3+} is not present in the first coordination sphere of the oxygen vacancy [205]. Banerji *et al.* also proposed that this peak appears due to the presence of the GdO_8 complex in the fluorite-type structure [206]. The increase in the intensity of this peak might also imply that defect clusters are formed.

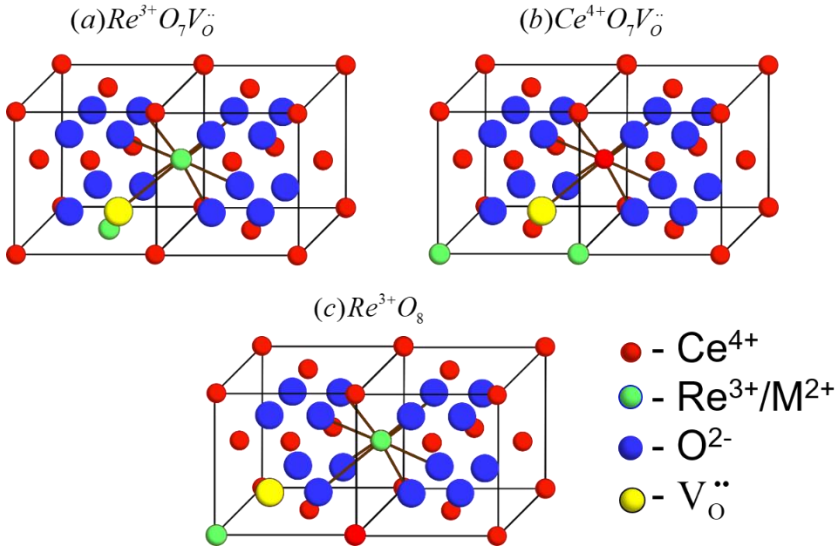

Fig 4.12 The configuration of defect clusters (a) $Re^{3+}O_7V_O^{\cdot\cdot}$, (b) $Ce^{4+}O_7V_O^{\cdot\cdot}$, and (c) $Re^{3+}O_8$

For the CG3 sample and CGS2 series, an additional band at ~370 cm^{-1} (marked with (*)) is observed, which coincides with the F_g band of the Gd_2O_3 [208]. This happens because of the double fluorite ordering in the samples. This formation of defect clusters has also been confirmed by the tunneling electron microscopy studies of CG2 by Ye *et al.* [209]. The clusters

reduce the mobility of the oxygen vacancy and decrease the overall conductivity of the sample. However, no such peak appears in other samples. The peak near 682 cm^{-1} (peak 10) appears when the oxygen atoms form the Frenkel defects by moving to the octahedral interstitial sites in these defect complexes [201, 210].

The Raman peaks at ~236 cm^{-1} (peak 1) in CeO_2, which shifts to 250 cm^{-1} in doped and co-doped ceria, possibly due to the doubly degenerate TO mode. This mode is IR active, but adding the dopant introduces the point defects and makes it Raman active [202]. Similarly, the peak at 624 cm^{-1} might be the non-degenerate LO mode, which becomes active because of the dopants. However, Filtschew *et al.*, in their work, reported that these peaks might also appear because of surface defects [211]. The peak at ~320 cm^{-1} and 516 cm^{-1} (peaks 2 and 6) may appear because of the surface or subsurface oxygen vacancies, as explained by Schilling *et al.* [205]. The two broad bands appearing between 800-1000 cm^{-1} (peaks 12-15) are due to the peroxides and superoxides formed by the absorption of the oxygen on the surface vacancies [205, 211]. Besides these, one small peak of ~750 cm^{-1} (peak 11) is also observed in all samples. No appropriate assignment for this peak could be found in the literature.

From the Raman analysis, one can get insight into the structural distortions and the defects that arise due to the doping, e.g., the oxygen vacancies attached to different crystal units in the undoped ceria are localized and can be easily identified by sharp peaks. Meanwhile, as the dopant concentration increases, the localized oxygen vacancies are mixed up with the delocalized oxygen vacancies, and distinguishability between those peaks diminishes in the Raman spectra. Also, the presence of an additional peak at 370 cm^{-1} in few samples has been able to establish the formation of nanodomains corresponding to the Gd_2O_3 structure that cannot be detected by XRD of the samples.

4.6 XPS analysis

The XPS analysis is conducted to confirm the presence of Ce^{3+} and oxygen vacancies in CeO_2, CG1 samples, and CS series. These samples are chosen as they show anomalies in the Raman spectra. The electron core level XPS spectrum of Ce3d levels in the range of 875 to 925 eV is shown in **Fig 4.13.** Two sets of spin-orbit multiplets are observed: *u* and *v*. The multiplet, *u*, corresponds to the spin-orbit split $3d_{3/2}$, whereas *v* corresponds to the $3d_{5/2}$ spin-orbit split. The peaks *u, v, u″, v″, u‴*, and *v‴* represent the Ce3d spectrum for Ce^{4+} as reported earlier, whereas the peaks *u′* and *v′* correspond to the Ce3d spectrum for Ce^{3+} [212]. As previously reported, these peaks are observed in the XPS spectrum [213, 214]. The peaks are deconvoluted, and the respective binding energies are presented in **Table 4.3**.

A semi-quantitative analysis is performed on the Ce3d XPS spectra to determine the effect of Gd and Sr doping on the oxidation states of Ce. The spectral weights of Ce^{3+} and Ce^{4+} have been calculated using equations (4.3) and (4.4), respectively.

$$Ce^{3+} = A_{u'} + A_{v'} \tag{4.3}$$

$$Ce^{4+} = A_u + A_v + A_{u''} + A_{v''} + A_{u'''} + A_{v'''} \tag{4.4}$$

The fraction of Ce^{3+} is calculated as follows:

$$f_{Ce^{3+}} = \frac{Ce^{3+}}{Ce^{3+} + Ce^{4+}} \tag{4.5}$$

The fraction of Ce^{3+} in CeO_2, CG1, CS1, CS2, and CS3 is 15, 24, 13, 16, and 11 %, respectively. The results of the above analysis indicate that the samples contain some Ce^{3+} ions, even an undoped CeO_2 sample. The presence of Ce^{3+} in CeO_2 is about 15 %, while in CG1 it is 24 %. This implies the addition of Gd increases the amount of Ce^{3+} in the samples. However, in the Sr-doped sample, this number initially decreases (for CS1) and then increases (for CS2) and

again decreases (for CS3). Similar results have also been observed in Raman spectra. As shown in **Fig 4.11 (b)**, the peaks corresponding to the Ce^{3+} are not present in CS1 and CS3 samples. Since both Raman and XPS are surface-sensitive techniques, the presence of Ce^{3+} in the bulk may be different than that on the surface [185].

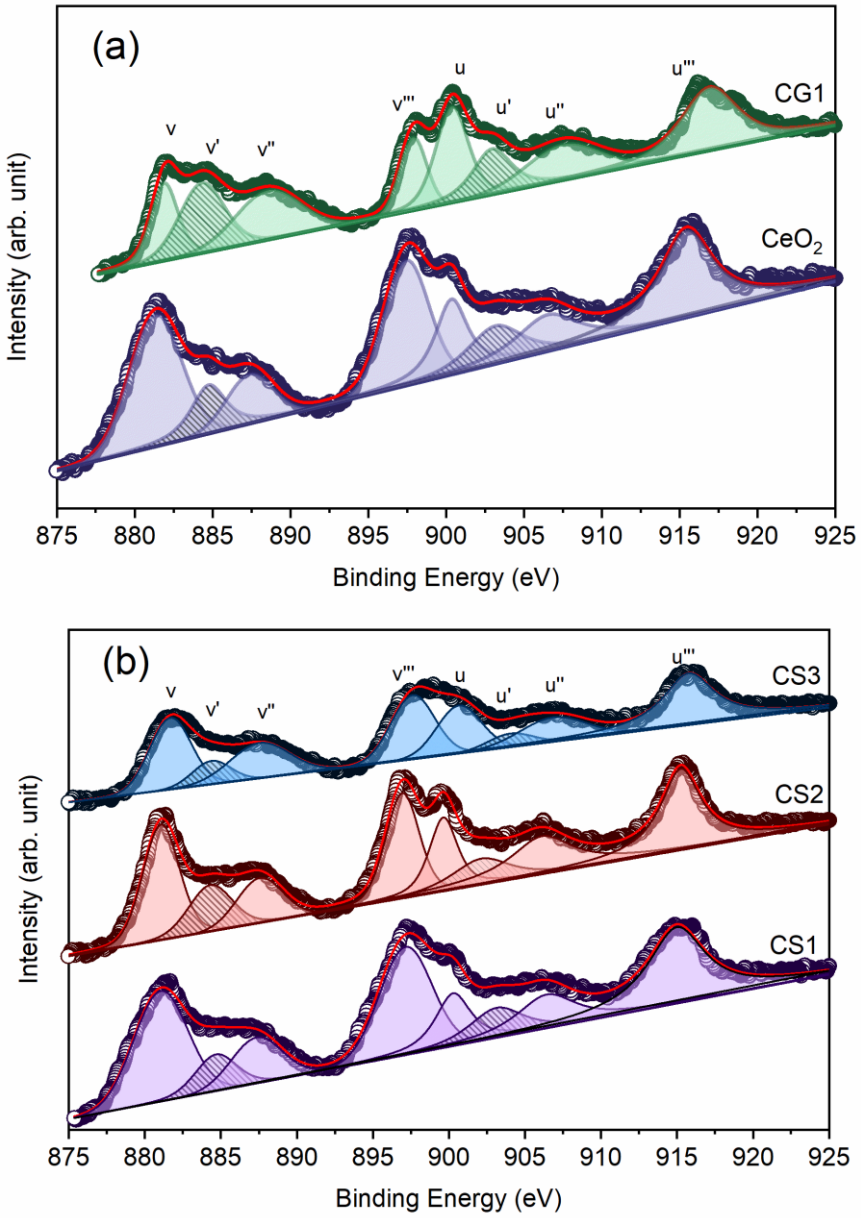

Fig 4.13 XPS spectrum of Ce3d for (a) CeO_2 and $Ce_{0.9}Gd_{0.1}O_{1.95}$ and (b) $Ce_{1-y}Sr_yO_{2-\delta}$ (y=0.025, 0.05, and 0.075). The spectrum is deconvoluted and marked for different peaks

Looking at the O1s XPS spectrum (**Fig 4.14 (a)** and **(b)**), the main peak appearing around 529 eV (marked with superscript b in **Table 4.3**) corresponds to the O^{2-} peak of CeO_2 lattice, is marked as O_L [214]. With the Gd doping, this peak appears at the same position, whereas, for Sr, the peak is slightly shifted to the lower binding energy side. The binding energies corresponding to these O1s peaks are mentioned in **Table 4.3.** The peaks marked as O_{ad} are attributed to the surface-adsorbed oxygen [214]. The peak at 530 eV might appear because of the oxygen vacancies (marked as O_v) present in the samples [215]. The broadening of the oxygen peaks implies the incorporation of Sr in the CeO_2 lattice [216]. The peak at 525 and 527 eV is because of the double charge effect, which occurs when charge accumulates on the sample surface [217].

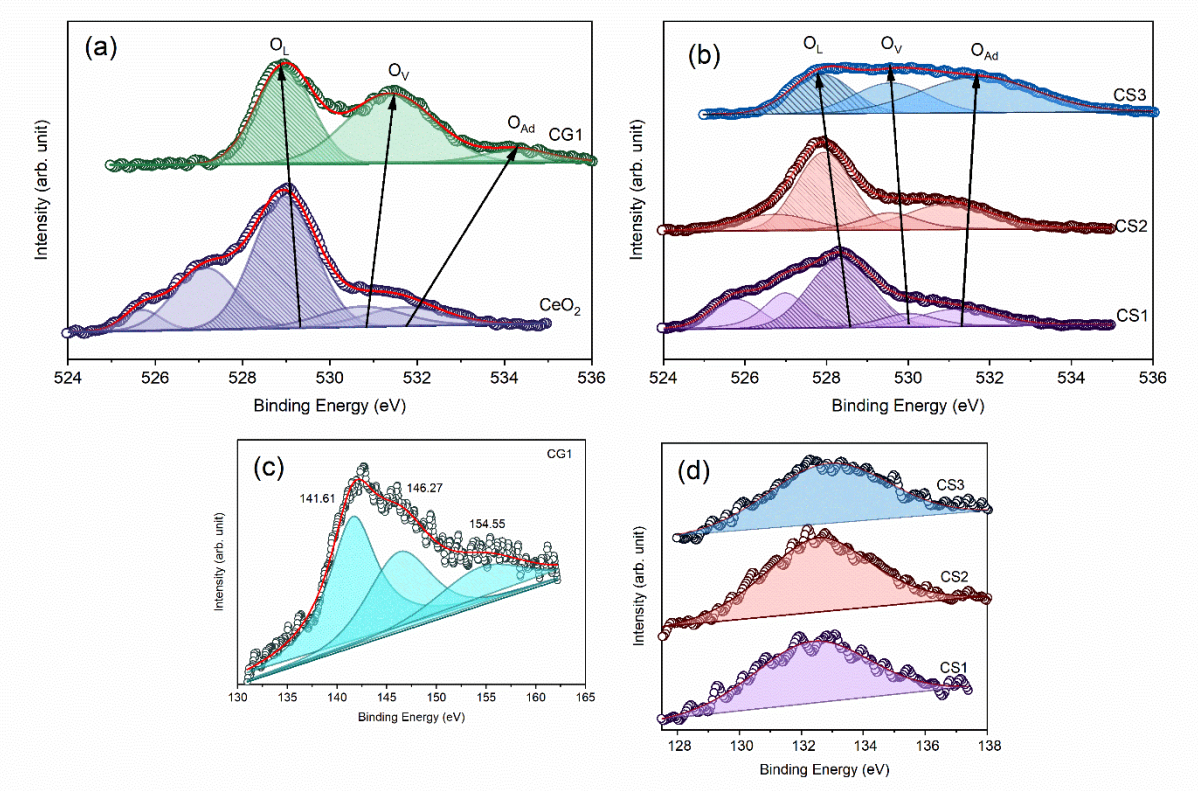

Fig 4.14 XPS spectrum of O1s for (a) CeO_2 and CG1 and (b) CS1, CS2, and CS3, and XPS spectrum of (c) Gd4d for CG1, and (d) Sr3d for CS1, CS2, and CS3. The spectrum is deconvoluted and marked for different peaks

The XPS spectrum of Gd4d shows three peaks at 141.61, 146.27, and 154.55 eV (**Fig 4.14 (c)**). The first two peaks correspond to $Gd4d_{5/2}$ and $Gd4d_{3/2}$, respectively [213, 218]. The peak at 154.55 eV is associated with the charge transfer process [158]. Since the fraction of Sr is very small in the samples, only one peak is observed corresponding to the Sr3d spectra in the CS1, CS2, and CS3 samples, as shown in **Fig 4.14 (d)**.

Table 4.3 Binding energies of Ce3d core levels and O1s core levels calculated from XPS spectra of CeO_2, CG1, CS1, CS2, and CS3 samples

Sample name	**Peak Positions (eV)**			**Ce^{3+}/Ce^{4+} (%)**
	$Ce3d_{5/2}$	**$Ce3d_{3/2}$**	**O1s**	
CeO_2	881.33	900.35	525.70	15
	884.75[a]	903.17[a]	527.15	
	887.40	906.53	528.95[b]	
	897.44	915.45	530.72	
			531.71	
CG1	881.90	900.38	528.95[b]	24
	884.32[a]	902.56[a]	531.38	
	885.57	907.53	534.29	
	897.88	916.91		
CS1	881.03	900.27	525.78	13
	884.68[a]	903.14[a]	526.98	
	887.34	906.42	528.34[b]	
	897.15	914.98	530.00	
			531.21	
CS2	881.05	899.63	526.72	16
	884.32[a]	902.12[a]	527.94[b]	
	887.56	906.13	529.54	
	896.94	915.26	530.99	
CS3	881.56	900.05	527.87[b]	11
	884.12[a]	903.12[a]	529.58	
	887.55	906.69	531.70	
	897.29	915.79		

[a] represents peaks belonging to Ce^{3+}, and [b] represents peaks belonging to O_L

From the above XPS analysis, the presence of Ce^{3+} and oxygen vacancies in the samples has been confirmed. Further, from the semiquantitative analysis of Ce3d spectra, and the Raman

spectra, it can be said that Sr dopant reduces the formation of Ce^{3+} ions as the peaks corresponding to this cation disappear in Sr doped ceria samples.

4.7 Conductivity analysis

AC impedance spectroscopy is used to study the effect of doping on the ionic conductivity of the pellets in a symmetric cell configuration. Impedance spectra of the samples sintered at 1450 °C exhibit three semicircles, as shown in **Fig 4.15**. The first semicircle corresponding to the grain resistivity (ρ_g) is observed in the higher frequency region, and the second semicircle corresponding to the grain boundary resistivity (ρ_{gb}) in the medium frequency region. The third arc belonging to the electrolyte-electrode resistivity (ρ_e) is observed in the lower frequency region. All these contributions are not observed in all the samples, as can be seen in **Fig 4.15 (a)**, as they depend on the resistivity behaviour of the sample [134]. The diameter of the semi-circular arcs on the x-axis is used to compute the resistivities of the grains and grain boundaries. For CeO_2 and $Ce_{0.9}Gd_{0.1}O_{1.95}$, only the grain boundary arc is visible. In the case of $Ce_{0.8}Gd_{0.2}O_{1.90}$ and $Ce_{0.7}Gd_{0.3}O_{1.85}$, both grain and grain boundary arcs are discernible, followed by the electrolyte-electrode interface. The SEM of these samples also supports these observations. The grains are deformed in $Ce_{0.8}Gd_{0.2}O_{1.90}$ and $Ce_{0.7}Gd_{0.3}O_{1.85}$ samples. All three arcs are visible for Sr-doped ceria, as seen in **Fig 4.15 (b)**. In the case of Sr and Gd singly doped ceria, the grain boundary resistivity is more pronounced than grain resistivity. However, in the case of Gd and Sr co-doped ceria, the arc corresponding to the grain is more pronounced than the grain boundary, as seen in **Fig 4.15 (c)** and **(d)**. It implies that the partial liquid phase sintering phenomenon occurs only on the sample's surface. However, it is higher in some samples like CG1S3 and CG2S3, as observed in **Fig 4.8**. As the temperature increases, the arcs representing the grain and grain boundary disappear, and the low-frequency arc becomes more pronounced. The grain boundary resistivity also disappears with the increasing Sr concentration. One reason behind this might be that with increasing Sr concentration, the grain

size increases along with the reduction of grain boundaries.

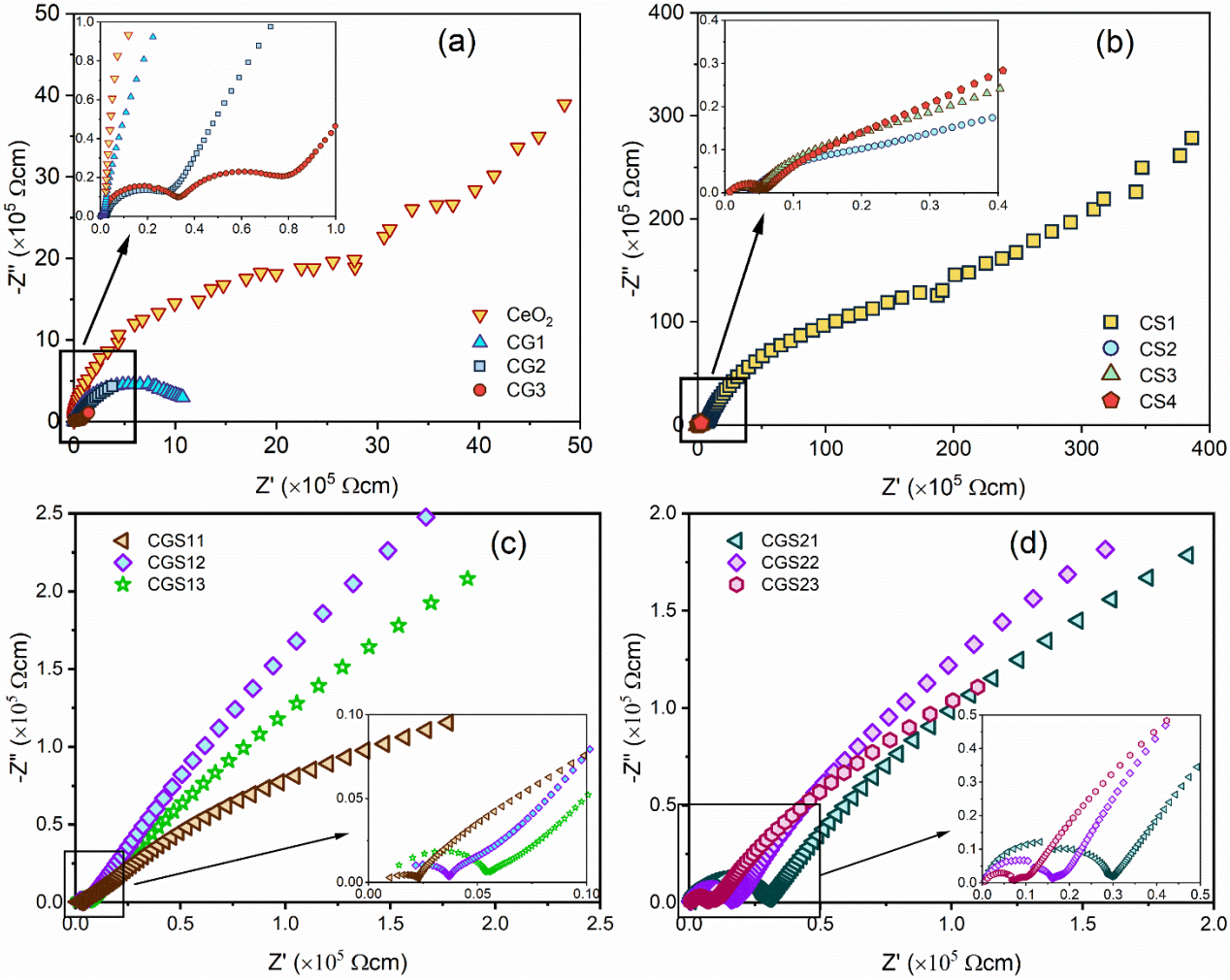

Fig 4.15 Nyquist plots for (a) CeO_2 and $Ce_{1-x}Gd_xO_{2-\delta}$ (x=0.1, 0.2 and 0.3) (b) $Ce_{1-y}Sr_yO_{2-\delta}$ (y=0.025, 0.05 and 0.075, and 0.10), (c) $Ce_{0.9-y}Gd_{0.1}Sr_yO_{2-\delta}$, and (d) $Ce_{0.8-y}Gd_{0.2}Sr_yO_{2-\delta}$ (y=0.025, 0.05 and 0.075) recorded at 400 °C

The impedance spectra were fitted to the conventional equivalent electronic circuit containing three Resistance-Constant Phase Element (R-CPE) subcircuits in series, as given in **Fig 4.16**.

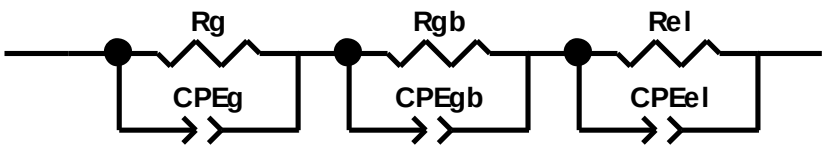

Fig 4.16 R-CPE combinations used to fit the Nyquist plots

Here, R_g, R_{gb}, and R_{el} are the grain, grain boundary, and electrode resistance, respectively. CPE_g, CPE_{gb}, and CPE_{el} are the constant phase elements of grain, grain boundary, and electrode, respectively. The conductivity and activation energy are calculated using the equations (3.9) and (3.10) discussed in **Chapter 3**, **section 3.4.7.**

As the temperature increases, the conductivity increases for all the samples, as seen in **Fig 4.17** and **Fig 4.18**. Conductivity increases with temperature as oxygen vacancy hopping is a thermally activated process in ceramic samples [46]. CeO_2 shows minimum conductivity. However, oxygen vacancies are formed due to the conversion of Ce^{4+} to Ce^{3+} in undoped ceria samples. The oxygen vacancies in CeO_2 may be localized and less than in other samples. Also, this sample has the lowest density, showing minimum conductivity in all the samples.

$Ce_{0.9}Gd_{0.1}O_{1.95}$ has a maximum conductivity of 1.67×10^{-2} Scm^{-1} at 600 °C, higher than reported in the literature for a similar composition [89, 95, 99]. Adding Gd^{3+} increased the ionic conductivity of $Ce_{0.9}Gd_{0.1}O_{1.95}$ by increasing vacancies in the host crystal structure. However, with the further addition of Gd^{3+}, the conductivity decreases marginally. This can be explained on the basis of trapping of oxygen vacancies in a cluster [122]. The trapped oxygen vacancies become immobile, and the conductivity decreases. Secondly, Mori and Drennan [203] reported the presence of some small regions (domains) with oxygen vacancy ordering in $Ce_{0.8}Gd_{0.2}O_{1.90}$. These domains are supposed to be formed due to the segregation of dopant cations and oxygen vacancies [209]. The size of these domains increases with the increase in the dopant concentration, leading to an increase in the concentration of oxygen vacancies in these regions. Ye *et al.* [209] related these domain regions to the presence of the C-type structure of Gd_2O_3 in the $Ce_{0.8}Gd_{0.2}O_{1.90}$ based on extensive transmission electron microscopy (TEM) analysis. This has also been confirmed by the presence of peaks related to C-type structure in the Raman spectra of present samples. This ordering of oxygen vacancies due to the presence of microdomains in $Ce_{0.8}Gd_{0.2}O_{1.90}$ and the secondary phase in $Ce_{0.7}Gd_{0.3}O_{1.85}$ will reduce the

conductivity of the samples [191]. In the Arrhenius plot, in **Fig 4.17 (a)**, all the samples have a single slope, indicating that the current samples have a single conduction mechanism. Secondly, the activation energy of most of the samples is more than 1 eV (see **Table 4.4**) which could be related to the ionic conduction in the present systems [159, 219]. The analysis of the impedance spectra of all samples reveals that the minimum activation energy is 0.81 eV, which is observed for CG1. This activation energy matches with earlier reported values for doped CeO_2 [99, 138, 220, 221].

Table 4.4 Total conductivity (σ_t) and activation energy (E_a) of the $Ce_{1-x}Gd_xO_{2-\delta}$, (x=0, 0.1, 0.2, and 0.3)

Composition	**σ_t (Scm^{-1})**		**E_a (eV)**
	500 °C	**600 °C**	
CeO_2	3.8×10^{-6}	1.93×10^{-5}	1.10
$Ce_{0.9}Gd_{0.1}O_{1.95}$ (CG1)	5.15×10^{-3}	1.67×10^{-2}	0.81
$Ce_{0.8}Gd_{0.2}O_{1.90}$ (CG2)	5.24×10^{-4}	3.33×10^{-3}	1.22
$Ce_{0.7}Gd_{0.3}O_{1.85}$ (CG3)	2.94×10^{-4}	2.55×10^{-3}	1.39

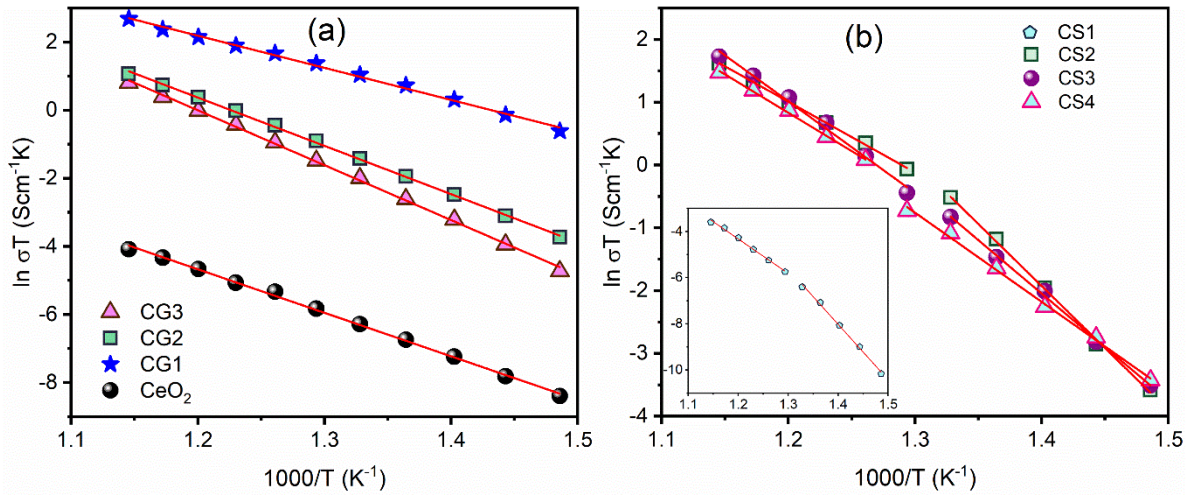

Fig 4.17 Arrhenius plots of total conductivity to find out the activation energy of (a) CeO_2 and $Ce_{1-x}Gd_xO_{2-\delta}$ (x=0.1, 0.2, and 0.3) and (b) $Ce_{1-y}Sr_yO_{2-\delta}$ (y=0.025, 0.050, 0.075, and 0.1). Inset is the plot for $Ce_{0.975}Sr_{0.025}O_{1.975}$ (CS1)

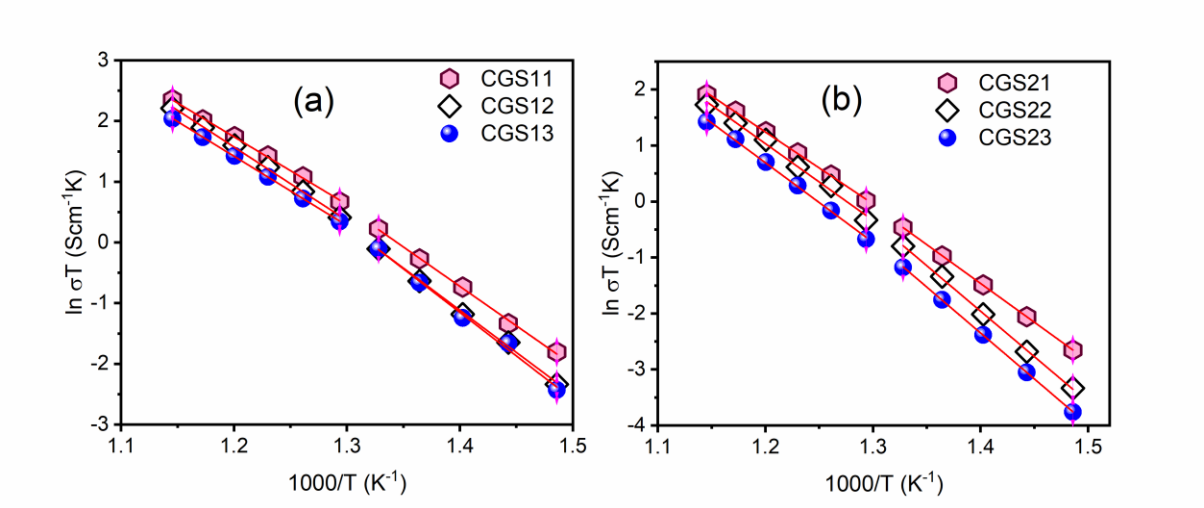

Fig 4.18 Arrhenius plots of total conductivity to find out the activation energy of (a) $Ce_{0.9-y}Gd_{0.1}Sr_yO_{2-\delta}$ and (b) $Ce_{0.8-y}Gd_{0.2}Sr_yO_{2-\delta}$ (y=0.025, 0.050, and 0.075)

The total conductivity of the CS series is plotted against temperature in **Fig 4.17 (b),** and the CGS series is plotted in **Fig 4.18**. A change in slope is observed around 500 °C in both series. This change is not observed for the CG series. This might be due to differences in the ionic radii of Gd and Sr cations. The larger ionic size of the Sr may increase the energy barrier for the hopping of oxide ions [222]. Further, Sr is known to form defect clusters with oxygen ions [223]. Now, these defect clusters are also there in CG samples, as seen with a very small change in slope (~0.05 eV) observable in **Fig 4.17 (a)**. The ionic conductivity in doped ceria electrolytes results from the transportation of oxygen ions. At low temperatures, the defect clusters ($M_{Ce}^{"} - V_o^{\bullet\bullet}$ and $M_{Ce}^{"} - V_o^{\bullet\bullet} - M_{Ce}^{"}$) are formed in ceria having association enthalpy ΔH_a [76]. So, the defect clusters might be formed with Sr^{2+} or Gd^{3+} in present doped ceria samples. These defect clusters dissociate as the temperature increases. Assuming that the maximum number of defect clusters are dissociated at the inflection point, as shown in **Fig 4.17 (b)** and **Fig 4.18**, the activation energy at higher temperatures (>500 °C) might be the enthalpy of migration of oxygen vacancies (ΔH_m). The activation energy below this temperature (<500 °C) will be the sum of migration enthalpy and association enthalpy $E_a = \Delta H_m + \Delta H_a$. The

dissociation of these defects clusters might result in a low energy path for oxygen ions migration near these clusters [224]. Because of this, the conductivity significantly changes at temperatures exceeding 500 °C. The values of the activation energy are mentioned in **Table 4.5**.

Table 4.5 Total conductivity (σ_t) and activation energy (Ea) of the different samples for temperatures higher than and less than 500 °C

Composition (Name)	**σ_t (Scm^{-1})**		**E_a (eV)**		**ΔH_a**
	500 °C	**600 °C**	**T<500 °C**	**T>500 °C**	**(eV)**
$Ce_{0.975}Sr_{0.025}O_{1.975}$ (CS1)	4.15×10^{-6}	3.16×10^{-5}	2.07	1.29	0.78
$Ce_{0.95}Sr_{0.05}O_{1.95}$ (CS2)	1.21×10^{-3}	5.77×10^{-3}	1.70	0.97	0.73
$Ce_{0.925}Sr_{0.075}O_{1.925}$ (CS3)	8.32×10^{-4}	6.46×10^{-3}	1.46	1.26	0.20
$Ce_{0.9}Sr_{0.1}O_{1.90}$ (CS4)	6.25×10^{-4}	5.00×10^{-3}	1.22	1.05	0.17
$Ce_{0.875}Gd_{0.1}Sr_{0.025}O_{1.925}$ (CG1S1)	3.26×10^{-3}	1.20×10^{-2}	1.12	0.96	0.16
$Ce_{0.85}Gd_{0.1}Sr_{0.05}O_{1.90}$(CG1S2)	1.95×10^{-3}	1.04×10^{-2}	1.20	1.04	0.16
$Ce_{0.825}Gd_{0.1}Sr_{0.075}O_{1.875}$ (CG1S3)	1.83×10^{-3}	8.79×10^{-3}	1.24	0.99	0.25
$Ce_{0.775}Gd_{0.2}Sr_{0.025}O_{1.875}$ (CG2S1)	1.31×10^{-3}	7.76×10^{-3}	1.19	1.11	0.08
$Ce_{0.75}Gd_{0.2}Sr_{0.05}O_{1.85}$ (CG2S2)	9.28×10^{-4}	6.46×10^{-3}	1.40	1.18	0.22
$Ce_{0.725}Gd_{0.2}Sr_{0.075}O_{1.825}$ (CG2S3)	6.62×10^{-4}	4.76×10^{-3}	1.41	1.23	0.18

As seen in **Table 4.5**, the highest conductivity is observed for the CS3 sample in the CS series at 600 °C. A comparison of the conductivities with a dopant concentration of the different samples measured at 600 °C is given in **Fig 4.19**. The conductivity increases gradually with increasing Sr concentration but then decreases for the CS4 sample. This decrease is associated with the formation of a secondary phase in the CS4 sample, as observed in the XRD data. In the CGS series, the highest conductivity is observed for the CG1S1 sample at 600 °C, i.e., 1.20×10^{-2} Scm^{-1} followed by CG1S2 (1.04×10^{-2} Scm^{-1}). However, the conductivity is slightly less than for CG1 (1.67×10^{-2} Scm^{-1}). However, this value is still higher than the minimum conductivity (.01 Scm^{-1}) required for ion conduction at fuel cell temperature [225]. The conductivity decreases with increasing dopant (Gd and Sr) concentration. This happens because of two reasons. First, the increasing Sr concentration shows more liquid phase

sintering, as observed in the FESEM micrographs, thus forming an amorphous layer along the grain boundaries [119, 121, 226]. This layer inhibits the movement of ions through the sample. Secondly, in the case of $Ce_{0.2-y}Gd_{0.2}Sr_yO_{2-\delta}$, the formation of defect associates of Gd_2O_3 occurs, as confirmed by the presence of the band at 370 cm^{-1} in Raman spectra. This also inhibits ion conduction as ions are trapped within these defect associates. Therefore, lesser conductivity is observed with these samples.

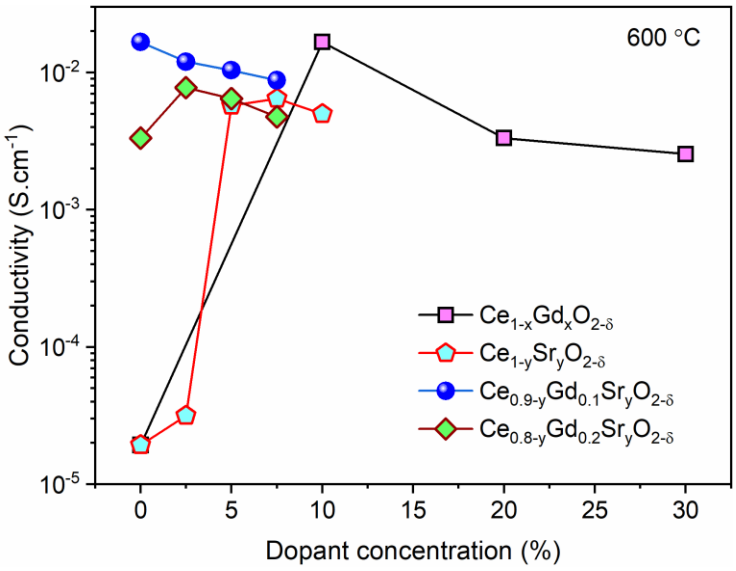

Fig 4.19 Conductivity vs dopant concentration of $Ce_{1-x}Gd_xO_{2-\delta}$ (x=0, 0.1, 0.2, and 0.3), $Ce_{1-y}Sr_yO_{2-\delta}$ (y=0, 0.025, 0.050, 0.075, and 0.1), $Ce_{0.9-y}Gd_{0.1}Sr_yO_{2-\delta}$ and $Ce_{0.8-y}Gd_{0.2}Sr_yO_{2-\delta}$ (y=0, 0.025, 0.050, and 0.075) measured at 600 °C

Based on the above conductivity analysis, it can be concluded that the highest conductivity is observed for the CG1 sample, followed by CG1S1 and CG1S2 samples. These three samples, along with the CS3 sample (form CS series), are selected for power studies in real SOFC conditions. A comparison of these electrolyte material with others in the literature is given in **Table 4.6**. The conductivity observed is comparable to those in the literature and even better than some other electrolytes.

Table 4.6 A comparison of the current electrolytes with those in the literature

Electrolyte	**Density (%)**	**Conductivity (S.cm^{-1})**	**Activation energy (eV)**	**Ref.**
$Ce_{0.9}Gd_{0.1}O_{1.95}$	~95	1.67×10^{-2} @ 600 °C	0.81	This work
$Ce_{0.925}Sr_{0.075}O_{2-\delta}$	~97	6.46×10^{-3} @ 600 °C	1.26	This work
$Ce_{0.875}Gd_{0.1}Sr_{0.025}O_{1.925}$	~96	1.20×10^{-2} @ 600 °C	0.96	This work
$Ce_{0.85}Gd_{0.1}Sr_{0.05}O_{1.90}$	~96	1.04×10^{-2} @ 600 °C	1.04	This work
$Ce_{0.8}Nd_{0.2}O_{1.9}$	~94	0.15×10^{-2} @ 600 °C	0.87	[117]
$Ce_{0.8}Sm_{0.2}O_{2-\delta}$	~96	1.01×10^{-2} @ 700 °C	0.89	[120]
$Ce_{0.9}Gd_{0.1}O_{2-\delta}$	-	1.13×10^{-2} @ 700 °C	1.02	[227]
$Ce_{0.9}Pr_{0.1}O_{2-\delta}$	-	1.21×10^{-3} @ 700 °C	1.28	[73]
$Ce_{0.83}Sm_{0.085}Pr_{0.085}O_{2-\delta}$	~95	2.63×10^{-2} @ 600 °C	0.68	[134]
$Ce_{0.80}Nd_{0.18}Y_{0.02}O_{1.90}$	~92	1.28×10^{-2} @ 600 °C	1.03	[142]
$Ce_{0.85}La_{0.10}Sr_{0.05}O_{2-\delta}$	~95	2.72×10^{-3} @ 600 °C	0.96	[80]
$Ce_{0.85}Gd_{0.10}Sr_{0.05}O_{2-\delta}$	~96	6.78×10^{-3} @ 600 °C	0.96	[80]
$Ce_{0.85}Dy_{0.1}Ca_{0.02}Bi_{0.03}O_{1.915}$	~95	3.53×10^{-2} @ 700 °C	0.79	[137]

4.8 Summary

Three series of samples (CG, CS, and CGS series) are synthesized using an ultrasound-assisted sol-gel auto-combustion method to refine the particles for better density, sinterability, and conductivity. The solid solubility limits observed for Gd-doped CeO_2, Sr-doped CeO_2, and Gd-Sr co-doped CeO_2 are ~20 %, ~7.5 %, and ~5 %, respectively. Gd-Sr co-doped samples exhibited the partial liquid phase sintering of the samples. The doped and co-doped samples show a relative density of more than 90 %. The highest conductivity is observed for 10 % Gd doped CeO_2 (1.67×10^{-2} Scm^{-1}), followed by 10 % Gd-2.5 % Sr doped ceria and then 10 % Gd and 5.0 % Sr doped ceria. The minimum activation energy is observed for the CG1 sample, i.e., 0.81 eV. The highest activation energy is observed for the CG3 sample, i.e., 1.39 eV. The present samples are predominantly ionic conductors.

Chapter 5

SOFC Complete Cell Fabrication and Testing

5.1Selection of electrolyte, anode, and cathode for cell testing

Four different samples synthesised in our laboratory have been chosen as electrolytes for cell testing with anode and cathode in real SOFC conditions. These four electrolytes are CG1, CS3, CG1S1, and CG1S2 samples, and the cells prepared using these electrolytes are named cell I, cell II, cell III, and cell IV, respectively. The electrolyte selection is based on their conductivity and other structural parameters, as discussed in **Chapter 4**. A composite of NiO and $Ce_{0.9}Gd_{0.1}O_{1.95}$ and $(La_{0.6}Sr_{0.4})_{0.95}Co_{0.8}Fe_{0.2}O_{3-\delta}$ (LSCF) and $Ce_{0.9}Gd_{0.1}O_{1.95}$ in the ratio of 65 and 35 wt. % is chosen for anode and cathode, respectively. These materials are chosen because they are compatible with ceria-based electrolytes and also depict good performance [182]. Moreover, CG1 present in the anode and cathode increases the number of triple phase boundaries and, thus, enhances the cell performance [40]. The button cells are tested in humidified hydrogen (3 % H_2O) and ambient air in the temperature range 500-600 °C. The fractured surface of the cell is also analysed using FESEM to find any traces of diffusion after the cell processing. The summarised parameters of the selected electrolytes are given in **Table 5.1**.

Table 5.1 Composition (name), relative density, lattice parameter, grain size, conductivity, and activation energy of the optimized electrolytes

Composition (name)	**Relative Density (%)**	**Lattice parameter (Å)**	**Grain size (µm)**	**Conductivity (Scm^{-1}) at 600 °C**	**Activation energy (eV)**
$Ce_{0.9}Gd_{0.1}O_{1.95}$ (CG1)	~95	5.417	1.34	1.67×10^{-2}	0.81
$Ce_{0.925}Sr_{0.075}O_{1.925}$ (CS3)	~97	5.437	1.61	6.46×10^{-3}	1.26

$Ce_{0.875}Gd_{0.1}Sr_{0.025}O_{1.925}$ (CG1S1)	~96	5.424	3.84	1.20×10^{-2}	0.96
$Ce_{0.85}Gd_{0.1}Sr_{0.5}O_{1.90}$ (CG1S2)	~96	5.431	5.65	1.04×10^{-2}	1.04

5.2 Phase analysis of anode and cathode

The phase analysis of the anode and cathode powders has been studied using X-ray diffraction, and the XRD patterns are shown in **Fig 5.1 (a)** and **(b)**, respectively. No secondary phase peaks appear in the XRD pattern, which confirms no reaction occurs during anode and cathode processing. In **Fig 5.1 (a)**, the peaks correspond to the NiO show cubic phase with space group $Fm\bar{3}m$ (ICDD card no. - 01-089-5881), and in **Fig 5.1 (b),** the peaks correspond to the cubic structure of LSCF with space group $Pm\bar{3}m$ (ICDD card no.- 01-089-5720). Along with these phases, peaks corresponding to the cubic fluorite structure of $Ce_{0.9}Gd_{0.1}O_{2-\delta}$ (ICDD card no. – 01-075-0161) also appear.

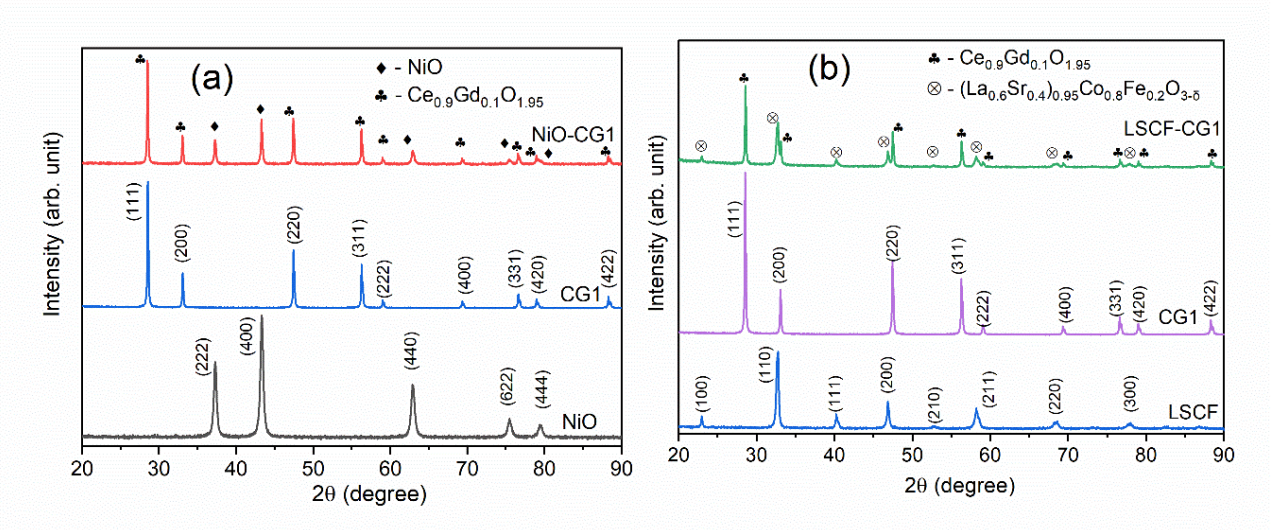

Fig 5.1 XRD pattern of (a) anode (NiO-$Ce_{0.9}Gd_{0.1}O_{2-\delta}$) and (b) cathode ($(La_{0.6}Sr_{0.4})_{0.95}Co_{0.8}Fe_{0.2}O_{3-\delta}$- $Ce_{0.9}Gd_{0.1}O_{2-\delta}$)

5.3 Optimization of tape for anode

The anode is fabricated using an aqueous tape-casting method to make an anode-supported fuel cell. Several tapes with different compositions are tried as per the parameters given in **Table 5.2**. In the first step, the anode powder is milled with deionised (DI) water and dispersant for about 16 h. Then, two plasticizers are added to this slurry and mixed further for about 2 h. After mixing these two, the PVA solution is added to the slurry along with the defoamer, and then it is mixed further for 1 h. After ensuring the complete mixing of all the ingredients, the slurry has been cast on a Mylar film using a doctor's blade, ensuring a thickness of about 600 μm for the dried tape. The final tape has been sintered at 1450 °C for 4h following a heating rate of 1 °C/min up to 500 °C, 2 °C/min up to 1000 °C and 3 °C/min till 1450 °C.

Table 5.2 Slurry composition for aqueous-based anode tape casting

	A1 (wt. %)	**A2 (wt. %)**	**A3 (wt. %)**	**A4 (wt. %)**	**A5 (wt. %)**	**A6 (wt. %)**	**A7 (wt. %)**	**A8 (wt. %)**	**A9 (wt. %)**
Powder (NiO-CG1)	**32**	**40**	**45**	**50**	**45**	**50**	50	50	50
Solvent (DI water)	16	16	16	16	**11**	**10**	**6**	**6.7**	**6**
Dispersant (DARVAN CN)	2	2	2	2	2	2	2	2	2
Binder (PVA solution-15 %)	**41**	**34**	**29**	**24**	**34**	**30**	**34**	**34**	**34**
Plasticizer-I (PEG)	3.9	3.9	3.9	3.9	3.9	3.9	3.9	3.9	3.9
Plasticizer-II (Glycerol)	3.9	3.9	3.9	3.9	3.9	3.9	3.9	3.9	3.9
Defoamer (octanol)	0.7	0.7	0.7	0.7	0.7	0.7	0.7	-	**1 drop[a]**

a-measured using 5 ml syringe.

According to the literature, the first trial of the anode is tried using the composition A1. However, the slurry shows low viscosity and could not be cast properly. So, after a few failed

attempts, three different compositions have been tried by increasing the amount of load and varying the amount of binder solution. In this case, the tapes have been formed but due to low viscosity they show the formation of rivulets, as can be seen from **Fig 5.2 (a)-(c)**. The probable reason may be the high amount of solvent in the tapes. So, the next few formulations are tried with two different loads and varying the quantity of PVA and DI water (A5 and A6). The formed tapes are better than the previous ones, as seen in **Fig 5.2 (d)** and **(e)**. Further, the tapes are sintered at 1450 °C for 4 h. The sintered tape show fine with no porosity but possess poor strength due to less thickness. As the cells are supposed to be anode-supported, further trials are carried out to get thicker tapes.

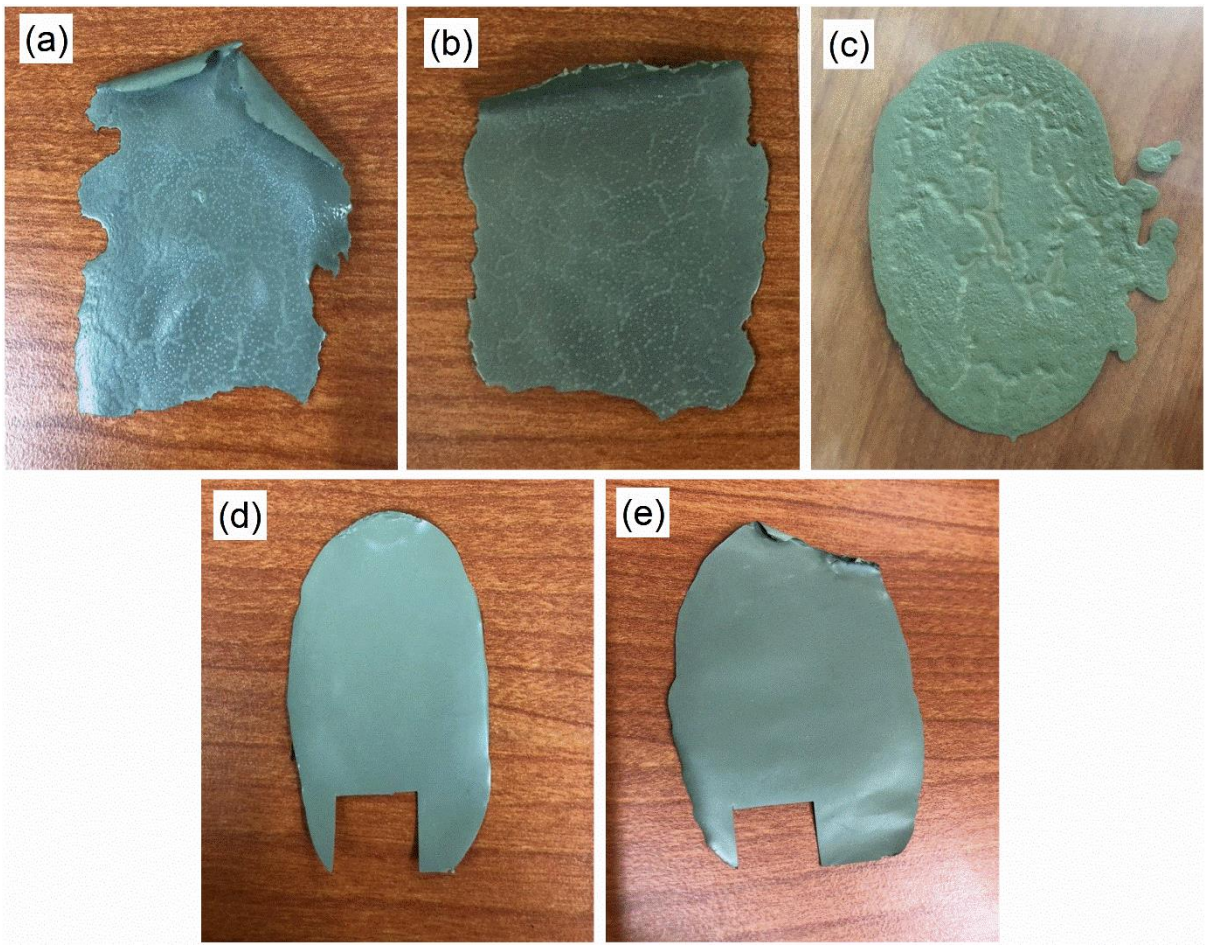

Fig 5.2 Tapes formed using slurries (a) A2, (b) A3, and (c) A4 show small rivulet-like structures. Tapes formed using slurries (d) A5 and (e) A6 show clean tapes with almost no defects

Hence, A7 composition has been tried with 50 wt. % of load and reducing the amount of DI water to just about 6.7 wt. % and PVA solution to 34 wt. %. The tape formed is much better and thicker than the earlier ones. The only issue remains with octanol separation on the top surface (**Fig 5.3 (a)**). Therefore, the A8 composition has been tried without defoamer, resulting in bubble formation on top of the tape (**Fig 5.3 (b)**). Several attempts have been made to adjust the amount of octanol. Finally, the A9 formulation shows the best results with the optimum thickness and minimum to zero bubble formation, as shown in **Fig 5.3 (c)**. The smaller bubbles in the tape are removed using ultrasonification for 5 minutes.

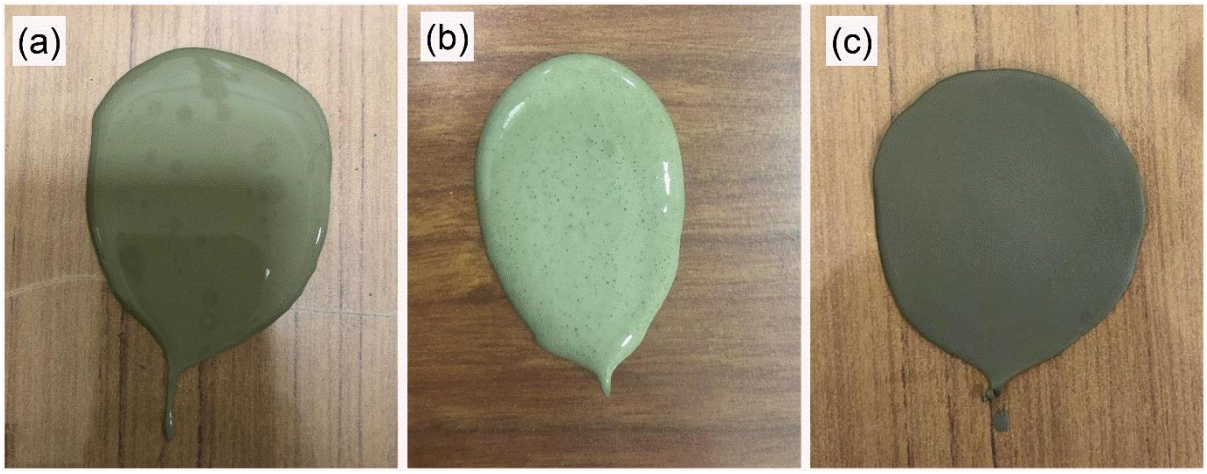

Fig 5.3 Tape formed using slurries (a) A7 shows octanol separation, (b)A8 shows bubble formation, and (c) A9 shows almost no defects and optimum thickness

The green tapes cast using slurry A8 are sintered at 1450 °C for 4h. The sintered tapes do not show any sign of crack or bend and show uniform porosity throughout the tape. The burning of the organic components in the tape generates this uniform porosity distribution. The microstructural images in **Fig 5.4 (a)** and **(b)** show the top and fractured surfaces with sufficient porosity, and **Fig 5.4 (c)** shows the thickness of the tape, which is ~ 270 μm.

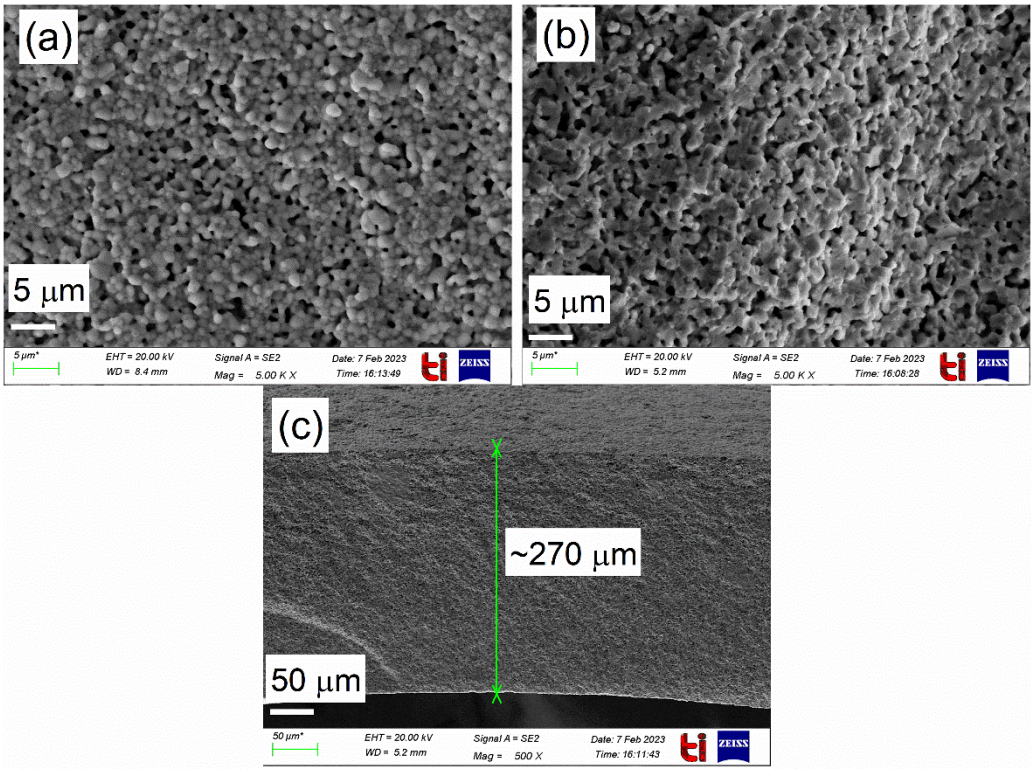

Fig 5.4 FESEM image of the (a) top surface, (b) fractured surface of the sintered tape shows the porous network in the tape, and (c) represents the thickness of the tape

5.4 Electrolyte optimization for spray coating

The electrolyte in the liquid form is spray-coated on the anode green tape using an air gun connected to an air pump that works at high pressure. First, the electrolyte powder (CG1 in this case) is mixed with DI water and dispersant for 12h in a beaker using zirconia balls. Further, PEG was added along with PVA in the slurry and mixed for about 3-4 h. The prepared slurry is sprayed on the green tapes of the anode, i.e., 22 cm in diameter. These green half cells, with both anode and electrolyte, are sintered at 1450 °C for 4h with the same sintering cycle as anode.

The different electrolyte inks tried for this purpose are given in **Table 5.3** (named E1, E2, etc.), and corresponding SEM images of the films are represented in **Fig 5.5** and **Fig 5.6**. The first trial with E1 shows highly dense but non-uniform film after sintering, as seen in **Fig 5.5** (a & b). To improve the uniformity, the load has been slightly decreased (E2 and E3) with increased

DI water. The high-loading content (load > 50 wt. %) inks do not come out of the spray nozzle and are challenging to work with. Thus, it results in the formation of islands on the anode surface. The visual appearance of the film is uniform, but islands can be seen as shown in **Fig 5.5 (a)** and **(b)** under FESEM observation. The density of the films formed with E2 and E3 is reduced, and the non-uniformity of the films is a big challenge (see **Fig 5.5 (c), (d), (e),** and **(f)**). The non-uniformity of the electrolyte film might short-circuit the anode and cathode. Another problem with these coatings is that sometimes these will peel off from the surface of the anode.

Table 5.3 Slurry composition tried for the fabrication of electrolyte using spray-coating

Ingredients	**E1 (wt. %)**	**E2 (wt. %)**	**E3 (wt. %)**	**E4 (wt. %)**	**E5 (wt. %)**	**E6 (wt. %)**
Electrolyte	60	58	55	50	45	40
DI water	20	22	25	25	25	25
Binder	10.2	10.2	10.2	15.2	20.2	25.2
Dispersant	6	6	6	6	6	6
Plasticizer	3.8	3.8	3.8	3.8	3.8	3.8

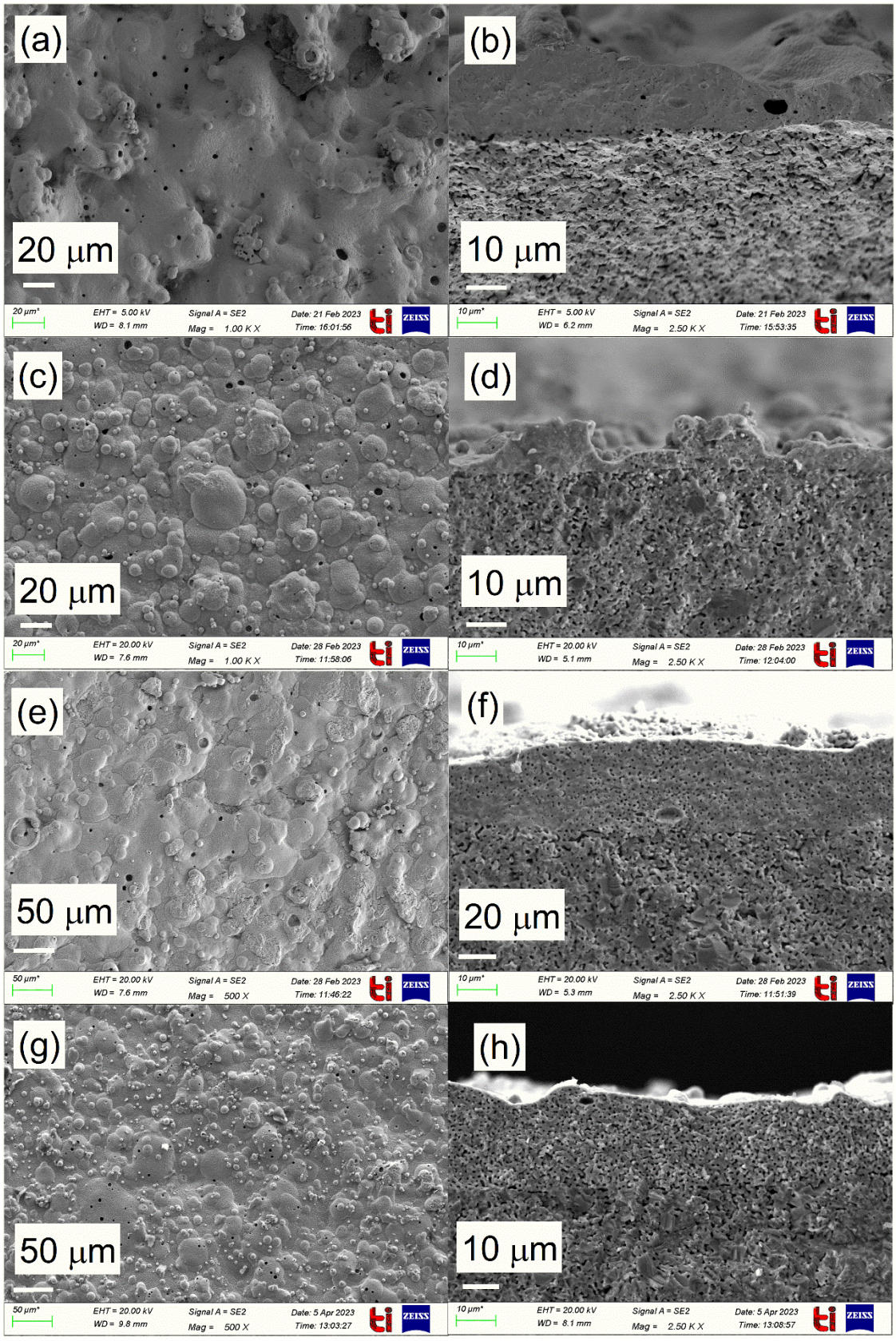

Fig 5.5 FESEM images of the top and fractured surface of the (a & b) E1, (c & d) E2, (e & f) E3, and (g & h) E4, respectively

It is very crucial to have a highly dense electrolyte for better performance. So, the amount of load has been reduced to 50, 45, and 40 wt. %, balanced by increasing the amount of binder as represented by E4, E5, and E6 formulations, respectively. Now, E4 was still a little difficult to work with and showed an island-like structure, as seen in **Fig 5.5 (g)** and **(h)**. However, as shown in **Fig 5.6 (a)** and **(b)**, E5 and E6 formulations are easier to work and depict uniform microstructure. After several trials, it is observed that the only issue that remains is with the density. E5 has been chosen as the final electrolyte formulation as E6 shows cracks after sintering due to low viscosity. The films that are pressed at 10 and 30 $kgcm^{-2}$ showed a uniform layer, but there is an appearance of cracks on the surface (see **Fig 5.6 (c), (d), (e),** and **(f))**. Only the films pressed at 50 $kgcm^{-2}$ depict uniform surfaces with high density and no cracks, as shown in **Fig 5.6 (g)** and **(h)**. A similar process is adopted for other electrolytes, viz. CS3, CG1S1, and CG1S2 electrolytes. All films are fabricated using E5 ink formulation and pressed at 50 $kgcm^{-2}$ before sintering for better density.

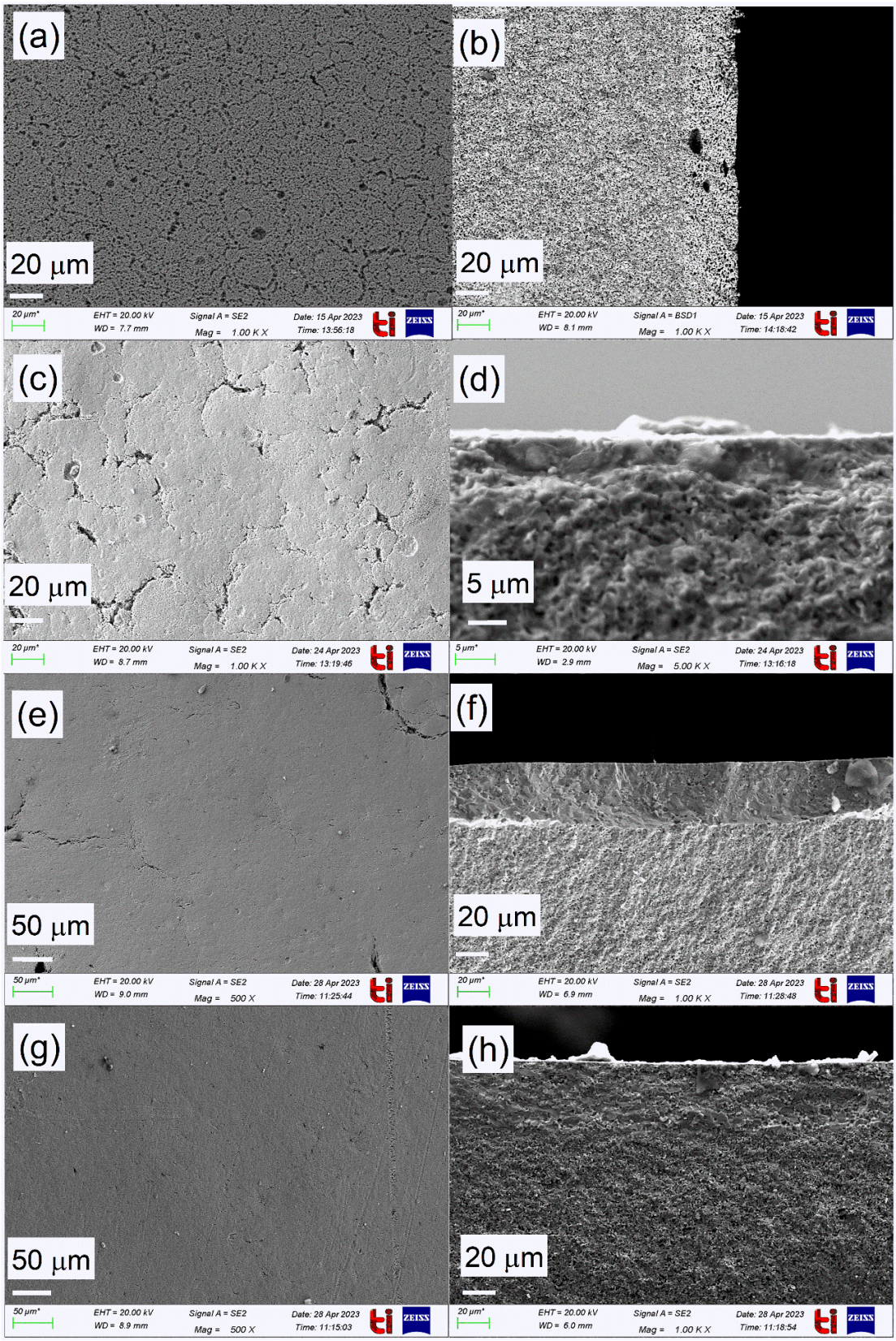

Fig 5.6 FESEM images of top and fractured surface for CG1 using Ink E5 formulation (a & b) not pressed, (c & d) pressed at 10 kgcm^{-2}, (e & f) pressed at 30 kgcm^{-2}, and (g & h) pressed at 50 kgcm^{-2}, respectively

5.5 Cathode painting

After the final sintering of anode and electrolyte at 1450 °C for 4 h, cathode powder ($(La_{0.6}Sr_{0.4})_{0.95}Co_{0.8}Fe_{0.2}O_{3-\delta}$- $Ce_{0.9}Gd_{0.1}O_{2-\delta}$) mixed with terpineol, and ethyl cellulose mixture is painted on top of electrolyte. The complete button cell is sintered at 1000 °C for 2 h. The surface and fractured images of the cathode are given in **Fig 5.7** (a) and (b), respectively. These figures show the clear porosity in the cathode, which is important for airflow throughout.

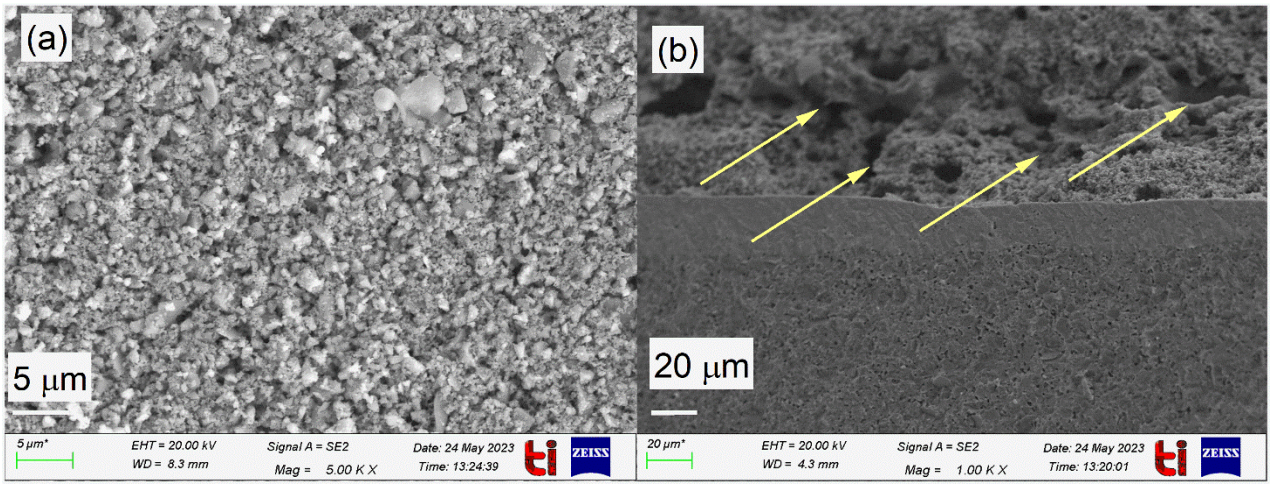

Fig 5.7 (a) Surface and (b) fractured images of the cathode ($(La_{0.6}Sr_{0.4})_{0.95}Co_{0.8}Fe_{0.2}O_{3-\delta}$-$Ce_{0.9}Gd_{0.1}O_{2-\delta}$). The yellow arrows in (b) show the porous structure of the cathode

The FESEM images of complete fractured cells are also taken and shown in **Fig 5.8**. These images show good contact formation between the anode, electrolyte, and cathode, which is crucial to achieve high performance in a fuel cell. The thickness of the anode is between 260-280 µm, whereas the thickness of the electrolyte and cathode lie between 17-18 µm and 80-90 µm, respectively.

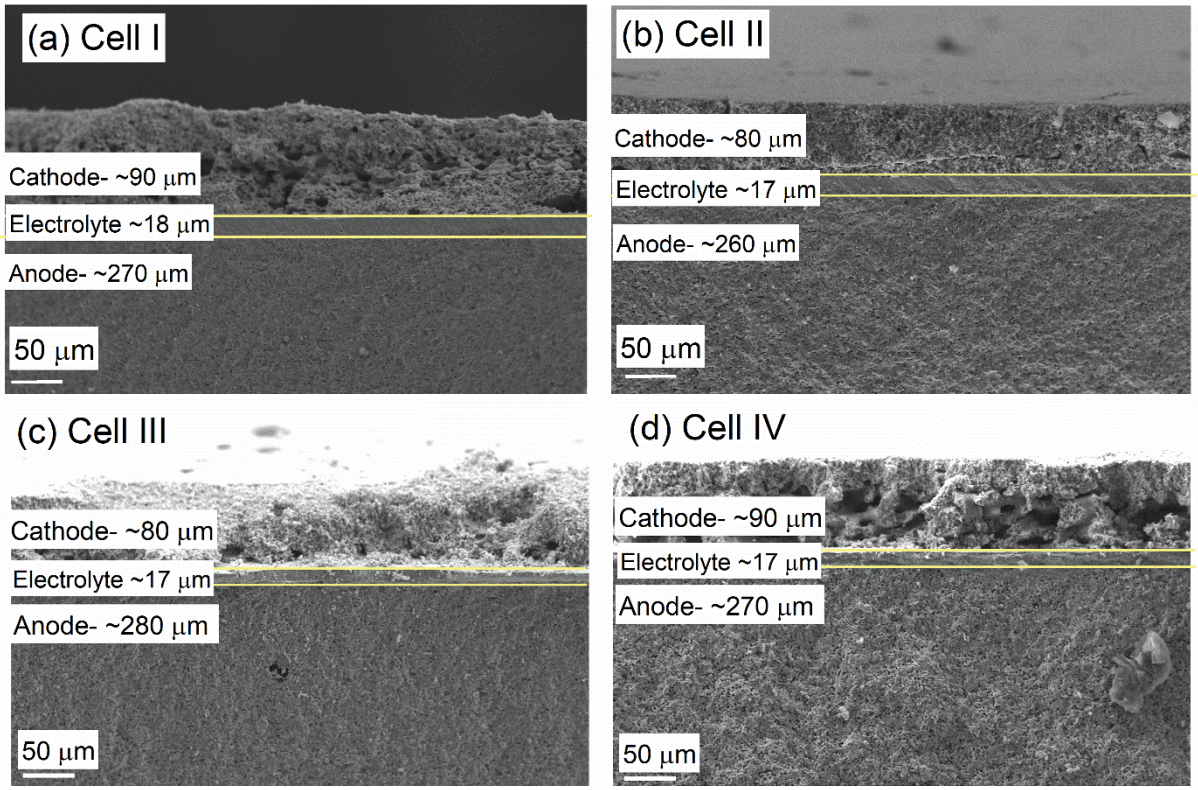

Fig 5.8 FESEM images of fractured surfaces of the (a) cell I, (b) cell II, (c) cell III, and (d) cell IV containing CG1, CS3, CG1S1, and CG1S2 electrolytes, respectively

5.6 Performance of cell

The power studies of the cells I, II, III, and IV measured at 600 °C are presented in **Fig 5.9 (a), (b), (c),** and **(d),** respectively. The measurements of the cells are taken in humidified hydrogen (3 % H_2O) at the anode and air at the cathode side. The open circuit voltage (OCV) and maximum power density of all cells are given in **Table 5.4**. The OCVs are less than theoretically predicted values and decrease with increasing temperature. This might happen for two reasons: first, there might be gas leakage due to sealing issues, and second, electronic conduction through the electrolyte due to the reduction of Ce^{4+} to Ce^{3+} in a reducing environment [228, 229]. The noise in the signal may appear due to the unreacted fuel reacting with the ambient oxygen which causes fluctuations in OCV and the power density [230]. Also, the redox cycling of Ni/NiO might break contacts between metal and the current collector which also causes noise to appear in the signal [230]. The power density increases with the

temperature, and the highest value is observed, ~112.7 $mWcm^{-2}$ at 600 °C for cell III containing **CG1S1** as the electrolyte. This is followed by cell I (with electrolyte-**CG1),** which showed a maximum power density of 102.2 $mWcm^{-2}$. This value of the power density for the CG1 electrolyte is comparable with the reported literature. Wang *et al*. [147] reported a power density of 96 $mWcm^{-2}$ at 800 °C for a cell made using CG1 as electrolyte. Li *et al.* [231] reported a maximum power density to be 113 $mWcm^{-2}$ at 600 °C. Marco *et al.* [232] reported a maximum power density of 80 $mWcm^{-2}$ at 600 °C for a cell with the similar electrolyte. However, power densities as high as 950 $mWcm^{-2}$ at 650 °C are also reported in the literature [233]. Cell II (electrolyte-**CS3**) showed a maximum power density of 88.9 $mWcm^{-2}$ at 600 °C, while cell IV (electrolyte-**CG1S2**) showed only a maximum power density of 42.5 $mWcm^{-2}$. The other cells, i.e., cell II, cell III, and Cell IV are tested for the first time in this work with electrolytes CS3, CG1S1, and CG1S2. It shows that the co-doping of ceria with Gd and Sr improves the performance of the cell. The decrease in the power density for cell IV may be due to the low conductivity and high activation energy, as discussed in **Chapter 4, section 4.7**.

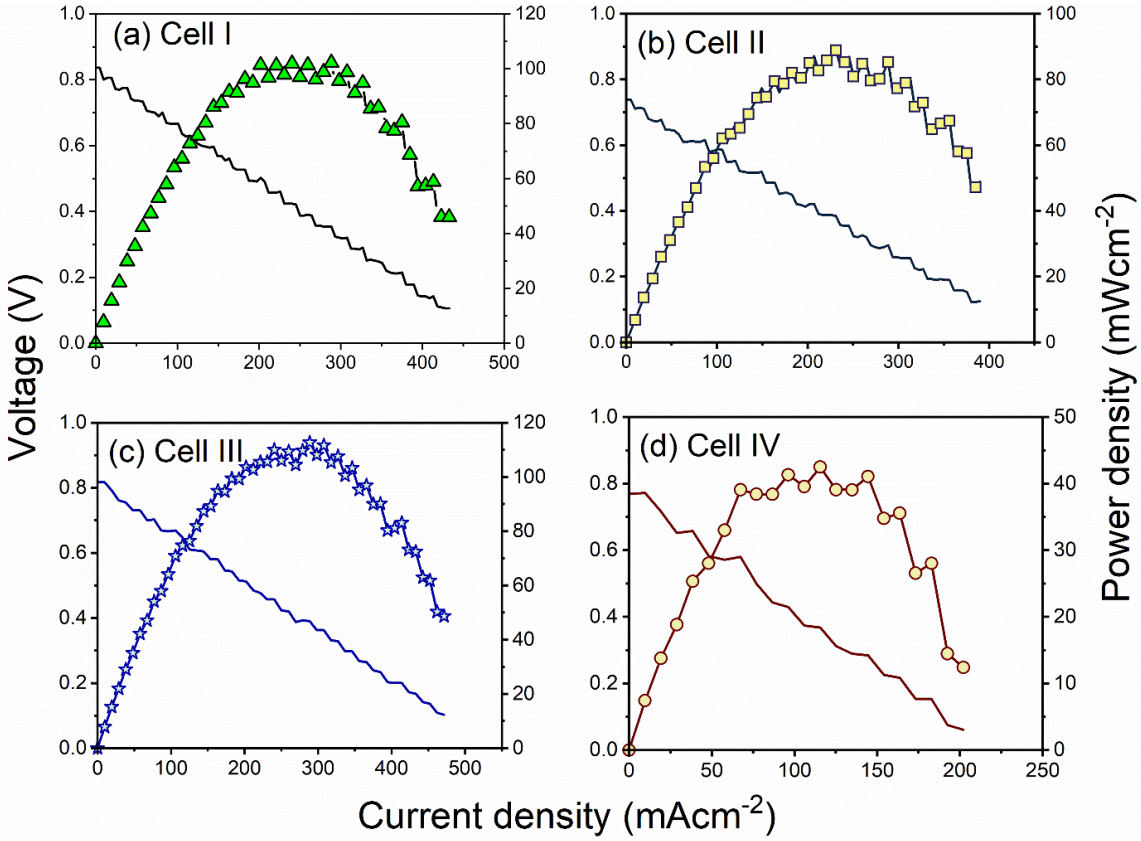

Fig 5.9 I-V curves of (a) Cell I containing $Ce_{0.9}Gd_{0.1}O_{1.950}$ (CG1), (b) Cell II containing $Ce_{0.925}Sr_{0.075}O_{1.925}$ (CS3), (c) Cell III containing $Ce_{0.875}Gd_{0.1}Sr_{0.025}O_{1.925}$ (CG1S1), and (d) Cell IV containing $Ce_{0.850}Gd_{0.1}Sr_{0.050}O_{1.925}$ (CG1S2) as the electrolyte measured at 600 °C

Table 5.4 The OCV and Power density of the cells measured at 500 °C and 600 °C

Cell	Electrolyte	OCV (V)		Power density ($mWcm^{-2}$)	
		500 °C	600 °C	500 °C	600 °C
I	CG1	0.784	0.837	60.7	102.2
II	CS3	0.792	0.739	81.6	88.9
III	CG1S1	0.853	0.817	94.0	112.7
IV	CG1S2	0.873	0.770	34.3	42.5

5.7 Summary

The four selected electrolytes (CG1, CS3, CG1S1, and CG1S2) are used to fabricate the fuel cells. After many trials and variations in the process of tape casting, a good tape was obtained using slurry A8. A dense electrolyte sandwiched between a porous anode and a porous cathode

is formed, as confirmed by the FESEM. The complete cell is studied in real SOFC conditions using hydrogen (3 % H_2O) as a fuel on the anode side and ambient air on the cathode side at 500 and 600 °C. The co-doping of the ceria with gadolinium and strontium enhances the performance of the cell as compared to the singly doped ceria due to the better density and reasonably good conductivity of this electrolyte. A maximum power density of 112.7 $mWcm^{-2}$ has been achieved for CG1S1 ($Ce_{0.875}Gd_{0.1}Sr_{0.025}O_{1.925}$) electrolyte. This implies that $Ce_{0.875}Gd_{0.1}Sr_{0.025}O_{1.925}$ can be a potential candidate as an electrolyte for intermediate-temperature solid oxide fuel cells.

Chapter 6

Conclusion and Future Scope

The effect of doping and co-doping of Gd and Sr on the structural, microstructural, and electrical properties of ceria-based electrolytes has been studied. Doping of Gd and Sr is expected to increase the electrical conductivity, densification, and other microstructural properties of the ceria. The co-doping effect of both Gd and Sr improves the overall performance of the electrolyte to be used in SOFC.

6.1 Conclusion

The conclusions drawn from the above studies are listed below:

1. The CeO_2, $Ce_{1-x}Gd_xO_{2-\delta}$ (x = 0, 0.1, 0.2, 0.3), $Ce_{1-y}Sr_yO_{2-\delta}$ (y=0.025, 0.05, 0.075, 0.10), and $Ce_{1-x-y}Gd_xSr_yO_{2-\delta}$ (x = 0.1, 0.2, y=0.025, 0.05, 0.075) samples have been successfully synthesized using ultrasonication assisted sol-gel auto combustion method with dense samples. The relative density is higher than 90 % for all the samples sintered at 1450 °C. The highest density for CS1, CS2, and CS3 samples is obtained due to the partial liquid phase sintering.
2. The dopants increase the thermal stability of CeO_2. The dopants prevent Ce^{4+} to reduce to Ce^{3+} which happens at the reducing conditions at high temperature.
3. The monophasic undoped and doped ceria with cubic fluorite structure is formed. The solid solubility limit of Gd, Sr, and Gd-Sr co-doped in ceria is ~20 %, ~7.5 %, and 5.0 %, respectively.
4. The dopants not only create oxygen vacancies but also delocalize them.

5. In undoped and doped samples, cerium is present in mixed states, i.e., Ce^{4+} and Ce^{3+} states. The doping of Sr prevents the conversion of Ce^{4+} to Ce^{3+}. The Raman spectra confirm the presence of the Gd_2O_3 impurity phase for concentrations higher than 20 %.
6. The highest conductivity is observed for 10 % Gd doped CeO_2 (1.67×10^{-2} Scm^{-1} at 600 °C), followed by 10 % Gd-2.5 % Sr doped ceria and then 10 % Gd and 5.0 % Sr doped ceria. Sr dopant acts as a sintering aid for CeO_2. Based on optimization and conductivity, the four samples, CG1, CS3, CG1S1, and CG1S2, are fabricated and tested in real SOFC conditions.
7. Single cells were successfully fabricated using selected electrolytes. Due to the co-doing effect, Gd and Sr co-doped ceria samples (CG1S1) showed the highest power density among these electrolytes with high density and high conductivity.
8. CG1S1 electrolyte has been tested for the first time in this fuel cell and it could be a potential candidate for ITSOFC applications.

6.2 Future scope

On the basis of the above conclusion, the following suggestions are recommended for the future investigations:

1. Different sintering aids can be used to enhance the relative density of the CeO_2 further.
2. Samples with different Gd concentrations between 20 and 30 % could be synthesized to know the exact solid solubility limit.
3. The optimized electrolyte, i.e., CG1S1, could be prepared using other routes, and the results could be compared.
4. The cell made in this case was anode-supported. The electrolyte should be tested with metal-supported cells as well. This process can reduce the wastage of anode material while making the tapes.

List of publications

1. Taranveer Kaur, K Singh, Jayant Kolte, Effect of intrinsic and extrinsic oxygen vacancies on the conductivity of Gd doped CeO_2 synthesized by sonochemical route, *The Journal of Physical Chemistry C* (2022), 126, 18018-18028. https://doi.org/10.1021/acs.jpcc.2c04851
2. Taranveer Kaur, Jayant Kolte, K Singh, Defect-induced improved electrical performance of doped ceria for solid oxide fuel cell applications, Ceramics International. (Accepted) https://doi.org/10.1016/j.ceramint.2024.02.182
3. Taranveer Kaur, K Singh, Jayant Kolte, Process parameters and their effect on structure and morphology of gadolinium doped ceria, *Materials Today: Proceedings* (2023), 80, 937-941. https://doi.org/10.1016/j.matpr.2022.11.331
4. Taranveer Kaur, K Singh, Jayant Kolte, Dual role of dopant SrO in CeO_2 and their effect on structure, microstructural and electrical properties, Ionics. (Accepted)
5. Taranveer Kaur, Jayant Kolte, K Singh, Improved performance of anode supported Gd and Sr co-doped ceria fuel cell for ITSOFC, (To be submitted).

Publications not included in the thesis

1. Taranveer Kaur, Shivani Punj, Ravindra Kumar, Kulvir Singh, Effect of minor phase (CuO) on sinterability, grain size, and dielectric properties of $CaCu_3Ti_4O_{12}$ ceramics, *App. Phys. A* (2020), 126, 1-6. http://dx.doi.org/10.1007/s00339-020-03963-y
2. Taranveer Kaur, Raman Kumar, Savidh Khan, Kulvir Singh, Jayant Kolte, Structural and electrical properties of Gd doped CeO2 (GDC) nanoceramics for solid oxide fuel cell applications, *Transactions of the Indian Ceramic Society* (2022), 81, 127-132. https://doi.org/10.1080/0371750X.2022.2115400
3. Taranveer Kaur, Jahnvi, K Singh, Jayant Kolte, Reducing the sintering temperature of Gadolinium-Doped Ceria electrolyte using different sintering aids (To Be Submitted).

List of conferences

1. Poster presentation in International Conference on Advanced Materials and Devices for Futuristic Applications (IC- AMDFA) at Chandigarh University, Chandigarh on 23 – 24 November, 2021.
2. Oral presentation in Global Conference on Recent Advancements in Sustainable Materials (GC-RASM 2022) held at AJ Institute of Engineering and Technology, Mangalore, Karnataka, India during 28 - 29, July 2022.
3. Oral presentation in National Conference on Physics and Chemistry of Materials-2023 held at Govt. Holkar (Model Autonomous) Science College, Indore.

References

[1] T.K. Maiti, J. Majhi, S.K. Maiti, J. Singh, P. Dixit, T. Rohilla, S. Ghosh, S. Bhushan, S. Chattopadhyay, Zirconia-and ceria-based electrolytes for fuel cell applications: critical advancements toward sustainable and clean energy production, Environ. Sci. Pollut. Res., 29 (2022) 64489-64512.
[2] S. Jo, B. Sharma, D.-H. Park, J.-h. Myung, Materials and nano-structural processes for use in solid oxide fuel cells: A review, Journal of the Korean Ceramic Society, 57 (2020) 135-151.
[3] Ryan O'hayre, Suk-won Cha, Whitney Colella, P. Fritz B, Fuel Cell Fundamentals, third ed., John Wiley & Sons, Hoboken, USA, 2016.
[4] K. Joon, Fuel cells–a 21st century power system, J. Power Sources, 71 (1998) 12-18.
[5] A.J. Appleby, Fuel cell handbook, New York, NY; Van Nostrand Reinhold Co. Inc., 1988.
[6] Y. Gao, M. Zhang, M. Fu, W. Hu, H. Tong, Z. Tao, A comprehensive review of recent progresses in cathode materials for Proton-conducting SOFCs, Energy Reviews, 2 (2023) 100038.
[7] A.L. Dicks, D.A.J. Rand, Fuel cell systems explained, John Wiley & Sons, 2018.
[8] A. Kasaeian, M. Javidmehr, M.R. Mirzaie, L. Fereidooni, Integration of Solid Oxide Fuel Cells with Solar Energy Systems: A Review, Appl. Therm. Eng., (2023) 120117.
[9] M.F. Rabuni, T. Li, M.H.D. Othman, F.H. Adnan, K. Li, Progress in Solid Oxide Fuel Cells with Hydrocarbon Fuels, Energies, 16 (2023) 6404.
[10] P. Kaur, K. Singh, Review of perovskite-structure related cathode materials for solid oxide fuel cells, Ceram. Int., 46 (2020) 5521-5535.
[11] S.K. Suraparaju, S.K. Natarajan, P. Karthikeyan, A succinct review on fuel cells, IOP Conference Series: Earth and Environmental Science, 312 (2019) 012012.
[12] Y. Tian, N. Abhishek, C. Yang, R. Yang, S. Choi, B. Chi, J. Pu, Y. Ling, J.T. Irvine, G. Kim, Progress and potential for symmetrical solid oxide electrolysis cells, Matter, 5 (2022) 482-514.
[13] M.Y. Lu, R. Scipioni, B.-K. Park, T. Yang, Y.A. Chart, S.A. Barnett, Mechanisms of PrO_x performance enhancement of oxygen electrodes for low and intermediate temperature solid oxide fuel cells, Mater. Today Energy, 14 (2019) 100362.
[14] N. Hedayat, Y. Du, H. Ilkhani, Review on fabrication techniques for porous electrodes of solid oxide fuel cells by sacrificial template methods, Renew. Sustain. Energy Rev., 77 (2017) 1221-1239.
[15] M.A. Alemu, M. Ilbas, Direct ammonia powered solid oxide fuel cells: challenges, opportunities, and future outlooks, J. Eng. Appl. Sci. Technol., 116 (2020) 2-11.
[16] L.S. Mahmud, A. Muchtar, M.R. Somalu, Challenges in fabricating planar solid oxide fuel cells: A review, Renew. Sustain. Energy Rev., 72 (2017) 105-116.
[17] K. Wei, X. Wang, R.A. Budiman, J. Kang, B. Lin, F. Zhou, Y. Ling, Progress in Ni-based anode materials for direct hydrocarbon solid oxide fuel cells, J. Mater. Sci., 53 (2018) 8747-8765.
[18] N. Mahato, A. Banerjee, A. Gupta, S. Omar, K. Balani, Progress in material selection for solid oxide fuel cell technology: A review, Prog. Mater Sci., 72 (2015) 141-337.
[19] M. Choolaei, M.F. Vostakola, B.A. Horri, Recent Advances and Challenges in Thin-Film Fabrication Techniques for Low-Temperature Solid Oxide Fuel Cells, Crystals, 13 (2023) 1008.
[20] J. Xiong, C. Jiao, M. Han, W. Yi, J. Ma, C. Yan, A high performance ceria-based solid oxide fuel cell operating on underground coal gasification gas, RSC Adv., 5 (2015) 87477-87483.

[21] R.C. Maher, P.R. Shearing, E. Brightman, D.J. Brett, N.P. Brandon, L.F. Cohen, Reduction dynamics of doped ceria, nickel oxide, and cermet composites probed using in situ Raman spectroscopy, Adv. Sci., 3 (2016) 1500146.
[22] L. Almar, B. Colldeforns, L. Yedra, S. Estrade, F. Peiró, A. Morata, T. Andreu, A. Tarancón, High-temperature long-term stable ordered mesoporous Ni–CGO as an anode for solid oxide fuel cells, J. Mater. Chem. A, 1 (2013) 4531-4538.
[23] Ö. Yıldız, A. Soydan, M. Akel, E. Ipçizade, A. Ata, Characterization of MO_y–$M_xCe_{1-x}O_{2-\delta}$ (M: Co, Ni & Cu) nano powders and anode materials for low and intermediate temperature solid oxide fuel cells, Int. J. Hydrogen Energy, 40 (2015) 14085-14094.
[24] Y. He, G. Chen, X. Zhang, L. Zhang, D. Yang, M.I. Asghar, S. Geng, P.D. Lund, Mechanism for major improvement in SOFC electrolyte conductivity when using Lithium compounds as anode, ACS Appl. Energy Mater., (2020).
[25] M. Shahid, C. He, S. Sankarasubramanian, V. Ramani, S. Basu, Enhanced methane electrooxidation by ceria and nickel oxide impregnated perovskite anodes in solid oxide fuel cells, Int. J. Hydrogen Energy, 45 (2020) 11287-11296.
[26] H. Shi, C. Su, R. Ran, J. Cao, Z. Shao, Electrolyte materials for intermediate-temperature solid oxide fuel cells, Prog. Nat. Sci.: Mater. Int, 30 (2020) 764-774.
[27] O. Corigliano, L. Pagnotta, P. Fragiacomo, On the technology of solid oxide fuel cell (SOFC) energy systems for stationary power generation: A review, Sustainability, 14 (2022) 15276.
[28] J.A. Kilner, M. Burriel, Materials for intermediate-temperature solid-oxide fuel cells, Annu. Rev. Mater. Res., 44 (2014) 365-393.
[29] M. Fallah Vostakola, B. Amini Horri, Progress in Material Development for Low-Temperature Solid Oxide Fuel Cells: A Review, Energies, 14 (2021) 1280.
[30] M. Stanislowski, J. Froitzheim, L. Niewolak, W.J. Quadakkers, K. Hilpert, T. Markus, L. Singheiser, Reduction of chromium vaporization from SOFC interconnectors by highly effective coatings, J. Power Sources, 164 (2007) 578-589.
[31] A. Topcu, B. Öztürk, Ö.N. Cora, Performance evaluation of machined and powder metallurgically fabricated Crofer® 22 APU interconnects for SOFC applications, Int. J. Hydrogen Energy, 47 (2022) 3437-3448.
[32] J.W. Fergus, Sealants for solid oxide fuel cells, J. Power Sources, 147 (2005) 46-57.
[33] J. Duquette, A. Petric, Silver wire seal design for planar solid oxide fuel cell stack, J. Power Sources, 137 (2004) 71-75.
[34] K. Singh, T. Walia, Review on silicate and borosilicate-based glass sealants and their interaction with components of solid oxide fuel cell, Int. J. Energy Res., 45 (2021) 20559-20582.
[35] I. Sreedhar, B. Agarwal, P. Goyal, A. Agarwal, An overview of degradation in solid oxide fuel cells-potential clean power sources, J. Solid State Electrochem., 24 (2020) 1239-1270.
[36] J. Laurencin, G. Delette, O. Sicardy, S. Rosini, F. Lefebvre-Joud, Impact of 'redox' cycles on performances of solid oxide fuel cells: Case of the electrolyte supported cells, J. Power Sources, 195 (2010) 2747-2753.
[37] S. Yang, T. Chen, Y. Wang, Z. Peng, W.G. Wang, Electrochemical analysis of an anode-supported SOFC, Int. J. Electrochem. Sci., 8 (2013) 2330-2344.
[38] M. Ilbas, B. Kumuk, Numerical modelling of a cathode-supported solid oxide fuel cell (SOFC) in comparison with an electrolyte-supported model, J. Energy Inst., 92 (2019) 682-692.
[39] G. Chen, H.-X. You, Y. Kasai, H. Sato, A. Abudula, Characterization of planer cathode-supported SOFC prepared by a dual dry pressing method, J. Alloys Compd., 509 (2011) 5159-5162.

[40] M.E. Navarro, X.G. Capdevila, M. Morales, J.J. Roa, M. Segarra, Manufacturing of anode-supported tubular solid oxide fuel cells by a new shaping technique using aqueous gel-casting, J. Power Sources, 200 (2012) 45-52.
[41] C. Ding, H. Lin, K. Sato, T. Hashida, A simple, rapid spray method for preparing anode-supported solid oxide fuel cells with GDC electrolyte thin films, J. Membr. Sci., 350 (2010) 1-4.
[42] V.V. Krishnan, Recent developments in metal-supported solid oxide fuel cells, WIREs Energy and Environment, 6 (2017) e246.
[43] M. Fallah Vostakola, H. Ozcan, R.S. El-Emam, B. Amini Horri, Recent Advances in High-Temperature Steam Electrolysis with Solid Oxide Electrolysers for Green Hydrogen Production, Energies, 16 (2023) 3327.
[44] M. Mogensen, N.M. Sammes, G.A. Tompsett, Physical, chemical and electrochemical properties of pure and doped ceria, Solid State Ion., 129 (2000) 63-94.
[45] M. Coduri, S. Checchia, M. Longhi, D. Ceresoli, M. Scavini, Rare earth doped ceria: The complex connection between structure and properties, Front. Chem., 6 (2018) 526.
[46] S. Anirban, A. Dutta, Revisiting ionic conductivity of rare earth doped ceria: Dependency on different factors, Int. J. Hydrogen Energy, 45 (2020) 25139-25166.
[47] D.W. Jung, K.T. Lee, E.D. Wachsman, Dysprosium and gadolinium double doped bismuth oxide electrolytes for low temperature solid oxide fuel cells, J. Electrochem. Soc., 163 (2016) F411.
[48] B.-H. Yun, K.J. Kim, D.W. Joh, M.S. Chae, J.J. Lee, D.-w. Kim, S. Kang, D. Choi, S.-T. Hong, K.T. Lee, Highly active and durable double-doped bismuth oxide-based oxygen electrodes for reversible solid oxide cells at reduced temperatures, J. Mater. Chem. A, 7 (2019) 20558-20566.
[49] G. Pasciak, J. Chmielowiec, Novel intermediate temperature solid oxide fuel cell based on La-doped $Bi_4V_2O_{11}$ electrolyte, Adv. Appl. Ceram., 120 (2021) 215-221.
[50] R. Kant, K. Singh, O.P. Pandey, Microstructural and electrical behavior of $Bi_4V_{2-x}Cu_xO_{11-\delta}$ ($0 \leq x \leq 0.4$), Ceram. Int., 35 (2009) 221-227.
[51] S. Thakur, M. Devi, K. Singh, Structural and optical properties of La and Gd substituted $Bi_{4-x}M_xV_2O_{11-\delta}$ ($0.1 \leq x \leq 0.3$), Ionics, 20 (2014) 73-81.
[52] R. Kant, K. Singh, O.P. Pandey, Structural, thermal and transport properties of $Bi_4V_{2-x}Ga_xO_{11-d}$ ($0 \leq x \leq 0.4$), Ionics, 16 (2010) 277-282.
[53] J. Yu, H. Liu, X. Chen, J. Xing, B. Yuan, M. Wang, W. Ma, Ionic conductivity and crystal structure of LSGM with different element mole ratios, Fuel Cells, 21 (2021) 149-154.
[54] G.M. Rupp, M. Glowacki, J. Fleig, Electronic and ionic conductivity of $La_{0.95}Sr_{0.05}Ga_{0.95}Mg_{0.05}O_{3-\delta}$ (LSGM) single crystals, J. Electrochem. Soc., 163 (2016) F1189.
[55] M. Feng, J.B. Goodenough, A superior oxide-ion conductor, Eur. J. Solid Inorg. Chem, 31 (1994) 663-672.
[56] K. Huang, R.S. Tichy, J.B. Goodenough, Superior perovskite oxide-ion conductor; strontium-and magnesium-doped LaGaO3: I, phase relationships and electrical properties, J. Am. Ceram. Soc., 81 (1998) 2565-2575.
[57] T. Ishihara, H. Matsuda, Y. Takita, Doped $LaGaO_3$ Perovskite Type Oxide as a New Oxide Ionic Conductor, J. Am. Chem. Soc., 116 (1994) 3801-3803.
[58] K.T. Bae, I. Jeong, D. Kim, H. Yu, H.-N. Im, A. Akromjon, C.-W. Lee, K.T. Lee, Highly active cobalt-free perovskites with Bi doping as bifunctional oxygen electrodes for solid oxide cells, Chem. Eng. J., 461 (2023) 142051.
[59] I. Stijepovic, A.J. Darbandi, V.V. Srdic, Conductivity of Co and Ni doped lanthanum-gallate synthesized by citrate sol–gel method, Ceram. Int., 39 (2013) 1495-1502.

[60] E. Filonova, D. Medvedev, Recent progress in the design, characterisation and application of $LaAlO_3$-and $LaGaO_3$-based solid oxide fuel cell electrolytes, Nanomaterials, 12 (2022) 1991.
[61] V. Thangadurai, W. Weppner, Studies on electrical properties of $La_{0.8}Sr_{0.2}Ga_{0.8}Mg_{0.2}O_{2.80}$ (LSGM) and LSGM–$SrSn_{1-x}Fe_xO_3$ (x = 0.8; 0.9) composites and their chemical reactivity, Electrochim. Acta, 50 (2005) 1871-1877.
[62] J. Ralph, A. Schoeler, M. Krumpelt, Materials for lower temperature solid oxide fuel cells, J. Mater. Sci., 36 (2001) 1161-1172.
[63] A. Tarancón, Strategies for lowering solid oxide fuel cells operating temperature, Energies, 2 (2009) 1130-1150.
[64] M.F. Öksüzömer, G. Dönmez, V. Sariboğa, T.G. Altinçekiç, Microstructure and ionic conductivity properties of gadolinia doped ceria ($Gd_xCe_{1-x}O_{2-x/2}$) electrolytes for intermediate temperature SOFCs prepared by the polyol method, Ceram. Int., 39 (2013) 7305-7315.
[65] B.S. Prakash, R. Pavitra, S.S. Kumar, S. Aruna, Electrolyte bi-layering strategy to improve the performance of an intermediate temperature solid oxide fuel cell: A review, J. Power Sources, 381 (2018) 136-155.
[66] S.J. Skinner, J.A. Kilner, Oxygen ion conductors, Mater. Today, 6 (2003) 30-37.
[67] W. Huang, P. Shuk, M. Greenblatt, Hydrothermal Synthesis and Properties of $Ce_{1-x}Sm_xO_{2-x/2}$ and $Ce_{1-x}Ca_xO_{2-x}$ Solid Solutions, Chem. Mater., 9 (1997) 2240-2245.
[68] G. Kim, N. Lee, K.-B. Kim, B.-K. Kim, H. Chang, S.-J. Song, J.-Y. Park, Various synthesis methods of aliovalent-doped ceria and their electrical properties for intermediate temperature solid oxide electrolytes, Int. J. Hydrogen Energy, 38 (2013) 1571-1587.
[69] N. Chaubey, B. Wani, S. Bharadwaj, M. Chattopadhyaya, Physicochemical properties of rare earth doped ceria $Ce_{0.9}Ln_{0.1}O_{1.95}$ (Ln= Nd, Sm, Gd) as an electrolyte material for IT-SOFC/SOEC, Solid State Sci., 20 (2013) 135-141.
[70] T.-H. Lee, S.-S. Baek, K.-Y. Park, Y. Seo, B. Park, H.-T. Lim, J.-Y. Park, Enhanced performance of intermediate temperature-solid oxide fuel cells with a bimodal shape $Nd_{0.2}Ce_{0.8}O_{2-\delta}$ electrolyte, J. Alloys Compd., 706 (2017) 330-339.
[71] M.R. Cesário, E. Savary, S. Marinel, B. Raveau, V. Caignaert, Synthesis and electrochemical performance of $Ce_{1-x}Yb_xO_{2-x/2}$ solid electrolytes: The potential of microwave sintering, Solid State Ion., 294 (2016) 67-72.
[72] K. Park, H. Hwang, Fabrication and electrical properties of nanocrystalline Dy^{3+}-doped CeO_2 for intermediate-temperature solid oxide fuel cells, Energy, 55 (2013) 304-309.
[73] I. Shajahan, J. Ahn, P. Nair, S. Medisetti, S. Patil, V. Niveditha, G.U.B. Babu, H.P. Dasari, J.-H. Lee, Praseodymium doped ceria as electrolyte material for IT-SOFC applications, Mater. Chem. Phys., 216 (2018) 136-142.
[74] K. Anjaneya, G. Nayaka, J. Manjanna, V.A. Kumar, G. Govindaraj, K.J.J.o.A. Ganesha, Investigation on the Sr-doped ceria $Ce_{1-x}Sr_xO_{2-\delta}$ (x= 0.05–0.2) as an electrolyte for intermediate temperature SOFC, J. Alloys Compd., 598 (2014) 33-40.
[75] V. Venkatesh, C.V. Reddy, Thermal and electrical properties of $Ce_{0.8-x}Pr_xSm_{0.2}O_{2-\delta}$ electrolyte materials for IT-SOFC applications, Ionics, 23 (2017) 3455-3467.
[76] A.V. Coles-Aldridge, R.T. Baker, Ionic conductivity in multiply substituted ceria-based electrolytes, Solid State Ion., 316 (2018) 9-19.
[77] A. Arabaci, Synthesis and characterization of Pr/Gd co-doped ceria by using the citric acid-nitrate combustion method, Solid State Ion., 326 (2018) 69-76.
[78] A. Arabacı, M. Öksüzömer, Ionic Conductivity of $Ce_{0.9-x}Gd_{0.1}Sm_xO_{2-\delta}$ co-doped Ceria Electrolytes, Acta Phys. Pol., A, 134 (2018) 122-124.
[79] N. Singh, O. Parkash, D. Kumar, Preparation and characterization of Al and La co-doped ($Ce_{1-x-y}Al_xLa_yO_{2-(x+y)/2}$) ceria, Ionics, 19 (2013) 165-170.

[80] V. Vijaykumar, G. Nirala, D. Yadav, U. Kumar, S. Upadhyay, Sucrose-nitrate auto combustion synthesis of $Ce_{0.85}Ln_{0.10}Sr_{0.05}O_{2-\delta}$ (Ln= La and Gd) electrolytes for solid oxide fuel cells, Int. J. Energy Res., 44 (2020) 4652-4663.
[81] K. Bhongale, S. Shirbhate, S. Acharya, Effect of sintering temperature on structural and electrical properties of co-doped ceria based electrolyte material for IT-SOFCs, AIP Conf. Proc., 2220 (2020) 020141.
[82] M. Dudek, Some structural aspects of ionic conductivity in co-doped ceria-based electrolytes, Arch. Metall. Mater., 58 (2013) 1355-1359.
[83] A. Venkatasubramanian, P. Gopalan, T.R.S. Prasanna, Synthesis and characterization of electrolytes based on $BaO–CeO_2–GdO_{1.5}$ system for Intermediate Temperature Solid Oxide Fuel Cells, Int. J. Hydrogen Energy, 35 (2010) 4597-4605.
[84] M. Biesuz, G. Dell'Agli, L. Spiridigliozzi, C. Ferone, V.M. Sglavo, Conventional and field-assisted sintering of nanosized Gd-doped ceria synthesized by co-precipitation, Ceram. Int., 42 (2016) 11766-11771.
[85] M. Alaydrus, M. Sakaue, S.M. Aspera, T.D. Wungu, T.P. Linh, H. Kasai, T. Ishihara, T. Mohri, A first-principles study on defect association and oxygen ion migration of Sm^{3+} and Gd^{3+} co-doped ceria, J. Phys.: Condens. Matter, 25 (2013) 225401.
[86] A. Arabacı, T.G. Altınçekiç, M. Der, M.A.F. Öksüzömer, Preparation and properties of ceramic electrolytes in the Nd and Gd Co-doped ceria systems prepared by polyol method, J. Alloys Compd., 792 (2019) 1141-1149.
[87] R. Gerhardt, A.S. Nowick, Grain-boundary effect in ceria doped with trivalent cations: I, electrical measurements, J. Am. Ceram. Soc., 69 (1986) 641-646.
[88] G. Accardo, C. Ferone, R. Cioffi, D. Frattini, L. Spiridigliozzi, G. Dell'Agli, Electrical and microstructural characterization of ceramic gadolinium-doped ceria electrolytes for ITSOFCs by sol-gel route, J. Appl. Biomater. Funct. Mater., 14 (2016) 35-41.
[89] G. Accardo, L. Spiridigliozzi, R. Cioffi, C. Ferone, E. Di Bartolomeo, S.P. Yoon, G. Dell'Agli, Gadolinium-doped ceria nanopowders synthesized by urea-based homogeneous co-precipitation (UBHP), Mater. Chem. Phys., 187 (2017) 149-155.
[90] S.R. Ali, R. Kumar, A. Kalam, A.G. Al-Sehemi, M.C. Arya, Effect of Strontium Doping on the Band Gap of CeO_2 Nanoparticles Synthesized Using Facile Co-precipitation, Arab. J. Sci. Eng . 44 (2019) 6295-6302.
[91] D.H. Prasad, H.-R. Kim, J.-S. Park, J.-W. Son, B.-K. Kim, H.-W. Lee, J.-H. Lee, Superior sinterability of nano-crystalline gadolinium doped ceria powders synthesized by co-precipitation method, J. Alloys Compd., 495 (2010) 238-241.
[92] G. Dell'Agli, L. Spiridigliozzi, A. Marocco, G. Accardo, C. Ferone, R. Cioffi, Effect of the mineralizer solution in the hydrothermal synthesis of gadolinium-doped (10% mol Gd) ceria nanopowders, J. Appl. Biomater. Funct. Mater., 14 (2016) 189-196.
[93] K. Mužina, S. Kurajica, G. Dražić, P. Guggenberger, G. Matijašić, True doping levels in hydrothermally derived copper-doped ceria, J. Nanopart. Res., 23 (2021) 1-14.
[94] A.S. Saleemi, A. Abdullah, M. Anis-Ur-Rehman, THERMOPHYSICAL PROPERTIES OF Gd DOPED CERIA NANOPARTICLES, Dig. J. Nanomater. Bios., 12 (2017) 19-28.
[95] S. Kulkarni, S. Duttagupta, G. Phatak, Study of glycine nitrate precursor method for the synthesis of gadolinium doped ceria ($Ce_{0.8}Gd_{0.2}O_{1.90}$) as an electrolyte for intermediate temperature solid oxide fuel cells, RSC Adv., 4 (2014) 46602-46612.
[96] B. Matovic, D. Bucevac, N. Jiraborvornpongsa, K. Yoshida, T. Yano, Synthesis and characterization of nanometric strontium-doped ceria solid solutions via glycine-nitrate procedure, J. Ceram. Soc. Jpn., 120 (2012) 69-73.
[97] X. Li, Z. Feng, J. Lu, F. Wang, M. Xue, G. Shao, Synthesis and electrical properties of $Ce_{1-x}Gd_xO_{2-x/2}$ (x= 0.05–0.3) solid solutions prepared by a citrate–nitrate combustion method, Ceram. Int., 38 (2012) 3203-3207.

[98] V.R. Mangalaraja, S. Ananthakumar, M. Paulraj, K. Uma, M. López, P.C. Camurri, E.R. Avila, Electrical and thermal properties of 10 mol% Gd^{3+} doped ceria electrolytes synthesized through citrate combustion technique, Process. Appl. Ceram., 3 (2009) 137-143.
[99] P. Ramos-Alvarez, M. Villafuerte-Castrejón, G. González, M. Cassir, C. Flores-Morales, J. Chávez-Carvayar, Ceria-based electrolytes with high surface area and improved conductivity for intermediate temperature solid oxide fuel cells, J. Mater. Sci., 52 (2017) 519-532.
[100] N. Jaiswal, N.K. Singh, D. Kumar, O. Parkash, Effect of strontium (Sr) doping on the conductivity of ceria, J. Power Sources, 202 (2012) 78-84.
[101] A. Akter, J. Pietras, S. Gopalan, Heavily neodymium doped ceria as an effective barrier layer in solid oxide electrochemical cells, Int. J. Hydrogen Energy, 47 (2022) 33429-33438.
[102] S. Anirban, P.T. Das, A. Dutta, Effect of divalent cation addition on structure, conductivity and grain boundary properties in La doped ceria oxygen ion conductors, Ceram. Int., 45 (2019) 5751-5760.
[103] K. Tanwar, N. Jaiswal, D. Kumar, O. Parkash, Synthesis & characterization of Dy and Ca Co-doped ceria based solid electrolytes for IT-SOFCs, J. Alloys Compd., 684 (2016) 683-690.
[104] A.I. Ivanov, S.I. Bredikhin, V.V. Kharton, Mixed Ionic-Electronic Conductivity of the Fluorite-Type $Ce_{1-x-y}La_xPr_yO_{2-\delta}$ Solid Solutions under Reducing Conditions, Russ. J. Electrochem., 58 (2022) 122-130.
[105] J. Molenda, K. Świerczek, W. Zając, Functional materials for the IT-SOFC, J. Power Sources, 173 (2007) 657-670.
[106] K.C. Anjaneya, G.P. Nayaka, J. Manjanna, G. Govindaraj, K.N. Ganesha, Studies on structural, morphological and electrical properties of $Ce_{0.8}Ln_{0.2}O_{2-\delta}$ (Ln= Y^{3+}, Gd^{3+}, Sm^{3+}, Nd^{3+} and La^{3+}) solid solutions prepared by citrate complexation method, J. Alloys Compd., 585 (2014) 594-601.
[107] S. Kuharuangrong, Ionic conductivity of Sm, Gd, Dy and Er-doped ceria, J. Power Sources, 171 (2007) 506-510.
[108] B.C. Steele, Appraisal of $Ce_{1-y}Gd_yO_{2-y/2}$ electrolytes for IT-SOFC operation at 500 °C, Solid State Ion., 129 (2000) 95-110.
[109] Y. Zheng, H. Gu, H. Chen, L. Gao, X. Zhu, L. Guo, Effect of Sm and Mg co-doping on the properties of ceria-based electrolyte materials for IT-SOFCs, Mater. Res. Bull., 44 (2009) 775-779.
[110] N. Jaiswal, D. Kumar, S. Upadhyay, O. Parkash, Effect of Mg and Sr co-doping on the electrical properties of ceria-based electrolyte materials for intermediate temperature solid oxide fuel cells, J. Alloys Compd., 577 (2013) 456-462.
[111] S. Jaidka, S. Khan, K. Singh, Na_2O doped CeO_2 and their structural, optical, conducting and dielectric properties, Phys. B: Condens. Matter, 550 (2018) 189-198.
[112] H. Yahiro, T. Ohuchi, K. Eguchi, H. Arai, Electrical properties and microstructure in the system ceria-alkaline earth oxide, J. Mater. Sci., 23 (1988) 1036-1041.
[113] N. Momin, J. Manjanna, S. Kobayashi, S.T. Aruna, S. Senthil Kumar, G.P. Nayaka, Synthesis and ionic conductivity of calcium-doped ceria relevant to solid oxide fuel cell applications, Mater. Adv., 3 (2022) 8780-8791.
[114] S.I. Ahmad, P. Koteshwar Rao, I.A. Syed, Sintering temperature effect on density, structural and morphological properties of Mg-and Sr-doped ceria, J. Taibah Univ. Sci., 10 (2016) 381-385.
[115] T.-H. Yeh, C.-C. Chou, Ionic conductivity investigation in samarium and strontium co-doped ceria system, Phys. Scr., 2007 (2007) 303.
[116] P. Koteswararao, M.B. Suresh, B.N. Wani, P.V.B. Rao, L.D. Jadhav, Synthesis, structural and morphological studies of Sr^{2+} and Gd^{3+} co-doped Ceria electrolyte system for LT-SOFC, 330 012029.

[117] F. Meng, N. Lin, T. Xia, J. Wang, Z. Shi, J. Lian, Q. Li, H. Zhao, F. Ma, Neodymium-doped ceria nanomaterials: facile low-temperature synthesis and excellent electrical properties for IT-SOFCs, RSC Adv., 3 (2013) 6290-6294.
[118] P.S. Ong, Y.P. Tan, Y.H. Taufiq-Yap, Z. Zainal, Improved sinterability and conductivity enhancement of 10-mol% calcium-doped ceria using different fuel-aided combustion reactions and its structural characterisation, Mater. Sci. Eng. B, 185 (2014) 26-36.
[119] M. Anwar, M.A. S.A, A. Muchtar, M.R. Somalu, Influence of strontium co-doping on the structural, optical, and electrical properties of erbium-doped ceria electrolyte for intermediate temperature solid oxide fuel cells, Ceram. Int., 45 (2019) 5627-5636.
[120] S. Ramesh, G. Rajitha, Structural characterization and electrical properties of $Ce_{1-x}Sm_xO_{2-\delta}$ by sucrose-pectin–assisted auto combustion process, Ionics, 26 (2020) 5089-5098.
[121] N. Jaiswal, S. Upadhyay, D. Kumar, O. Parkash, Ionic conductivity investigation in lanthanum (La) and strontium (Sr) co-doped ceria system, J. Power Sources, 222 (2013) 230-236.
[122] S. Shirbhate, R.N. Nayyar, P.K. Ojha, A.K. Yadav, S. Acharya, Exploration of atomic scale changes during oxygen vacancy dissociation mechanism in nanostructure co-doped ceria: as electrolytes for IT-SOFC, J. Electrochem. Soc., 166 (2019) F544-F554.
[123] S. Ramesh, Electrical Properties of $Ce_{0.8}Dy_{0.175}Ca_{0.025}O_{2-\delta}$, J. Electron. Mater., 50 (2021) 4333-4345.
[124] D. Kashyap, P.K. Patro, R.K. Lenka, T. Mahata, P.K. Sinha, Effects of Gd and Sr co-doping in CeO_2 for electrolyte application in solid oxide fuel cell (SOFC), Ceram. Int., 40 (2014) 11869-11875.
[125] M. Chen, H. Gao, L. Zhang, Y. Xuan, J. Ren, M. Ni, Z. Lin, Unlocking the nature of the co-doping effect on the ionic conductivity of CeO_2-based electrolyte, Ceram. Int., 45 (2019) 3977-3985.
[126] K. Venkataramana, C. Madhuri, Y.S. Reddy, G. Bhikshamaiah, C.V. Reddy, Structural, electrical and thermal expansion studies of tri-doped ceria electrolyte materials for IT-SOFCs, J. Alloys Compd., 719 (2017) 97-107.
[127] M. Stojmenović, M. Žunić, J. Gulicovski, D. Bajuk-Bogdanović, I. Holclajtner-Antunović, V. Dodevski, S. Mentus, Structural, morphological, and electrical properties of doped ceria as a solid electrolyte for intermediate-temperature solid oxide fuel cells, J. Mater. Sci., 50 (2015) 3781-3794.
[128] A. Abdullah, A. Saleemi, M. Anis-ur-Rehman, Temperature and frequency dependence of transport phenomena in co-doped rare earth oxides nanoparticles for ITSOFCs, J. Alloys Compd., 632 (2015) 695-700.
[129] J. Yu, L. Wang, L. Luo, L. Cheng, X. Xu, Z. Wang, Bifunctional $Ce_{0.9}Gd_{0.09}M_{0.01}O_{2-\delta}$ (M= Fe, Cu) interlayers with micro-doping for high-performance solid oxide fuel cells, Ceram. Int., 50 (2024) 360-369.
[130] F. Aydın Ünal, Synthesis and characterization of (La, Cu) co-doped CeO_2 nanomaterials used as electrolyte material in SOFC applications, Appl. Phys. A, 129 (2023) 817.
[131] R. Liu, F. Zhou, J. Gao, Y. Zhang, J. Bao, X. Song, Synthesis and characterization of $Ce_{0.95-x}Dy_xCa_{0.02}Bi_{0.03}O_{2-\delta}$ solid electrolytes for IT-SOFCs, Ionics, (2022) 1-14.
[132] H. Chen, H. Zhu, S. Shen, K. Zheng, Y. Ling, S. Wang, X. Wang, Numerical study on charge transport and electrochemical performance of Gd and Pr co-doped ceria-based solid oxide fuel cells free from internal shorting, Ionics, 28 (2022) 3445-3452.
[133] Z. Fu, S. Wang, Y. Zheng, W. Pan, J. Liu, H. Wang, Q. Guan, Co-sintering synthesis of Yb^{3+} and Sm^{3+} co-doped CeO_2/NiO composite as a solid electrolyte and its electrochemical properties, Int. J. Electrochem. Sci., 17 (2022) 220565.
[134] S. Ramesh, Preparation and structural, microstructural, and electrical properties of $Ce_{0.83}Sm_{0.085}Pr_{0.085}O_{2-\delta}$ electrolyte material, J. Phys. Chem. Solids, 160 (2022) 110364.

[135] P.C.C. Daza, J.L. de Almeida Ferreira, J.A. Araujo, J.A.E. Paiva, R.A.M. Meneses, C.R.M. da Silva, Conductivity and microstructural evaluation of SGDC solid electrolytes synthetized by Pechini and controlled precipitation, Bol. Soc. Esp. Cerám. Vidr, 61 (2022) 541-551.
[136] Y. Liu, H. Qin, M. Li, J. Cheng, C. Tang, J. Xiao, Y. Xie, Direct synthesis of $Ce_{0.8}Sm_{0.2-x}Zn_xO_{2-\delta}$ electrolyte by sol–gel for IT-SOFC, Ionics, 28 (2022) 4675-4684.
[137] R. Liu, F. Zhou, J. Gao, Y. Zhang, J. Bao, X. Song, Synthesis and characterization of $Ce_{0.95-x}Dy_xCa_{0.02}Bi_{0.03}O_{2-\delta}$ solid electrolytes for IT-SOFCs, Ionics, 29 (2023) 271-284.
[138] A.V. Coles-Aldridge, R.T. Baker, Oxygen ion conductivity in ceria-based electrolytes co-doped with samarium and gadolinium, Solid State Ion., 347 (2020) 115255
[139] K. Venkataramana, C. Madhuri, C. Madhusudan, A. Bhogi, B. Srinivas, C.V. Reddy, Influence of La^{3+}, Sm^{3+} and Dy^{3+} dopants on ceria solid electrolytes for IT–SOFCs, Mater. Sci. Semicond. Process., 142 (2022) 106495.
[140] C. Madhusudan, K. Venkataramana, C. Madhuri, C. Vishnuvardhan Reddy, Structural, electrical and thermal studies on microwave sintered Dy and Pr co-doped ceria ceramics as electrolytes for intermediate temperature solid oxide fuel cells, J. Mater. Sci.: Mater. Electron., 29 (2018) 17067-17077.
[141] J. Yang, B. Ji, J. Si, Q. Zhang, Q. Yin, J. Xie, C. Tian, Synthesis and properties of ceria based electrolyte for IT-SOFCs, Int. J. Hydrogen Energy, 41 (2016) 15979-15984.
[142] S. Kobi, N. Jaiswal, D. Kumar, O. Parkash, Ionic conductivity of Nd^{3+} and Y^{3+} co-doped ceria solid electrolytes for intermediate temperature solid oxide fuel cells, J. Alloys Compd., 658 (2016) 513-519.
[143] C. Madhuri, K. Venkataramana, A. Nurhayati, C.V. Reddy, Effect of La^{3+} and Pr^{3+} co-doping on structural, thermal and electrical properties of ceria ceramics as solid electrolytes for IT-SOFC applications, Curr. Appl. Phys., 18 (2018) 1134-1142.
[144] B. Ji, C. Tian, C. Wang, T. Wu, J. Xie, M. Li, Preparation and characterization of $Ce_{0.8}Y_{0.2-x}Cu_xO_{2-\delta}$ as electrolyte for intermediate temperature solid oxide fuel cells, J. Power Sources, 278 (2015) 420-429.
[145] M. Mori, H. Sumi, E. Suda, Reducing the Gadolinium Dopant Content by Partial Substitution with Yttrium in a $Ce_{0.9}Gd_{0.1}O_{1.95}$-Based Oxide-Ion Conductor, J. Electrochem. Soc., 164 (2017) F1626-F1632.
[146] H. Bi, X. Liu, L. Zhu, J. Sun, S. Yu, H. Yu, L. Pei, Effect of MgO addition and grain size on the electrical properties of $Ce_{0.9}Gd_{0.1}O_{1.95}$ electrolyte for IT-SOFCs, Int. J. Hydrogen Energy, 42 (2017) 11735-11744.
[147] Z. Wang, Y. Zeng, C. Li, Z. Ye, L. Cao, Y. Zhang, Structures and electrical conductivities of Gd^{3+} and Fe^{3+} co-doped cerium oxide electrolytes sintered at low temperature for ILT-SOFCs, Ceram. Int., 44 (2018) 10328-10334.
[148] C. Tian, M. Zhu, X. Qu, Y. Liu, C. Wang, T. He, C. Chen, Effects of Bi_2O_3 doping on structural and electrical properties of $Ce_{0.8}Sm_{0.2}O_{1.9}$ electrolyte for solid oxide fuel cells, Int. J. Electrochem. Sci., (2023) 100432.
[149] R.M. Kasse, J.C. Nino, Ionic conductivity of $Sm_xNd_yCe_{0.9}O_{2-\delta}$ codoped ceria electrolytes, J. Alloys Compd., 575 (2013) 399-402.
[150] R.K. Lenka, T. Mahata, A.K. Tyagi, P.K. Sinha, Influence of grain size on the bulk and grain boundary ion conduction behavior in gadolinia-doped ceria, Solid State Ion., 181 (2010) 262-267.
[151] M.G. Bellino, D.G. Lamas, N.E. Walsöe de Reca, Enhanced ionic conductivity in nanostructured, heavily doped ceria ceramics, Adv. Funct. Mater., 16 (2006) 107-113.
[152] G. Accardo, D. Frattini, H. Ham, J. Han, S. Yoon, Improved microstructure and sintering temperature of bismuth nano-doped GDC powders synthesized by direct sol-gel combustion, Ceram. Int., 44 (2018) 3800-3809.

[153] L.B. Winck, J.L. de Almeida Ferreira, J.M.G. Martinez, J.A. Araujo, A.C.M. Rodrigues, C.R.M. da Silva, Synthesis, sintering and characterization of ceria-based solid electrolytes codoped with samaria and gadolinium using the Pechini method, Ceram. Int., 43 (2017) 16408-16415.
[154] N.C. Priya, K. Sandhya, D.N. Rajendran, Study on Electrical conductivity and Activation Energy of doped Ceria nanostructures, EETECH, 3 (2018) 49-53.
[155] H. Song, T. Wang, H. Wang, Y. Ma, W. Yang, D. Yan, D. Wang, R. Liu, Effect of precursor powder uniformity on structure and electrical properties of gadolinium-doped cerium oxide ceramics, Process. Appl. Ceram., 16 (2022) 42-47.
[156] D. GÜÇTaŞ, V. SaribоĞA, M.A.F. ÖKsÜZÖMer, Microstructure and ionic conductivity investigation of samarium doped ceria ($Sm_{0.2}Ce_{0.8}O_{1.9}$) electrolytes prepared by the templating methods, Turk. J. Chem., 46 (2022) 910-922.
[157] C. Goulart, E. Djurado, Synthesis and sintering of Gd-doped CeO_2 nanopowders prepared by ultrasonic spray pyrolysis, J. Eur. Ceram. Soc., 33 (2013) 769-778.
[158] D.A. Zatsepin, D.W. Boukhvalov, A.F. Zatsepin, Y.A. Kuznetsova, M.A. Mashkovtsev, V.N. Rychkov, V.Y. Shur, A.A. Esin, E.Z. Kurmaev, Electronic structure, charge transfer, and intrinsic luminescence of gadolinium oxide nanoparticles: Experiment and theory, Appl. Surf. Sci., 436 (2018) 697-707.
[159] K.C. Anjaneya, M.P. Singh, Synthesis and properties of gadolinium doped ceria electrolyte for IT-SOFCs by EDTA-citrate complexing method, J. Alloys Compd., 695 (2017) 871-876.
[160] S. Dey, D. Choudhury, M. Choudhuri, A. Bhattacharya, J. Mukhopadhyay, A. Das Sharma, M. Mukhopadhyay, Facile synthesis of doped ceria-based oxide by co-precipitation technique and performance evaluation in solid oxide fuel cell, Int. J. Appl. Ceram. Technol., 17 (2020) 1769-1784.
[161] A. Gondolini, E. Mercadelli, A. Sanson, S. Albonetti, L. Doubova, S. Boldrini, Effects of the microwave heating on the properties of gadolinium-doped cerium oxide prepared by polyol method, J. Eur. Ceram. Soc., 33 (2013) 67-77.
[162] S. Anirban, A. Banerjee, A. Dutta, Synthesis route dependent structure, conductivity and dielectric properties of $Ce_{0.8}Gd_{0.2}O_{1.9}$ oxygen ion conductor: A comparative approach, Int. J. Hydrogen Energy, 46 (2021) 8210-8225.
[163] A.U. Hapsari, J. Raharjo, H. Yuliani, I.G.A. Suradharmika, R.D. Pravitasari, D.P. Sari, Synthesis and Characterization of Gadolinium doped Cerium ($Ce_{0,9}Gd_{0,1}O_{1,95}$) by using Various Carbonates as a Precipitant, 622 012011.
[164] A. Zarkov, A. Stanulis, T. Salkus, A. Kezionis, V. Jasulaitiene, R. Ramanauskas, S. Tautkus, A. Kareiva, Synthesis of nanocrystalline gadolinium doped ceria via sol–gel combustion and sol–gel synthesis routes, Ceram. Int., 42 (2016) 3972-3988.
[165] N.H. Menzler, D. Lavergnat, F. Tietz, E. Sominski, E. Djurado, W. Fischer, G. Pang, A. Gedanken, H.P. Buchkremer, Materials synthesis and characterization of 8YSZ nanomaterials for the fabrication of electrolyte membranes in solid oxide fuel cells, Ceram. Int., 29 (2003) 619-628.
[166] E.-H. Hyeong, S.-M. Bae, C.-R. Park, J.-S. Park, Y.-S. Yoo, H.-S. Yang, H. Hwang, Sonochemical synthesis of highly sinterable/nanocrystalline CeO_2-based electrolyte powders for intermediate-temperature solid oxide fuel cells, J. Ceram. Process. Res., 13 (2012) 349-352.
[167] H. Okkay, M. Bayramoğlu, M.F. Öksüzömer, Ultrasound assisted synthesis of Gd and Nd doped ceria electrolyte for solid oxide fuel cells, Ceram. Int., 39 (2013) 5219-5225.
[168] I. Unal, S. Meisuria, M. Choolaei, T.R. Reina, B.A. Horri, Synthesis and characteristics of nanocrystalline $Ni_{1-x}Co_xO$/GDC powder as a methane reforming catalyst for SOFCs, Ceram. Int., 44 (2018) 6851-6860.

[169] E.-H. Kim, S.-M. Bae, J.-H. Hwang, Electrochemical enhancement of GDC (Gd_2O_3-doped CeO_2)/SSC ($Sm_xSr_{1-x}CoO_3$) composite cathodes in solid oxide fuel cells prepared through the sonochemical synthesis of nanocrystalline GDC electrolytes, Ceram. Int., 40 (2014) 15875-15880.
[170] M.-H. Ko, J.-H. Hwang, Application of sonochemical processing to LSC ($La_{0.6}Sr_{0.4}CoO_3$)/SDC (Sm_2O_3-doped CeO_2) composite cathodes for solid oxide fuel cells involving CeO_2-based electrolytes, Ceram. Int., 42 (2016) 11548-11553.
[171] J.M. Costa, A.F. de Almeida Neto, Ultrasound-assisted electrodeposition and synthesis of alloys and composite materials: A review, Ultrason. Sonochem., 68 (2020) 105193.
[172] J.-Y. Zhang, Z.-H. Luo, H.-C. Jiang, J. Jiang, C.-H. Chen, J.-X. Zhang, Z.-Z. Gui, N. Xiao, Highly transparent cerium doped gadolinium gallium aluminum garnet ceramic prepared with precursors fabricated by ultrasonic enhanced chemical co-precipitation, Ultrason. Sonochem., 39 (2017) 792-797.
[173] A. Poulia, P.M. Sakkas, D.G. Kanellopoulou, G. Sourkouni, C. Legros, C. Argirusis, Preparation of metal–ceramic composites by sonochemical synthesis of metallic nano-particles and in-situ decoration on ceramic powders, Ultrason. Sonochem., 31 (2016) 417-422.
[174] S.P.S. Badwal, F.T. Ciacchi, Oxygen-ion conducting electrolyte materials for solid oxide fuel cells, Ionics, 6 (2000) 1-21.
[175] A. Tschöpe, S. Kilassonia, R. Birringer, The grain boundary effect in heavily doped cerium oxide, Solid State Ion., 173 (2004) 57-61.
[176] R. Gerhardt, A.S. Nowick, M.E. Mochel, I. Dumler, Grain-boundary effect in ceria doped with trivalent cations: II, Microstructure and microanalysis, J. Am. Ceram. Soc., 69 (1986) 647-651.
[177] J. Cheng, R. Xu, Y. Shi, A strategy for improving sinterability and electrical properties of gadolinium-doped ceria electrolyte using calcium oxide additive, J. Rare Earths, 39 (2021) 728-733.
[178] J. Cheng, R. Xu, Y. Shi, A strategy for improving sinterability and electrical properties of gadolinium-doped ceria electrolyte using calcium oxide additive, J. Rare Earths, (2020).
[179] D.K. Kim, P.-S. Cho, J.-H. Lee, D.-Y. Kim, H.-M. Park, G. Auchterlonie, J. Drennan, Mitigation of highly resistive grain-boundary phase in gadolinia-doped ceria by the addition of SrO, Electrochem. Solid-State Lett., 10 (2007) B91.
[180] P.-S. Cho, S.B. Lee, Y.H. Cho, D.-Y. Kim, H.-M. Park, J.-H. Lee, Effect of CaO concentration on enhancement of grain-boundary conduction in gadolinia-doped ceria, J. Power Sources, 183 (2008) 518-523.
[181] A. Arabacı, M.F. Öksüzömer, Preparation and characterization of 10 mol% Gd doped CeO_2 (GDC) electrolyte for SOFC applications, Ceram. Int., 38 (2012) 6509-6515.
[182] C. Fu, S.H. Chan, Q. Liu, X. Ge, G. Pasciak, Fabrication and evaluation of Ni-GDC composite anode prepared by aqueous-based tape casting method for low-temperature solid oxide fuel cell, Int. J. Hydrogen Energy, 35 (2010) 301-307.
[183] T.S. Zhang, J. Ma, H.T. Huang, P. Hing, Z.T. Xia, S.H. Chan, J.A. Kilner, Effects of dopant concentration and aging on the electrical properties of Y-doped ceria electrolytes, Solid State Sci., 5 (2003) 1505-1511.
[184] https://www.veqter.co.uk/residual-stress-measurement/x-ray-diffraction
[185] S. Sharma, S. Jaiswal, B. Duffy, A.K. Jaiswal, Nanostructured Materials for Food Applications: Spectroscopy, Microscopy and Physical Properties, Bioengineering, 6 (2019) 26.
[186] https://www.horiba.com/int/scientific/products/raman-imaging-and-spectrometers/
[187] A. Sachdeva, P.K. Singh, H.W. Rhee, Composite Materials: Properties, Characterisation, and Applications, CRC Press, 2021.
[188] https://www.norecs.com/index.php?page=Fuel+cell+SOFC

[189] M. Ramalinga Viswanathan, A. Solaiappan, U. Kasimayan, R. Jiménez, S. Uthayakumar, M. Lopez, C. Camurri, Synthesis and characterization of Gd^{3+} and Sm^{3+} ion doped ceria electrolytes through an in-situ sulphated combustion technique, J. Ceram. Process. Res., 13 (2012) 15-22.
[190] R.D. Shannon, Revised effective ionic radii and systematic studies of interatomic distances in halides and chalcogenides, Acta Crystallogr. A, 32 (1976) 751-767.
[191] Z. Tianshu, P. Hing, H. Huang, J. Kilner, Ionic conductivity in the CeO_2–Gd_2O_3 system ($0.05 \leq Gd/Ce \leq 0.4$) prepared by oxalate coprecipitation, Solid State Ion., 148 (2002) 567-573.
[192] A.J.M. Araújo, J.P.F. Grilo, F.J.A. Loureiro, L.I.V. Holz, D.A. Macedo, D.P. Fagg, C.A. Paskocimas, Proteic sol–gel synthesis of Gd-doped ceria: a comprehensive structural, chemical, microstructural and electrical analysis, J. Mater. Sci., 55 (2020) 16864-16878.
[193] D.D. Upadhyaya, R. Bhat, S. Ramanathan, S.K. Roy, H. Schubert, G. Petzow, Solute effect on grain growth in ceria ceramics, J. Eur. Ceram. Soc., 14 (1994) 337-341.
[194] H. Inaba, T. Nakajima, H. Tagawa, Sintering behaviors of ceria and gadolinia-doped ceria, Solid State Ion., 106 (1998) 263-268.
[195] N. Nafsin, J.A. Aguiar, T. Aoki, A.M. Thron, K. Van Benthem, R.H. Castro, Thermodynamics versus kinetics of grain growth control in nanocrystalline zirconia, Acta Mater., 136 (2017) 224-234.
[196] F. Liu, R. Kirchheim, Nano-scale grain growth inhibited by reducing grain boundary energy through solute segregation, J. Cryst. Growth, 264 (2004) 385-391.
[197] M.B. Suresh, J. Roy, The effect of strontium doping on densification and electrical properties of $Ce_{0.8}Gd_{0.2}O_{2-\delta}$ electrolyte for IT-SOFC application, Ionics, 18 (2012) 291-297.
[198] T. Sherwood, R.T. Baker, Effects of Strontium Content on the Microstructure and Ionic Conductivity of Samarium-Doped Ceria, Solids, 2 (2021) 293-313.
[199] W. Weber, K. Hass, J. McBride, Raman study of CeO_2: Second-order scattering, lattice dynamics, and particle-size effects, Phys. Rev. B, 48 (1993) 178.
[200] M. Gupta, A. Kumar, A. Sagdeo, P.R. Sagdeo, Doping-Induced Combined Fano and Phonon Confinement Effect in La-Doped CeO_2: Raman Spectroscopy Analysis, J. Phys. Chem. C, 125 (2021) 2648-2658.
[201] C. Mortalò, M. Boaro, E. Rebollo, V. Zin, E. Aneggi, M. Fabrizio, A. Trovarelli, Insights on the Interfacial Processes Involved in the Mechanical and Redox Stability of the $BaCe_{0.65}Zr_{0.20}Y_{0.15}O_{3-\delta}$–$Ce_{0.85}Gd_{0.15}O_{2-\delta}$ Composite, ACS Appl. Energy Mater., 3 (2020) 9877-9888.
[202] R. Schmitt, A. Nenning, O. Kraynis, R. Korobko, A.I. Frenkel, I. Lubomirsky, S.M. Haile, J.L. Rupp, A review of defect structure and chemistry in ceria and its solid solutions, Chem. Soc. Rev., 49 (2020) 554-592.
[203] T. Mori, J. Drennan, Influence of microstructure on oxide ionic conductivity in doped CeO_2 electrolytes, J. Electroceram., 17 (2006) 749-757.
[204] S. Singh, K. Singh, Effect of in-situ reduction of Fe^{3+} on physical, structural and optical properties of calcium sodium silicate glasses and glass ceramics, J. Non·Cryst. Solids, 386 (2014) 100-104.
[205] C. Schilling, A. Hofmann, C. Hess, M.V. Ganduglia-Pirovano, Raman Spectra of Polycrystalline CeO_2: A Density Functional Theory Study, J. Phys. Chem. C, 121 (2017) 20834-20849.
[206] A. Banerji, V. Grover, V. Sathe, S. Deb, A. Tyagi, CeO_2–Gd_2O_3 system: Unraveling of microscopic features by Raman spectroscopy, Solid State Commun., 149 (2009) 1689-1692.
[207] J. McBride, K. Hass, B. Poindexter, W. Weber, Raman and x-ray studies of $Ce_{1-x}RE_xO_{2-y}$, where RE= La, Pr, Nd, Eu, Gd, and Tb, J. Appl. Phys., 76 (1994) 2435-2441.
[208] R. Schmitt, J. Spring, R. Korobko, J.L.M. Rupp, Design of Oxygen Vacancy Configuration for Memristive Systems, ACS Nano, 11 (2017) 8881-8891.

[209] F. Ye, T. Mori, D.R. Ou, J. Zou, G. Auchterlonie, J. Drennan, Compositional and structural characteristics of nano-sized domains in gadolinium-doped ceria, Solid State Ion., 179 (2008) 827-831.
[210] E. Sartoretti, C. Novara, F. Giorgis, M. Piumetti, S. Bensaid, N. Russo, D. Fino, In situ Raman analyses of the soot oxidation reaction over nanostructured ceria-based catalysts, Sci. Rep., 9 (2019) 1-14.
[211] A. Filtschew, K. Hofmann, C. Hess, Ceria and its defect structure: new insights from a combined spectroscopic approach, J. Phys. Chem. C, 120 (2016) 6694-6703.
[212] J. Calvache-Muñoz, F.A. Prado, L. Tirado, L.C. Daza-Gomez, G. Cuervo-Ochoa, H.L. Calambas, J.E. Rodríguez-Páez, Structural and optical properties of CeO_2 nanoparticles synthesized by modified polymer complex method, J. Inorg. Organomet. Polym., 29 (2019) 813-826.
[213] P. Datta, P. Majewski, F. Aldinger, Study of gadolinia-doped ceria solid electrolyte surface by XPS, Mater. Charact., 60 (2009) 138-143.
[214] B. Wang, B. Zhu, S. Yun, W. Zhang, C. Xia, M. Afzal, Y. Cai, Y. Liu, Y. Wang, H. Wang, Fast ionic conduction in semiconductor $CeO_{2-\delta}$ electrolyte fuel cells, NPG Asia Mater., 11 (2019) 51.
[215] M.A.K.Y. Shah, Y. Lu, N. Mushtaq, M. Yousaf, P.D. Lund, M.I. Asghar, B. Zhu, Designing Gadolinium-doped ceria electrolyte for low temperature electrochemical energy conversion, Int. J. Hydrogen Energy, (2023).
[216] S. Rauf, B. Zhu, M. Shah, Z. Tayyab, S. Attique, N. Ali, N. Mushtaq, M.I. Asghar, P.D. Lund, C.P. Yang, Low-temperature solid oxide fuel cells based on Tm-doped $SrCeO_{2-\delta}$ semiconductor electrolytes, Mater. Today Energy, 20 (2021) 100661.
[217] A. Fetisov, G. Kozhina, S.K. Estemirova, V. Fetisov, R. Gulyaeva, XPS study of the chemical stability of $DyBa_2Cu_3O_{6+\delta}$ superconductor, Phys. C: Supercond. Appl, 508 (2015) 62-68.
[218] D.H. Hur, S.-H. Jeon, J. Han, S.-Y. Park, Y.-B. Chun, Effect of gadolinium addition on the corrosion behavior and oxide properties of titanium in boric acid solution at 50 °C, J. Mater. Res. Technol., 21 (2022) 3051-3061.
[219] S. Thakur, O.P. Pandey, K. Singh, Structural, Thermal, and Electrical Study of $Bi_{0.5}Sr_{0.5}MnO_3$, Part. Sci. Technol, 33 (2015) 178-183.
[220] S. Acharya, V. Gaikwad, S. D'Souza, S. Barman, Gd/Sm dopant-modified oxidation state and defect generation in nano-ceria, Solid State Ion., 260 (2014) 21-29.
[221] G. Accardo, D. Frattini, H.C. Ham, S.P. Yoon, Direct addition of lithium and cobalt precursors to $Ce_{0.8}Gd_{0.2}O_{1.95}$ electrolytes to improve microstructural and electrochemical properties in IT-SOFC at lower sintering temperature, Ceram. Int., 45 (2019) 9348-9358.
[222] W. Lee, S.-Y. Chen, E. Tseng, A. Gloter, C.-L. Chen, Study of Defect Structure in Ferromagnetic Nanocrystalline CeO_2: Effect of Ionic Radius, J. Phys. Chem. C, 120 (2016) 14874-14882.
[223] S. Anirban, A. Dutta, Structure and defect interaction mediated transport mechanism of mixed di-tri valent cation containing ceria-based Ionic conductors, Int. J. Hydrogen Energy, 43 (2018) 23418-23429.
[224] S. Sulekar, M. Mehr, J.H. Kim, J.C. Nino, Effect of Reduced Atmosphere Sintering on Blocking Grain Boundaries in Rare-Earth Doped Ceria, Inorganics, 9 (2021) 1-12.
[225] B.C.H. Steele, A. Heinzel, Materials for fuel-cell technologies, Nature, 414 (2001) 345-352.
[226] N. Jaiswal, D. Kumar, S. Upadhyay, O. Parkash, Ceria co-doped with calcium (Ca) and strontium (Sr): a potential candidate as a solid electrolyte for intermediate temperature solid oxide fuel cells, Ionics, 20 (2014) 45-54.

[227] S. Medisetti, J. Ahn, S. Patil, A. Goel, Y. Bangaru, G.V. Sabhahit, G.U.B. Babu, J.-H. Lee, H.P. Dasari, Synthesis of GDC electrolyte material for IT-SOFCs using glucose & fructose and its characterization, Nano-Structures & Nano-Objects, 11 (2017) 7-12.
[228] B. Li, S. Liu, X. Liu, G. Hao, H. Wang, W. Su, Study on GDC-LSGM composite electrolytes for intermediate-temperature solid oxide fuel cells, Int. J. Hydrogen Energy, 38 (2013) 11392-11397.
[229] Y.-C. Wu, Y.-Y. Liao, Effect of Ca^{2+} and Sr^{2+} doping on the microstructure and cell performance of samaria-doped ceria electrolytes used in solid oxide fuel cells, Int. J. Hydrogen Energy, 41 (2016) 13591-13602.
[230] A.R. Hartwell, C.A. Wilhelm, T.S. Welles, R.J. Milcarek, J. Ahn, Effects of Synthesis Gas Concentration, Composition, and Operational Time on Tubular Solid Oxide Fuel Cell Performance, Sustainability, 14 (2022).
[231] R. Li, C. Li, L. Cao, Y. Zeng, Z. Wang, Z. Ye, Y. Zhang, Preparation and characterization of GDC-Li_2SO_4/Li_2CO_3 nanocomposite electrolytes for applications in intermediate solid oxide fuel cells, Ceram. Int., 43 (2017) 12191-12195.
[232] V. De Marco, A. Iannaci, M. Lo Faro, V.M. Sglavo, Influence of Copper-based Anode Composition on Intermediate Temperature Solid Oxide Fuel Cells Performance, Fuel Cells, 17 (2017) 708-715.
[233] Y.-G. Choi, J.-Y. Park, J.-W. Son, J.-H. Lee, H.-J. Je, B.-K. Kim, H.-W. Lee, K.J. Yoon, Ceria-based electrolyte reinforced by sol–gel technique for intermediate-temperature solid oxide fuel cells, Int. J. Hydrogen Energy, 38 (2013) 9867-9872.